Observatório Nacional

Divisão de Programas de Pós-graduação em Geofísica

EARLY PALEOGENE ASTROCHRONOLOGY FROM THE AGULHAS PLATEAU AND MENTELLE BASIN RECORDS (IODP EXPEDITIONS 392 AND 369): ORBITAL CALIBRATION FROM THE K-Pg – PETM INTERVAL

Bernardo Mokan Maffessoni

Dissertation presented to the Graduate Program in Geophysics of the Observatório Nacional, as part of the requirements for obtaining the title of Master in Geophysics.

Advisor: Dr. Daniel Ribeiro Franco
Co-advisors: Dra. Mariane Candido (ON/MCTI) and Dr. Joao Maurício Figueiredo Ramos (PETROBRAS)

Rio de Janeiro

May 2026

"EARLY PALEOGENE ASTROCHRONOLOGY FROM THE AGULHAS PLATEAU AND MENTELLE BASIN RECORDS (IODP EXPEDITIONS 392 AND 369): ORBITAL CALIBRATION FROM THE K-Pg – PETM INTERVAL"

Bernardo Mokan Maffessoni

DISSERTAÇÃO SUBMETIDA AO CORPO DOCENTE DO PROGRAMA DE PÓS-GRADUAÇÃO EM GEOFÍSICA DO OBSERVATÓRIO NACIONAL COMO PARTE DOS REQUISITOS NECESSÁRIOS PARA A OBTENÇÃO DO GRAU DE MESTRE EM GEOFÍSICA.

Aprovada por:

Dr. Daniel Ribeiro Franco - (ON) - (Orientador)

Dra. Natália Braun dos Santos - (ON)

Dra. Linda Alide Hinnov - (George Mason University) - (EUA)

RIO DE JANEIRO – BRASIL

02 DE JUNHO DE 2026

ACKNOWLEDGEMENTS

To God / the Universe and to my guardian angel for the hours of talking, and for showing the way.

To my family, Marcelo, Adriana and Manoela, for each and every form of support and encouragement. Seriously… they are **undisputedly** the best and I love them.

To my dearest friends, Paloma de Freitas Ferreira (Poma Aparecida Pereira, my girlfriend), Matheus Gaudert, Vinicius Colnaghi, Maurício Righi, Gabriel Squizzato and Éfren Mota de Souza for all their support and for listening. Without you guys, I don't know what I'd do...

To my advisor, Dr. Daniel Ribeiro Franco, for his scientific guidance, patience, and support throughout this journey. To Dr. Joice Cagliari for introducing me to the world of cyclostratigraphy and for providing me with so many opportunities throughout my academic career.

To my co-advisor, Dr. Mariane Candido, for her expertise, dedication to science, constructive criticism, unwavering support and enthusiasm for this research. To my co-advisor João Maurício Figueiredo Ramos for his good advices and his assistance on this work wrapping-up process.

To my colleagues at the Observatório Nacional, Raysa de Magalhães Rocha, Mateus Fontana Michelon, and Evelyn Nascimento, for the shared hours of work, ideas, and friendship that made this project possible. To the Cyclostratigraphy Field Training School 2025 team, for all the for all the knowledge-sharing and camaraderie.

To the International Ocean Discovery Program (IODP) and the science parties of Expeditions 369 and 392 for the collection, processing, and public availability of the data on which this work is based. I also thank to the Observatório Nacional and the Coordenação de Aperfeiçoamento de Pessoal de Nível Superior (CAPES) for the financial support that made this research viable.

“Uma árvore, por mais que cresça, nunca atinge um tamanho aproximado.”

José Carlos Maffessoni (Vô Zeca)

SUMMARY

ABSTRACT **8**

RESUMO **10**

INDEX OF FIGURES **12**

LIST OF TABLES **13**

LIST OF ABBREVIATIONS AND ACRONYMS **14**

1 INTRODUCTION **15**

2 OBJECTIVES AND JUSTIFICATION **17**

2.1 GENERAL OBJECTIVES 17

2.2 JUSTIFICATION 17

3 EARLY PALEOCENE PALEOCEANOGRAPHIC AND CLIMATIC EVOLUTION: K-PG BOUNDARY TO THE POST-PETM INTERVAL (66 - 54 MA) **19**

3.1 ASTRONOMICAL FORCING AND THE CYCLOSTRATIGRAPHIC ARCHITECTURE OF THE PALEOCENE 19

3.2 CHRONOSTRATIGRAPHIC CONSTRAINTS FROM MAGNETO-, BIO- AND CHEMOSTRATIGRAPHY 20

3.2.1 Magnetostratigraphy **20**

3.2.2 Biostratigraphy **20**

3.2.3 Elemental Chemostratigraphy **21**

3.3 FROM THE K–PG BOUNDARY TO THE PETM: MAJOR EVENTS OF THE EARLY PALEOCENE 21

3.3.1 The K-Pg event: Evidence of mass extinction (~66 Ma) **21**

3.3.2 The post K-Pg interval (~66 - 63 Ma): Catastrophe and recovery **22**

3.3.3 The Latest Danian Event and the Danian-Selandian Transition (~62.5 - 61 Ma) **22**

3.3.4 The Mid-Paleocene Biotic Event, Carbon Isotope Maximum, and Sea-Level Dynamics (~59 - 57.5 Ma) **23**

3.3.5 Late Paleocene Warming and Pre-PETM Destabilisation of the Carbon Cycle (~58 - 56 Ma) **23**

3.3.6 The Paleocene-Eocene Thermal Maximum and Conditions Extending to 54 Ma **24**

4 GEOLOGICAL CONTEXT: **25**

4.1 IODP EXPEDITION 392 - AGULHAS PLATEAU, SOUTH INDIAN OCEAN 25
4.1.1 Geological and paleoceanographic setting 26
4.1.2 Seismostratigraphic framework 26
4.1.3 K-Pg / PETM interval on Hole U1579D 27
4.2 IODP EXPEDITION 369 - MENTELLE BASIN, WESTERN AUSTRALIA 28
4.2.1 Geological and tectonic setting 30
4.2.2 Rift evolution and paleogeography 30
4.2.3 K-Pg / PETM interval on Hole U1514C 31
5 THE MILANKOVITCH CYCLES 32
5.1 THE CLIMATIC SPECTRUM 32
5.2 ORBITAL CYCLES AND CLIMATE FORCING 32
6 METHODS AND PROCEDURES 36
6.1 GAMMA RAY WELL LOGGING: NGR, U, TH AND K 36
6.2 DATA BASE AND CROSS-CORRELATION 36
6.3 CYCLOSTRATIGRAPHY 37
6.4 ASTRONOMICAL TIME SCALE 38
6.5 SAR TESTING 38
6.5.1 COCO / eCOCO 38
6.5.2 TimeOpt / eTimeOpt 39
6.5.3 A multi-method approach to evaluate SAR 39
6.6 WAVELET TRANSFORM ANALYSIS 40
6.7 INTEGRATED PREDICTION ERROR FILTERING ANALYSIS (INPEFA) 41
7 MANUSCRIPT: CYCLOSTRATIGRAPHY OF AGULHAS PLATEAU AND MENTELLE BASIN RECORDS (IODP EXPEDITIONS 392 AND 369): AN ORBITALLY-BASED CHRONOSTRATIGRAPHY FROM THE K–PG BOUNDARY TO THE PETM 42
ABSTRACT 42
1 INTRODUCTION 43
2 GEOLOGICAL SETTING 44
2.1 IODP EXPEDITION 392 - HOLE U1579D, AGULHAS PLATEAU 44
2.2 IODP EXPEDITION 369 - HOLE U1514C, MENTELLE BASIN 46

3 METHODS 48

3.1 WIRELINE LOG DATA 48

3.2 PROXY SELECTION 49

3.3 CYCLOSTRATIGRAPHY 49

3.4 ASTRONOMICAL TIME SCALE 50

3.5 INTEGRATED PREDICTION ERROR FILTER ANALYSIS (INPEFA) 50

4 RESULTS 51

4.1 SPECTRAL ANALYSIS AND ORBITAL FREQUENCY IDENTIFICATION 51

4.2 CYCLOSTRATIGRAPHIC CONSTRAINTS ON SEDIMENT ACCUMULATION RATES 54

4.3 INPEFA 54

4.4 ASTRONOMICAL TIME SCALE 55

4.4.1 Hole U1579D 55

4.4.2 Hole U1514C 57

5 DISCUSSION 58

5.1 SAR CONVERGENCE, ORBITAL RESOLUTION, AND IMPLICATIONS FOR PETM AGE 58

5.2 INPEFA AND DEPOSITIONAL TRENDS 59

5.3 SPECTRAL RESOLUTION AND LITHOLOGICAL EFFECTS ON LONG-ECCENTRICITY BAND DEFINITION 60

5.4 THANETIAN ANOMALY AT ~58.15 MA: THE "*" CIE AND ITS PALAEOCLIMATIC CONTEXT 60

5.5 PETM REPOSITIONING 61

5.6 GLOBAL CORRELATION AND FORWARD PERSPECTIVES 61

6 CONCLUSIONS 62

REFERENCES 63

SUPLEMENTARY MATERIAL 67

8 CONCLUDING REMARKS 104

REFERENCES 106

Abstract of the dissertation presented to the National Observatory's Graduate Program in Geophysics as a partial fulfillment of the requirements for the degree of Master in Geophysics.

EARLY PALEOGENE ASTROCHRONOLOGY FROM THE AGULHAS PLATEAU AND MENTELLE BASIN RECORDS (IODP EXPEDITIONS 392 AND 369): ORBITAL CALIBRATION FROM THE K-Pg – PETM INTERVAL

Bernardo Mokan Maffessoni

May 2026

ABSTRACT

The present master's dissertation aimed at conducting a detailed cyclostratigraphic study of gamma-ray logging series (total gamma and thorium, potassium, and uranium spectral channels) from two deep-marine Paleocene sequences spanning from the Cretaceous-Paleogene boundary (~66 Ma) to the Paleocene-Eocene Thermal Maximum (~56 Ma), an interval encompassing the post-extinction biotic recovery, the progressive destabilisation of the global carbon cycle, and a series of orbitally paced hyperthermal events that culminated in the largest rapid warming event of the Cenozoic, recovered during Expeditions 392 (Hole U1579D, Agulhas Plateau, southern Indian Ocean) and 369 (Hole U1514C, Mentelle Basin, offshore western Australia). Preliminary cross-correlation tests between the gamma ray component data series indicated a strong zero-lag correlation of the thorium channel with the total gamma-ray series ($|r|$ = 0.784 and 0.917; holes U1579D and U1514C, respectively) and with the potassium series ($|r|$ = 0.737 and 0.893, respectively), alongside phase offsets and reduced coherence consistent with post-depositional diagenetic remobilisation for the uranium channel, supporting the selection of the thorium series as the most suitable proxy for cyclostratigraphic analysis in these pelagic carbonate sequences. Multi-taper method spectral analyses identified significant spectral peaks exceeding the 99% confidence level at both holes. Long eccentricity (E405) peaks were detected at 7.39, 5.46, and 5.07 m at U1579D, and at 7.04, 6.29, 4.45, and 4.29 m at U1514C. Short eccentricity (e131, e125, e99, e95) peaks were identified at 2.80, 2.57, 2.40, and 2.03 m at U1579D, and at 1.34 and 1.28 m at U1514C. These periodicities are consistent with the predicted spectral ratio for ~61 Ma (405:131:125:99:95:39 = 21.6:6.7:5.1:2.1:1.2:1; Laskar et al., 2004). In conjunction with evolutionary harmonic analysis of the series, it was possible to delimit the frequency band associated with the long eccentricity signal, with a central wavelength ratio of ~5 to 7 m (band limits of ~4.55-8.40 m at U1579D; ~4.24-7.19 m at U1514C). COCO, eCOCO, and TimeOpt analyses corroborate sedimentary accumulation rate estimates of ~1.1-2.1 cm/kyr for U1579D (main peak ~1.5-1.9 cm/kyr; TimeOpt ~2.12 cm/kyr) and ~1.0-1.8 cm/kyr for U1514C (TimeOpt ~1.62 cm/kyr). Short eccentricity cycles are identified but exhibit intermittent frequency on evolutionary

harmonic analysis. Obliquity (~39 kyr) is preliminarily identified at U1579D; precession is unresolvable at the 15.2 cm sampling resolution. Taken together, these results allow the construction of astronomical time scales anchored at the K-Pg boundary and calibrated by biostratigraphic datums, recording approximately 25.5 and 25 long eccentricity cycles at U1579D and U1514C, respectively, consistent with the astrochronological framework of 25 cycles for the Paleocene and a PETM age of ~ 55.7-55.9 Ma. A prominent positive thorium anomaly at both holes is constrained to ~58.15 Ma, consistent with the unnamed "*" carbon isotope excursion marking the termination of the Paleocene Oxygen Isotope Maximum. This excursion occurs close to an eccentricity minimum and is not considered a classical hyperthermal; its expression as a positive thorium anomaly at both holes argues for a globally coherent sedimentary signal consistent with carbonate dilution or enhanced clay flux during this global carbon-cycle transition. The stronger orbital signal preservation at U1579D relative to U1514C is attributed to the more homogeneous Nannofossil Chalk lithology at the Agulhas Plateau versus the greater lithological heterogeneity of the Mentelle Basin. Integrated Prediction Error Filter Analysis curves document trend reversals consistent with depositional regime changes at the Cretaceous-Paleogene boundary and near the Early Late Paleocene Event /"*" carbon isotope excursion interval, broadly consistent with the Paleocene barystatic sea level, and possibly providing a wireline-based trend indicator of Paleocene depositional dynamics at the Indian Ocean.

Keywords: Cyclostratigraphy; Paleocene; K-Pg boundary; PETM; thorium; E405; astrochronology.

Resumo de dissertação apresentado ao Programa de Pós-Graduação em Geofísica do Observatório Nacional como parte dos requisitos necessários para a obtenção do título de Mestre em Geofísica.

ASTROCRONOLOGIA DO PALEÓGENO INFERIOR A PARTIR DE REGISTROS DO PLATÔ DE AGULHAS E DA BACIA DE MENTELLE (EXPEDIÇÕES IODP 392 E 369): CALIBRAÇÃO ORBITAL DO INTERVALO K-Pg - PETM

Bernardo Mokan Maffessoni

Maio de 2026

RESUMO

A presente dissertação de mestrado teve como objetivo a realização de um estudo cicloestratigráfico detalhado de séries de perfilagem de raios gama (gama total e canais espectrais de tório, potássio e urânio) de duas sequências pelágicas paleocênicas de mar profundo, abrangendo o intervalo entre o limite Cretáceo-Paleógeno (~66 Ma) e o Máximo Térmico do Paleoceno-Eoceno (~56 Ma). O intervalo engloba a recuperação biótica pós-extinção, a desestabilização progressiva do ciclo global do carbono e uma série de eventos hipertermais orbitalmente controlados que culminaram no maior evento de aquecimento rápido do Cenozoico, recuperadas durante as Expedições 392 (Furo U1579D, Platô das Agulhas, sul do Oceano Índico) e 369 (Furo U1514C, Bacia de Mentelle, margem oeste da Austrália). Testes preliminares de correlação cruzada entre as séries de dados dos componentes dos raios gama indicaram forte correlação de defasagem nula do canal de tório com a série de gama total (|r| = 0,784 e 0,917; sítios U1579D e U1514C, respectivamente) e com a série de potássio (|r| = 0,737 e 0,893, respectivamente), além de defasagens de fase e coerência reduzida consistentes com remobilização diagenética pós-deposicional para o canal de urânio, fundamentando a seleção da série de tório como o proxy mais adequado para a análise cicloestratigráfica nessas sequências de carbonatos pelágicos. Análises espectrais pelo método de múltiplas janelas identificaram picos espectrais significativos acima do nível de confiança de 99% em ambos os sítios. Picos de excentricidade longa (E405) foram detectados a 7,39, 5,46 e 5,07 m em U1579D, e a 7,04, 6,29, 4,45 e 4,29 m em U1514C. Picos de excentricidade curta (e131, e125, e99, e95) foram identificados a 2,80, 2,57, 2,40 e 2,03 m em U1579D, e a 1,34 e 1,28 m em U1514C. Essas periodicidades são consistentes com a razão espectral prevista para ~61 Ma (405:131:125:99:95:39 = 21,6:6,7:5,1:2,1:1,2:1; Laskar et al., 2004). Em conjunto com a análise harmônica evolutiva das séries, foi possível delimitar a banda de frequência associada ao sinal de excentricidade longa, com razão de comprimento de onda central de ~5 a 7 m (limites de banda de ~4,55-8,40 m em U1579D; ~4,24-7,19 m em U1514C). As análises COCO, eCOCO e TimeOpt corroboram estimativas de taxa de acumulação sedimentar de ~1,1-2,1 cm/kyr para U1579D (pico principal ~1,5-1,9 cm/kyr; TimeOpt ~2,12 cm/kyr) e ~1,0-1,8 cm/kyr para U1514C (TimeOpt ~1,62 cm/kyr). Os ciclos de excentricidade curta são identificados, mas

apresentam expressão intermitente na análise harmônica evolutiva. A obliquidade (~39 kyr) é preliminarmente identificada em U1579D; a precessão não é resolvível na resolução de amostragem de 15,2 cm. Em conjunto, esses resultados permitem a construção de escalas de tempo astronômicas ancoradas no limite K-Pg e calibradas por datums bioestratigráficos, registrando aproximadamente 25,5 e 25 ciclos de excentricidade longa em U1579D e U1514C, respectivamente, consistentes com o arcabouço astrocronológico de 25 ciclos para o Paleoceno e uma idade do PETM de ~55,7-55,9 Ma. Uma proeminente anomalia positiva de tório em ambos os furos é constraída a ~58,15 Ma, consistente com a excursão isotópica de carbono inominada "" que marca a terminação do Máximo de Isótopos de Oxigênio do Paleoceno. Essa excursão ocorre próximo a um mínimo de excentricidade e não é considerada um hipertermal clássico; sua expressão como anomalia positiva de tório em ambos os sítios aponta para um sinal sedimentar globalmente coerente, consistente com diluição de carbonato ou aumento do fluxo de argilas durante essa transição global do ciclo do carbono. A melhor preservação do sinal orbital em U1579D em relação a U1514C é atribuída à litologia mais homogênea de giz nanofossilífero no Platô das Agulhas, em contraste com a maior heterogeneidade litológica da Bacia de Mentelle. As curvas de Análise de Filtro de Erro de Predição Integrado documentam inversões de tendência consistentes com mudanças de regime deposicional no limite Cretáceo-Paleógeno e próximo ao intervalo do Evento do Paleoceno Tardio Inicial / excursão isotópica de carbono "*", amplamente consistentes com o nível do mar barystático do Paleoceno, possivelmente fornecendo um indicador de tendência baseado em perfilagem das dinâmicas deposicionais paleocênicas no Oceano Índico.*

Palavras-chave: Cicloestratigrafia; Paleoceno; limite K-Pg; PETM; tório; E405; astrocronologia.

INDEX OF FIGURES

Figure 1 – **A**. Bathymetry of the Agulhas Plateau (AP) (Sandwell and Smith, 1997). Expedition 392 sites are marked as red stars on seismic lines (black lines) (Uenzelmann-Neben, 1998, 2005, 2014). Red arrow = Site U1579; Yellow diamond = Expedition 361 Site U1475 (Gruetzner *et al*., 2019; Hall *et al*., 2017); **B**. Auxiliary map showing the broader location of the expedition's area in which abbreviations stand for: SA = South Africa; AB = Agulhas Bank; MOZR = Mozambique Ridge. **C**. Currents and water masses active in the African-Southern Ocean gateway: AC = Agulhas Current; NADW = North Atlantic Deep Water; AABW = Antarctic Bottom Water. Modified from Uenzelmann-Neben *et al.* (2023). 26

Figure 2 – **A**. location of Site U1579 over seismic Line AWI-20050201. Preliminary interpretation of seismic units according to the chronostratigraphic model is shown. CDP = common depth point, TWT = two-way traveltime, ZS = zeolitic silicified sediments (Uenzelmann-Neben *et al*., 2023); **B.** Zoom of the highlighted area within dashed white limits for better visualization of the studied interval marked approximately by red hollowed polygon. 27

Figure 3 - Schematic of the K/Pg boundary, Hole U1579D: The boundary is characterised by a sharp color change at 33R-6A, 96 to 99 cm, from reddish-brown clayey calcareous chalk to grayish-green calcareous chalk with clay. The interval is affected by drilling-related deformation and includes a narrow (~1 cm) greenish-gray layer of calcareous ooze with clay (Uenzelmann-Neben *et al*., 2023).....28

Figure 4 – **A**. Regional context of the Naturaliste Plateau and Mentelle Basin, showing the locations of major reflection seismic profiles, nearby DSDP sites (red numbers), and Expedition 369 sites (yellow circles). Site U1514 is highlighted by a red arrow; **B**. Auxiliary map for location of the two different areas highlighted by their respective border colours; **C**. Location other Expedition 369 related sites. Site U1512 (yellow circle) within the GAB, the Leg 182 site (white circle), and petroleum exploration wells (black circles). Modified from Huber *et al.* (2019). 29

Figure 5 – **A**. Time-migrated Geoscience Australia reflection seismic with location of Site U1514 marked along seismic shotpoints (Huber *et al*., 2019); **B**. Zoom of the highlighted area within dashed white limits for better visualization of the studied interval marked approximately by red hollowed polygon. Green line along seismic reflector represents the upper limit, possibly related to the Paleocene/Eocene boundary while light blue line to the bottom of the studied sequence represents the Paleocene/Maastrichtian boundary. Modified from Huber *et al.* (2019). 30

Figure 6 – Schematic representation of the three Milankovitch orbital parameters and their characteristic temporal signals over a 1 Myr window. **A**. 405 kyr Long eccentricity and **B**. ~100 kyr Short eccentricity: a single parameter expressed across two frequency bands, the long eccentricity (E_{405}, ~405 kyr), driven by the Jupiter-Venus gravitational interaction and stable for ≥ 250 Myr, and the short eccentricity (E_{100}, ~95–131 kyr), whose amplitude is modulated by the E_{405} envelope. **C**. Obliquity (ε): cyclic variation in the tilt of Earth's rotational axis relative to its orbital plane (~41 kyr; range 22.1°-24.5°), governing latitudinal insolation contrasts. **D**. Precession index (e sin ψ): combined effect of axial and apsidal precession (~21 kyr mean period), controlling which hemisphere experiences summer at perihelion and affecting all latitudes. Orbital geometries are exaggerated for clarity. Period values correspond to present-day orbital modelling (La2004 solution; Laskar *et al*., 2004).....34

LIST OF TABLES

Table 1. Orbital periodicities predicted by the La2004 astronomical solution (Laskar *et al.*, 2004) for a mean age of 61 Ma, with corresponding expected wavelengths at the primary sediment accumulation rate estimates for each hole. Observed band limits (from MTM and EHA analyses) are given in the rightmost columns. E = long eccentricity; e = short eccentricity; O = obliquity; P = precession; M = million-year-scale band. n.r. = not resolved above 95% confidence threshold. 53

Table 2 Biostratigraphic datums used and excluded from ATS calibration at Holes U1579D and U1514C. B = base (first occurrence); T = top (last occurrence); Bc = consistent occurrence base. 56

LIST OF ABBREVIATIONS AND ACRONYMS

AR(1) - First-order Autoregressive model
ATS - Astronomical Time Scale
BFEE - Benthic Foraminiferal Extinction Event
CCD - Carbonate Compensation Depth
CCF - Cross Correlation Function
CIE - Carbon Isotope Excursion
CNP - Paleocene Calcareous Nannofossil
COCO - Correlation Coefficient
COI - Cone of Influence
CSF-A - Core Depth Below Seafloor
CWT - Continuous Wavelet Transform
DSDP - Deep Sea Drilling Project
eCOCO - Evolutionary Correlation Coefficient
EECO - Early Eocene Climatic Optimum
eFFT - Evolutionary Fast Fourier Transform
EHA - Evolutionary Harmonic Analysis
ELPE - Early Late Paleocene Event
E405 - 405-kyr long eccentricity cycle
E100 - ~100-kyr short eccentricity cycle
FFT - Fast Fourier Transform
GAB - Great Australian Bight
GPTS - Geomagnetic Polarity Time Scale
GSSP - Global Boundary Stratotype Section and Point
HCGR - Uranium-free gamma radiation
HFK - Formation potassium
HNGS - Hostile Environment NGR Sonde
HSGR - Standard (total) gamma ray
HTHO - Formation thorium
HURA - Formation uranium
INPEFA - Integrated Prediction Error FilterAnalysis
IODP - International Ocean Discovery Program
K - Potassium
K-Pg - Cretaceous-Paleogene Boundary
LDE - Latest Danian Event
LDEO - Lamont-Doherty Earth Observatory
LIP - Large Igneous Province
LOWESS - Locally Weighted Scatterplot Smoothing
MB - Mentelle Basin
MPBE - Mid-Paleocene Biotic Event
MTM - Multitaper Method
NAIP - North Atlantic Igneous Province
NGR - Natural Gamma Ray
OAE - Oceanic Anoxic Events
ODP - Ocean Drilling Program
PCIM - Paleocene Carbon Isotope Maximum
PEFA - Prediction Error Filter Analysis
PETM - Paleocene-Eocene Thermal Maximum
POIM - Paleocene Oxygen Isotope Maximum
POE - Pre-Onset Excursion
SAR - Sediment Accumulation Rate
STTE - Selandian-Thanetian Transition Event
Th - Thorium
U - Uranium
WMSF - Wireline log matched depth below seafloor

1 INTRODUCTION

Throughout Earth's history, extreme events have repeatedly disrupted the stability of the Earth system, reshaping environmental conditions and influencing the evolution of life. These perturbations, operating across a range of temporal and spatial scales, have significantly altered ocean circulation patterns and global ecosystems. Evidence of such events is preserved in marine sedimentary archives, where successive strata record characteristic sedimentary features and biological assemblages that provide key insights into Earth system processes. However, the sedimentary record is inherently incomplete, representing only the preserved fraction of past events and commonly including hiatuses associated with erosion and non-deposition.

Among these perturbations, mass extinctions, collectively referred to as the "Big Five", are the most extreme disruptions of the Earth system, fully reshaping the biosphere through the loss of over 75% of estimated species and opening ecological spaces for new organisms throughout the last ~540 Myr (Barnosky *et al.,* 2011; Burgess, 2019; Jablonsky and Edie, 2025). Improved understanding and chronostratigraphic calibration of the geological time intervals associated with post-extinction biodiversity recovery are essential for assessing biosphere resilience and the factors that govern ecosystem recovery, while also providing a basis for interpreting both past biological crises and the biodiversity loss observed today (Hull, 2015; Bottjer, 2024; Dunhill *et al.,* 2024).

In such context, the **Paleogene Period** (~66 to 23 Ma; Zachos *et al.,* 2001) represents a pivotal interval in Earth's history, marked by profound climatic and biotic transformations. It encompasses both the aftermath of the end-Cretaceous mass extinction and a series of global warming events that significantly affected ocean-atmosphere interactions, biogeochemical cycles, and sedimentary regimes (Friedrich *et al.,* 2012). Its onset is marked by the **Paleocene Epoch** (~ 66 - 56 Ma; Gradstein *et al.,* 2020), spanning from the Cretaceous-Paleogene (K-Pg) boundary, associated with an abrupt extinction of approximately 75% of Earth's species, primarily linked to the impact of a large extraterrestrial body and its cascading climatic and ecological consequences (e.g., Alvarez *et al.,* 1980; Schulte *et al.,* 2010) - to the Paleocene-Eocene Thermal Maximum (PETM), characterised by a rapid global temperature increase of ~ 5-8°C over a few thousand years, accompanied by ocean acidification, major disruptions to the carbon cycle, and large-scale biotic migrations (e.g., Zachos *et al.,* 2005, 2008; Sluijs *et al.,* 2011). During the Paleocene, deep-ocean temperatures rose by approximately 6-8 °C from the K-Pg boundary to the Early Eocene Climatic Optimum (EECO; Zachos *et al.,* 2001; Westerhold *et al.,* 2020), the biological pump underwent a protracted multi-million-year recovery (Barnet *et al.,* 2019), and a series of orbitally paced hyperthermal events punctuated a long-term warming trend driven by volcanic CO_2 emissions from the North Atlantic Igneous Province (NAIP; Svensen *et al.,* 2004; Barnet *et al.,* 2019; Gutjahr *et al.,* 2017).

Regarding the major environmental changes encompassed by the Paleocene, the establishment of high-quality chronostratigraphic constraints by improvements at the temporal calibration of the K-Pg boundary and the PETM is of central importance, as both events correspond to primary, global time markers for estimating rates, timespans, and temporal relationships of life recovery, greenhouse warming, carbon-cycle disturbances,

and sedimentary processes throughout the early Paleogene. In such context, cyclostratigraphy has emerged as a key tool for refining the temporal resolution of sedimentary sequences by identifying periodic signals related to variations in Earth's orbital parameters, known as Milankovitch cycles (e.g., Barthes *et al.,* 1999; Weedon, 2003; Westerhold *et al.,* 2008; Paulissen and Luthi, 2011; Hinnov, 2013; 2018; Dinarès-Turell *et al.,* 2014; Li *et al.,* 2019; Leandro *et al.,* 2022). Among the proxies commonly used, natural gamma ray (NGR) and its spectral components stand out due to high resolution, cost-effectiveness, and sensitivity to lithological and compositional variations driven by climatic forcing (e.g., Goldberg, 1997; Myers and Wignall, 1987; Barthes *et al.,* 1999; Ruffell and Worden, 2000; Gorgas and Wilkens, 2002; Schnyder *et al.,* 2006; Paulissen and Luthi, 2011). In particular, the thorium channel (HTHO), as a lithophile, diagenetically immobile element concentrated in detrital heavy minerals, has been shown to faithfully record orbital-scale detrital flux variations in pelagic carbonate sequences without the redox-sensitive behaviour that compromises uranium as a cyclostratigraphic proxy (e.g., Adams and Weaver, 1958; Myers and Wignall, 1987; Osmond and Ivanovich, 1992; Schnyder *et al.,* 2006).

This study applies cyclostratigraphic methods to HTHO data obtained from two deep-marine sedimentary records recovered during IODP expeditions: Hole U1579D, located on the Agulhas Plateau (IODP Expedition 392, South Indian Ocean), and Hole U1514C, located on the western Australian margin in the Mentelle Basin (IODP Expedition 369). These successions span the entire Paleocene interval and include both the K-Pg (~66 Ma) and PETM (~56 Ma) as key stratigraphic tie points (Huber *et al.,* 2019; Uenzelmann-Neben *et al.,* 2023).

The primary objective of this work is to establish cyclostratigraphic frameworks for both pelagic carbonate records, complementing previous interpretations based on magneto- and biostratigraphic constraints, thereby refining their chronostratigraphy and estimating the duration of the preserved Paleocene record. In doing so, this study also investigates the differential preservation of orbital signals between the two depositional settings, evaluates the suitability of HTHO as a cyclostratigraphic proxy in pelagic carbonate sequences, and contribute to discussions about the unnamed "*" carbon isotope excursion event at ~58.15 Ma.

2 OBJECTIVES AND JUSTIFICATION

2.1 GENERAL OBJECTIVES

This study aims to establish cyclostratigraphic frameworks for two pelagic carbonate records recovered during IODP Expeditions 392 (Hole U1579D, Agulhas Plateau) and 369 (Hole U1514C, Mentelle Basin), spanning the Paleocene interval between the K-Pg boundary (~66.0 Ma) and the PETM (~56.0 Ma).

To achieve this goal, the study pursues the following specific objectives:

(1) Proxy evaluation via cross-correlation function (CCF) analysis, to assess the behaviour and mutual relationships of the available spectral gamma-ray channels (NGR, potassium, thorium, and uranium) and to identify the most reliable proxy for orbital signal detection in each borehole;

(2) Detrending method evaluation, to compare the performance of multiple detrending approaches (linear, LOESS, high-pass Butterworth filter) and to identify the method that best isolates orbital-band signals while avoiding apparent transient coalescence between low-frequency spectral power, interpreted as million-year-scale eccentricity modulations, and the 405-kyr orbital eccentricity component.

(3) Recognition of orbital imprint through spectral analyses (MTM and EHA) applied to the Thorium series, as well as sedimentary accumulation rate (SAR) testing methods (COCO, eCOCO, and TimeOpt) in order to estimate sedimentation rates consistent with the given target periodicities;

(4) Construction of astronomical time scales (ATS) for both boreholes, anchored to the K-Pg boundary and calibrated by biostratigraphic datum positions, in order to refine the chronostratigraphic placement of Paleocene events;

(5) Evaluation of depositional trend patterns for both stratigraphies by means of integrated prediction error filter analysis (INPEFA) to identify changes in depositional regimes and sequence stratigraphic surfaces, and to compare such findings with the Paleocene barystatic sea-level record from Miller *et al.* (2024);

(6) Inter-site comparison and event identification, to assess the differential preservation of orbital signals between U1579D and U1514C stratigraphies, and to use the co-temporal expression of anomalous HTHO peaks at both holes as a basis for identifying and contextualizing the unnamed "*" CIE event at ~58.15 Ma (e.g., Barnet *et al.,* 2019; Hollis *et al.,* 2022).

2.2 JUSTIFICATION

The Paleocene represents a critical interval for understanding the interplay among orbital forcing, carbon cycle dynamics, and Earth's climate system. Despite significant advances in Paleocene astrochronology from classical deep-sea sections at Walvis Ridge (Westerhold *et al.,* 2008; Littler *et al.,* 2014; Barnet *et al.,* 2019), Shatsky Rise (Westerhold *et al.,* 2011; Zachos *et al.,* 2010), and Zumaia (Dinarès-Turell *et al.,* 2003, 2007, 2014), the Indian Ocean sector remains comparatively underrepresented in cyclostratigraphic studies. The IODP wells investigated here, one on the Agulhas Plateau off South Africa (Hole U1579D) and one on the western Australian margin (Hole U1514C), fill an important geographic gap in the global Paleocene orbital framework.

Moreover, the use of downhole spectral gamma-ray data for cyclostratigraphy, as opposed to the core-based geochemical proxies (XRF-Fe, $CaCO_3$, $\delta^{13}C$) that have underpinned most Paleocene ATS work, provides an independent and publicly available dataset for testing and extending the orbital calibration of these wells. The identification of the "*" CIE at ~58.15 Ma (Littler *et al.,* 2014; Barnet *et al.,* 2019; Hollis *et al.,* 2022) at two widely separated Indian Ocean locations provides new geographic constraints on this poorly characterised global perturbation and its paleoclimatic context at the termination of the Paleocene Oxygen Isotope Maximum (Hollis *et al.,* 2022).

3 EARLY PALEOCENE PALEOCEANOGRAPHIC AND CLIMATIC EVOLUTION: K-PG BOUNDARY TO THE POST-PETM INTERVAL (66 - 54 MA)

The Paleocene epoch, spanning from the K-Pg extinction (~66 Ma) to the PETM (~56 Ma), records the recovery from the end-Cretaceous mass extinction, the progressive destabilisation of the global carbon cycle, and the culmination of greenhouse warming in the Paleocene-Eocene Thermal Maximum. Between 66 and 54 Ma, deep-ocean temperatures rose by approximately 8 to 10 °C, the biological pump underwent a protracted multi-million-year recovery, and a series of orbitally paced hyperthermal events punctuated a long-term warming trend driven by volcanic CO_2 emissions from the North Atlantic Igneous Province (NAIP). This period represents a key phase in global paleoclimatic evolution, often cited as a geological analogue for modern anthropogenic CO_2 emissions (Pagani *et al.,* 2006; Zeebe *et al.,* 2016).

3.1 ASTRONOMICAL FORCING AND THE CYCLOSTRATIGRAPHIC ARCHITECTURE OF THE PALEOCENE

The Paleocene sedimentary record is pervaded by orbital cyclicity, and astronomical calibration now provides the highest-resolution chronological framework for this epoch. The 405-kyr long eccentricity cycle constitutes the primary tuning target as it remains the most stable component of Earth's orbital solution over the entire Phanerozoic (Laskar *et al.,* 2004). Between the K-Pg boundary at ~66.04 Ma and the PETM onset at ~55.93 Ma, the Paleocene encompasses approximately 24 to 25 long eccentricity cycles. Westerhold *et al.* (2008) initially proposed 24 cycles spanning the K-Pg to PETM, whilst Hilgen *et al.* (2010) advocated 25 cycles. A number of studies (e.g., Dinarès-Turell *et al.,* 2014; Clyde *et al.,* 2016) favour the 25-cycle option, yielding the now accepted K-Pg age of ~66.0 Ma and the PETM onset age of ~55.93 Ma (Zeebe and Lourens, 2019).

The most precise currently available age estimate for the K-Pg was provided by Sprain *et al.* (2019), who place it at 66.052 ± 0.008/0.043 Ma. For the PETM, Zeebe and Lourens (2019) established an age of 56.01 ± 0.05 Ma derived from their ZB18a orbital solution. Short eccentricity (~95 and ~124 kyr components) is prominently expressed in XRF Fe intensities, weight-percent $CaCO_3$, colour reflectance, and benthic foraminiferal stable isotope records from key deep-sea sites. Obliquity (~39 kyr) shows remarkably weak expression in Paleocene deep-sea records (e.g. Westerhold *et al.,* 2007; Zachos *et al.,* 2010; Littler *et al.,* 2014; Zeebe *et al.,* 2017), consistent with low-latitude forcing mechanisms operating through monsoonal precipitation and terrestrial organic carbon cycling, rather than high-latitude ice-sheet dynamics (Barnet *et al.,* 2019; Westerhold *et al.,* 2020).

Longer-period eccentricity modulations, on the million-years scale, exert profound influence on hyperthermal pacing. The ~2.4 Myr eccentricity cycle, arising from the g4-g3 orbit-orbit resonance between Mars and Earth (Laskar *et al.,* 2011), modulates the amplitude of the 95 and 124 kyr components. Lourens *et al*. (2005) demonstrated that both the PETM and the ETM-2 (Elmo) correspond to 405-kyr and 100-kyr eccentricity maxima that post-date prolonged minima in the ~2.25 Myr cycle, establishing astronomical pacing

as a key triggering mechanism for Paleogene hyperthermals. The landmark CENOGRID compilation (Westerhold *et al.,* 2020) synthesised astronomically dated benthic foraminiferal isotope records across the entire Cenozoic, placing the Paleocene within a Warmhouse climate state, characterised by eccentricity-paced carbon-cycle variability with $\delta^{13}C$ amplitudes of 0.5 to 1.0 ‰ and temperature oscillations of up to 4 °C.

3.2 CHRONOSTRATIGRAPHIC CONSTRAINTS FROM MAGNETO-, BIO- AND CHEMOSTRATIGRAPHY

3.2.1 Magnetostratigraphy

The magnetostratigraphic backbone of the Paleocene spans chrons C29r through C24r, calibrated through the Geologic Time Scale 2020 (Gradstein *et al.,* 2020), building upon Cande and Kent (1995) and astronomical tuning by Westerhold *et al.* (2008, 2020). The K-Pg boundary at 66.04 Ma falls within the reversed chron C29r, whose total duration is constrained at 587 ± 53 kyr (Sprain *et al.,* 2018). Chron C29n (~65.69 to 66.00 Ma) encompasses the earliest Danian, followed by C28r (~65.12 to 65.69 Ma) and C28n (~64.67 to 65.12 Ma). The mid-Danian is represented by the long reversed chron C27r (~63.49 to 64.67 Ma) and the normal chron C27n (~62.55 to 63.49 Ma), at whose termination the Latest Danian Event (LDE) occurs. The exceptionally long reversed chron C26r (~59.24 to 62.55 Ma; ~3.31 Myr) spans the Danian-Selandian boundary, whilst chrons C25r, C25n, and the protracted C24r (~53.90 to 57.66 Ma; ~3.76 Myr) carry the record through to the early Eocene. The PETM onset at ~56.0 Ma falls approximately 1 Myr above the top of C25n within C24r.

3.2.2 Biostratigraphy

The Paleocene calcareous nannofossil (CNP) biozonation follows the revised scheme proposed by Agnini *et al.* (2014), which replaces the traditional NP zonation with the CNP framework and employs more robust and globally correlatable bioevents. Zone CNP1 spans the post-extinction recovery phase immediately following the K-Pg event, characterised by extremely low diversity assemblages dominated by *Thoracosphaera* blooms and opportunistic *Braarudosphaera bigelowii*. Successive zones CNP2 through CNP11 document the progressive diversification of calcareous nannoplankton through the Paleocene, with key events including the base of *Discoaster mohleri* (CNP8, ~58.97 Ma), the base of *Discoaster multiradiatus* (CNP10-11 boundary, ~56.01 Ma), and the extinction of *Fasciculithus richardii* group at the PETM.Planktonic foraminiferal zonation follows Berggren and Pearson (2005) and Wade *et al.* (2011). The lowermost Danian zones P0-P1 record the progressive recolonisation of planktonic habitats. Zones P2 through P5 span the mid to late Danian and Selandian-Thanetian interval, with the Paleocene-Eocene boundary coinciding with the base of Zone E1, marked by the appearance of *Acarinina sibaiyaensis* and the benthic foraminiferal extinction event (BFEE).

3.2.3 Elemental Chemostratigraphy

Elemental chemostratigraphy derived from natural gamma-ray spectroscopy (NGR/SGR) provides supplementary palaeoenvironmental information through the behaviour of K (%), Th (ppm), and U (ppm). The Th/K ratio serves as a clay-mineralogy proxy: elevated values indicate kaolinite-smectite dominance reflecting intense chemical weathering under warm, humid conditions, whereas low values indicate illite-mica dominance characteristic of physical weathering in cooler or more arid climates (e.g., Ruffell and Worden, 2000; Schnyder *et al.,* 2006). The Th/U ratio functions as a redox indicator, with low values reflecting reducing, potentially anoxic bottom-water conditions (Myers and Wignall, 1987).

Natural gamma-ray logging data may display cyclic variations associated with orbital forcing in both marine and lacustrine environments (Grant, 2012; Boulila *et al.,* 2021). In Paleocene pelagic sequences specifically, spectral gamma-ray data from ODP Leg 208 sites at Walvis Ridge and Shatsky Rise reveal pervasive cyclicity at multiple depth scales that has proven particularly useful for cyclostratigraphic framework construction (Westerhold *et al.,* 2008; 2017; 2020). The Th/K excursion associated with the PETM at multiple sites, reflecting selective depletion of K-bearing illite during carbonate dissolution, illustrate the capacity of elemental chemostratigraphy to independently fingerprint major Paleocene palaeoenvironmental events (Littler *et al.,* 2014; Barnet *et al.,* 2019).

3.3 FROM THE K–Pg BOUNDARY TO THE PETM: MAJOR EVENTS OF THE EARLY PALEOCENE

3.3.1 The K-Pg event: Evidence of mass extinction (~66 Ma)

The Cretaceous-Paleogene (K-Pg) boundary, dated to 66.052 ± 0.008/0.043 Ma (Sprain *et al.,* 2019), marks one of the most abrupt and catastrophic events in Earth's history (Alvarez *et al.,* 1980; 1981). It is associated with a global mass extinction that eliminated nearly 75% of marine and terrestrial species, including ammonites, marine reptiles, and most morphologically complex planktonic foraminifera (Schulte *et al.,* 2010; Gradstein *et al.,* 2020). This extinction is widely linked to the impact of a ~10 km asteroid on the Yucatán Peninsula, which formed the Chicxulub crater and triggered planetary-scale climatic and ecological disturbances (Smit, 1999). Environmental consequences included global wildfires, injection of aerosols and soot into the atmosphere, and the onset of an "impact winter" that severely disrupted photosynthesis and ocean productivity (Toon *et al*., 1997; Vellekoop *et al.,* 2016; Gibbs *et al.,* 2020).

Evidence has accumulated linking the K-Pg extinction not only to the asteroid impact but also to one of the Earth's largest magmatic events in Phanerozoic, the Deccan Traps eruptions (e.g., Font *et al.,* 2016; Keller *et al.,* 2016). The Deccan Large Igneous Province (LIP), located in present-day India, erupted ~1.2 million km³ of magma over 753 ± 38 kyr, releasing vast amounts of gases and aerosols into the atmosphere (Keller, 2014; Schoene *et al.,* 2014; Renne *et al.,* 2015). In marine records, the K-Pg boundary is classically recognised as a thin, clay-rich horizon enriched in iridium, accompanied by shocked minerals, microtektites,

$\delta^{13}C$ anomalies, and abrupt faunal turnovers (Keller, 2014; Vellekoop *et al.,* 2014). Its clear global expression makes it a key chronostratigraphic marker and an important anchor point for astrochronological calibration.

3.3.2 The post K-Pg interval (~66 - 63 Ma): Catastrophe and recovery

The Chicxulub impact precipitated one of the most severe disruptions to the marine carbon cycle in the Phanerozoic. The collapse of calcareous plankton communities and the extinction of planktonic foraminiferal species substantially weakened the biological pump, resulting in the so-called Strangelove ocean (Hsü and McKenzie, 1985), characterised by the near-total elimination of the surface-to-deep $\delta^{13}C$ gradient (Henehan *et al.,* 2019). The recovery proceeded in distinct phases that were spatially heterogeneous and temporally protracted: the biological pump recovered functionally by ~1.8 Myr post-impact (~64.2 Ma), but ecological trait recovery required approximately 4.3 Myr (~61.7 Ma) (Birch *et al.,* 2016, 2021).

Within this recovery interval, the Dan-C2 event at ~65.2 Ma represents the earliest Paleocene hyperthermal, occurring approximately 800 kyr after the K-Pg boundary at the top of Magnetozone C29r. It is characterised by a conspicuous double negative excursion in $\delta^{13}C$ (~1.0-1.3 ‰) and $\delta^{18}O$ spanning approximately 100 kyr, a timespan suggestive for the short-eccentricity control. The Dan-C2 coincides with the first 405-kyr eccentricity maximum of the Paleocene (Pc405-1; Barnet *et al.,* 2019), and recent evidence favours orbital forcing over Deccan volcanism as the primary trigger (Ma *et al.,* 2024).

3.3.3 The Latest Danian Event and the Danian-Selandian Transition (~62.5 - 61 Ma)

The Latest Danian Event (LDE), dated between ~61.75 and ~62.2 Ma (Westerhold *et al.,* 2008, 2011; Dinarès-Turell *et al.,* 2014), constitutes the first unambiguous Cenozoic hyperthermal recorded throughout the full water column. Named by Bornemann *et al.* (2009) from Nile Basin sections in Egypt, the LDE is positioned at the very top of magnetic chron C27n, at the C27n to C26r polarity reversal. The event exhibits a distinctive twin-peaked structure: two negative $\delta^{13}C$ excursions of up to ~1 ‰ separated by a brief recovery, with a total duration of approximately 200 kyr. At Shatsky Rise ODP Site 1210, planktonic foraminifera record $\delta^{13}C$ drops of ~0.7 ‰ and $\delta^{18}O$ decreases of ~0.6 ‰, corresponding to whole-water-column warming of 2 to 3 °C (Jehle *et al.,* 2015, 2019). Harbich *et al.* (2024) confirmed pulsed sea-surface temperature increases of ≥1.5 °C and documented synchronous declines in planktonic and benthic B/Ca ratios, indicating carbonate system perturbation consistent with ocean acidification.

The Danian-Selandian boundary at ~61.6 Ma is defined by the GSSP at Itzurun beach, Zumaia, ratified by the IUGS in September 2008 (Schmitz *et al.,* 2011). The GSSP is placed at the abrupt lithological change between the limestone-dominated Aitzgorri Limestone Formation and the overlying grey marls of the Itzurun Formation, 49 m above the K-Pg boundary. The Danian-Selandian Transition Event (D/STE) comprises coupled negative $\delta^{13}C$ and $\delta^{18}O$ excursions, indicative of warming and carbon-cycle perturbation at the boundary (Arenillas *et al.,* 2008; Barnet *et al.,* 2019).

3.3.4 The Mid-Paleocene Biotic Event, Carbon Isotope Maximum, and Sea-Level Dynamics (~59 - 57.5 Ma)

The late Paleocene is characterised by a distinctive interval of isotopic decoupling between $\delta^{13}C$ and $\delta^{18}O$, spanning approximately 59.7 to 58.1 Ma and known as the Paleocene Oxygen Isotope Maximum (POIM; Hollis *et al.,* 2022). During this interval, benthic $\delta^{18}O$ values remain elevated, reflecting relatively cool conditions, while $\delta^{13}C$ rises toward its Cenozoic maximum, the Paleocene Carbon Isotope Maximum (PCIM).

The onset of the POIM broadly coincides with the Mid-Paleocene Biotic Event (MPBE), equivalent to the Early Late Paleocene Event (ELPE; Coccioni *et al.,* 2012, 2019; Hyland *et al.,* 2015), a short-lived climatic perturbation at ~59.2 Ma that constitutes the terminal phase of the Selandian-Thanetian Transition Event (STTE). This event is expressed as a ~1 ‰ negative $\delta^{13}C$ excursion accompanied by a ~30% decrease in $CaCO_3$ content, interpreted as lysocline shoaling driven by the injection of isotopically depleted carbon into the ocean-atmosphere system. The core of the perturbation lasted approximately 10-11 kyr, with the broader event spanning ~52-53 kyr based on precession-cycle counting (Bernaola *et al.,* 2007). The Selandian-Thanetian boundary (~59.24 Ma) is defined at the Global Boundary Stratotype Section and Point (GSSP) at Zumaia, at the base of magnetochron C26n.

Following the MPBE/ELPE, $\delta^{13}C$ continues to rise, reaching its long-term maximum during the PCIM at approximately 57.7–57.8 Ma within chron C25r (Littler *et al.,* 2014), with benthic values of ~2.0 to 2.5 ‰ VPDB, among the highest of the Cenozoic. The POIM interval overlaps with the PCIM and reflects a period of transient cooling associated with enhanced organic carbon burial (Hollis *et al.,* 2022).

The termination of the POIM at ~58.15 Ma is marked by an unnamed carbon isotope excursion ("*" event; Littler *et al.,* 2014; Barnet *et al.,* 2019; Hollis *et al.,* 2022). Notably, this event occurs during a minimum in eccentricity forcing, within a ~1 Myr decline initiated at the ELPE eccentricity maximum, rather than at an eccentricity maximum, as is typical of classical Paleocene hyperthermals (Hollis *et al.,* 2022). This orbital configuration distinguishes it mechanistically from events such as the Dan-C2, Latest Danian Event (LDE), and the Paleocene-Eocene Thermal Maximum (PETM), and the absence of robust evidence for deep-water warming in benthic $\delta^{18}O$ records argues against its classification as a hyperthermal *sensu stricto*.

The "*" event was further characterised by Hollis *et al.* (2022) in the context of Waipawa organofacies deposition in the southwest Pacific, where a second organic-rich layer approximately 5 m above the main ELPE deposit was correlated to this perturbation. The identification of coeval positive HTHO anomalies at both IODP holes investigated in this study provides new constraints from the Indian Ocean on the expression of this global event.

3.3.5 Late Paleocene Warming and Pre-PETM Destabilisation of the Carbon Cycle (~58 - 56 Ma)

From approximately 58 Ma onward, the deep-ocean $\delta^{18}O$ record documents a progressive warming trend that would culminate in the Early Eocene Climatic Optimum (EECO). Benthic foraminiferal $\delta^{18}O$ values

declined from ~0.5 ‰ to approximately -0.5 ‰ VPDB over this interval, corresponding to deep-water warming of ~4 to 5°C and absolute bottom-water temperatures of ~8 to 12°C immediately prior to the PETM (Zachos *et al.,* 2001, 2008). The North Atlantic Igneous Province (NAIP) emerges as the principal driver of late Paleocene warming. NAIP activity proceeded in two main phases: Phase 1 at ~61 Ma (associated with initial rifting) and Phase 2 at ~56 Ma (linked to continental breakup and the opening of the northeast Atlantic), with total volcanic volumes possibly exceeding ~6.6 million km³ (Saunders, 2016).

The Pre-Onset Excursion (POE), occurring tens of thousands of years before the main PETM carbon isotope excursion, was first documented by Bowen *et al.* (2015) in pedogenic carbonates from the Bighorn Basin, Wyoming, and subsequently confirmed in marine records. Earth system modelling indicates the POE was driven by largely thermogenic CO_2. Babila *et al.* (2022) observed a 1.0-1.5 ‰ negative $\delta^{13}C$ excursion with ~2 °C sea-surface warming and a decline in ocean pH, establishing a direct causal link between NAIP volcanism and early warming that preceded the main PETM CIE.

3.3.6 The Paleocene-Eocene Thermal Maximum and Conditions Extending to 54 Ma

The PETM (56.01 ± 0.05 Ma; Zeebe and Lourens, 2019) represents the most extreme transient warming event of the Cenozoic and coincides with the Paleocene-Eocene boundary. The event is characterised by a massive negative carbon isotope excursion (CIE), rapid global warming, and profound biotic disruption. The CIE magnitude varies systematically among substrates: ~2 ‰ in bulk marine carbonate, ~2.5 to 4 ‰ in benthic foraminifera, and up to 6 to 7 ‰ in terrestrial organic matter and pedogenic carbonates (Koch *et al.,* 1992; McInerney and Wing, 2011). Global mean temperature rose by 5 to 8°C (McInerney and Wing, 2011), and deep-sea temperatures increased by 4 to 6°C (Tripati and Elderfield, 2005). The total duration of the PETM is constrained at ~150 to 200 kyr (Röhl *et al.,* 2007).

The benthic foraminiferal extinction event (BFEE), during the PETM, represents the most severe benthic crisis of the Cenozoic, with 30 to 50% of species lost within <10 kyr (Thomas, 1998, 2007). Zachos *et al.* (2005) documented CCD shoaling of >2 km in the South Atlantic, producing a prominent clay layer representing complete $CaCO_3$ dissolution at deeper sites. Recovery from the PETM was mediated by enhanced silicate weathering and organic carbon sequestration (Bowen and Zachos, 2010). Post-PETM, warming continued into the EECO, with orbitally paced hyperthermals (ETM-2, H-2, ETM-3; Zachos *et al.,* 2010) demonstrating the sustained operation of eccentricity-paced carbon-cycle oscillations through the early Eocene.

4 GEOLOGICAL CONTEXT:

The International Ocean Discovery Program (IODP) has played a central role in the efforts aiming to reconstruct past environmental changes. By recovering sediment cores from diverse oceanic regions, IODP expeditions have generated extensive and publicly available scientific datasets that underpin chronostratigraphic, biostratigraphic, magnetostratigraphic, and cyclostratigraphic studies (e.g., Huber et al., 2019; Uenzelmann-Neben et al., 2023). Pelagic marine environments, characterised by relatively continuous and well-preserved sedimentation, are particularly well suited for cyclostratigraphic analysis (Weedon, 2003; Hinnov, 2013). As discussed previously, the Paleocene interval, spanning the K-Pg boundary (~66 Ma) to the PETM (~56 Ma), represents a critical window for investigating the interplay among orbital forcing, carbon cycle dynamics, and climate evolution in the early Cenozoic. The two IODP sites investigated in this study, Hole U1514C on the western Australian margin (Expedition 369) and Hole U1579D on the Agulhas Plateau (Expedition 392), were selected because they preserve continuous Paleocene pelagic carbonate sequences in the Indian Ocean sector, a region that, as noted above, remains underrepresented in cyclostratigraphic frameworks in relation to classical reference sections at Walvis Ridge, Shatsky Rise, and Zumaia. The following sections describe the geological and tectonic settings, paleoceanographic context, and stratigraphic characteristics of each hole, providing the background necessary to contextualise the cyclostratigraphic analysis presented in subsequent chapters.

4.1 IODP EXPEDITION 392 - AGULHAS PLATEAU, SOUTH INDIAN OCEAN

IODP Expedition 392 (Uenzelmann-Neben *et al.,* 2023), conducted between February and April 2022, targeted the southwest Indian Ocean, focusing on the Agulhas Plateau and Transkei Basin at paleolatitudes of 53° to 61° S during the Late Cretaceous (Figure 1). The main objective was to investigate the long-term climate transition from the Cretaceous greenhouse to the late Paleogene icehouse, aiming to improve understanding of southern high-latitude Earth system dynamics during large fluctuations in global temperature and atmospheric CO_2 (Uenzelmann-Neben *et al.,* 2023).

The expedition goals were to:

(1) Evaluate whether the Indian Ocean LIPs associated with the breakup of Gondwana originated from a similar mantle source and exhibited comparable temporal and geochemical evolution to coeval and older Pacific LIPs;

(2) Determine if sedimentation on the Agulhas Plateau commenced immediately after crustal emplacement at approximately 100 Ma under subaerial conditions;

(3) Investigate whether bottom currents linked to deep and intermediate water masses, as well as climatic events, are recorded in the sedimentary succession as seismic reflections and unconformities;

(4) Reconstruct the paleotemperature evolution at southern high latitudes across the rise and decline of the Cretaceous supergreenhouse and throughout the early Paleogene;

(5) Assess how the progressive opening of the African-Southern Ocean gateway influenced ocean circulation from the Cretaceous to the Paleogene;

(6) Identify the forcing mechanisms responsible for the Cretaceous Oceanic Anoxic Events (OAEs) and evaluate their impact on high-latitude climate, oceanography, and biota.

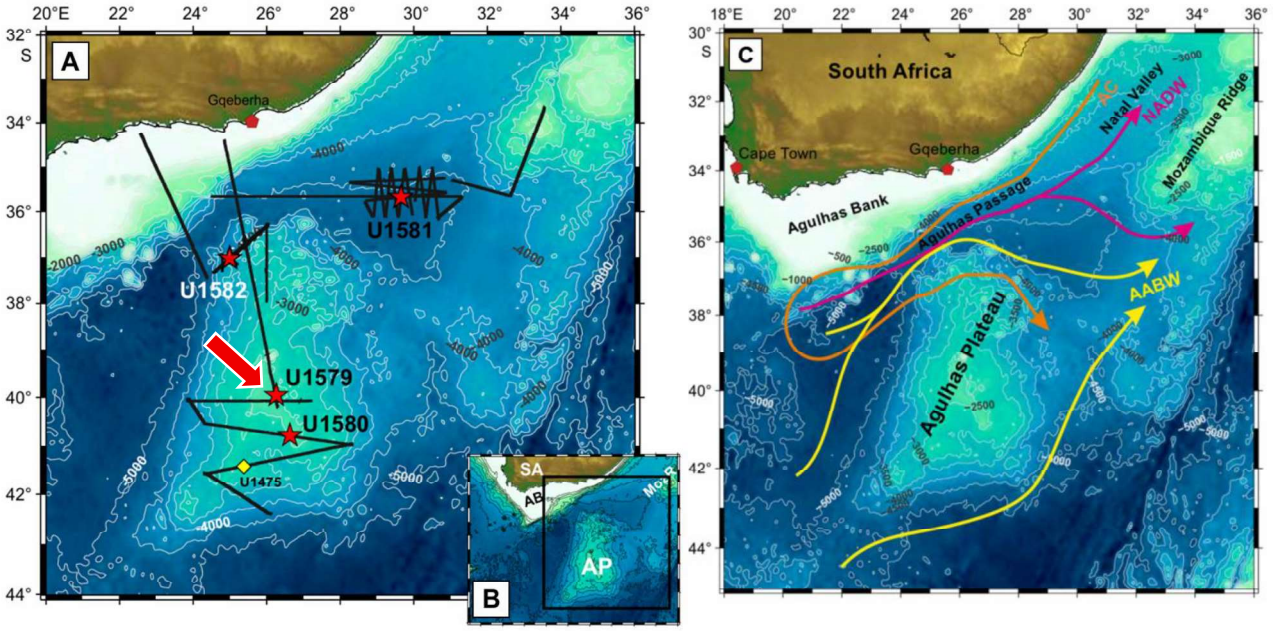


Figure 1 – **A**. Bathymetry of the Agulhas Plateau (AP) (Sandwell and Smith, 1997). Expedition 392 sites are marked as red stars on seismic lines (black lines) (Uenzelmann-Neben, 1998, 2005, 2014). Red arrow = Site U1579; Yellow diamond = Expedition 361 Site U1475 (Gruetzner *et al*., 2019; Hall *et al*., 2017); **B**. Auxiliary map showing the broader location of the expedition's area in which abbreviations stand for: SA = South Africa; AB = Agulhas Bank; MOZR = Mozambique Ridge. **C**. Currents and water masses active in the African-Southern Ocean gateway: AC = Agulhas Current; NADW = North Atlantic Deep Water; AABW = Antarctic Bottom Water. Modified from Uenzelmann-Neben *et al.* (2023).

4.1.1 Geological and paleoceanographic setting

During the Early Cretaceous, South America, Africa, and Antarctica were joined as part of Gondwana, and the African-Southern Ocean gateway did not yet exist. Around 146 Ma, breakup initiated, leading to the formation of two major oceanic plateaus: the Mozambique Ridge (~136 to 120 Ma) and the Agulhas Plateau (105 to 95 Ma). These bathymetric highs acted as barriers to deep and intermediate water circulation (König and Jokat, 2010). The separation of the Falkland Plateau from Africa between ~120 and 100 Ma opened the Indian Ocean; however, large igneous provinces (LIPs) such as the Agulhas Plateau, the Northeast Georgia Rise, and Maud Rise continued to restrict deep and intermediate water flow until ~94 Ma, when tectonic subsidence allowed deeper connections.

4.1.2 Seismostratigraphic framework

Pre-expedition seismic studies (Tucholke and Carpenter, 1977; Tucholke and Embley, 1984), identified distinct seismic horizons above basement (Figure 2). Expedition 392 results confirmed and refined

this seismostratigraphic model, anchoring the reflectors with direct biostratigraphic and magnetostratigraphic constraints.

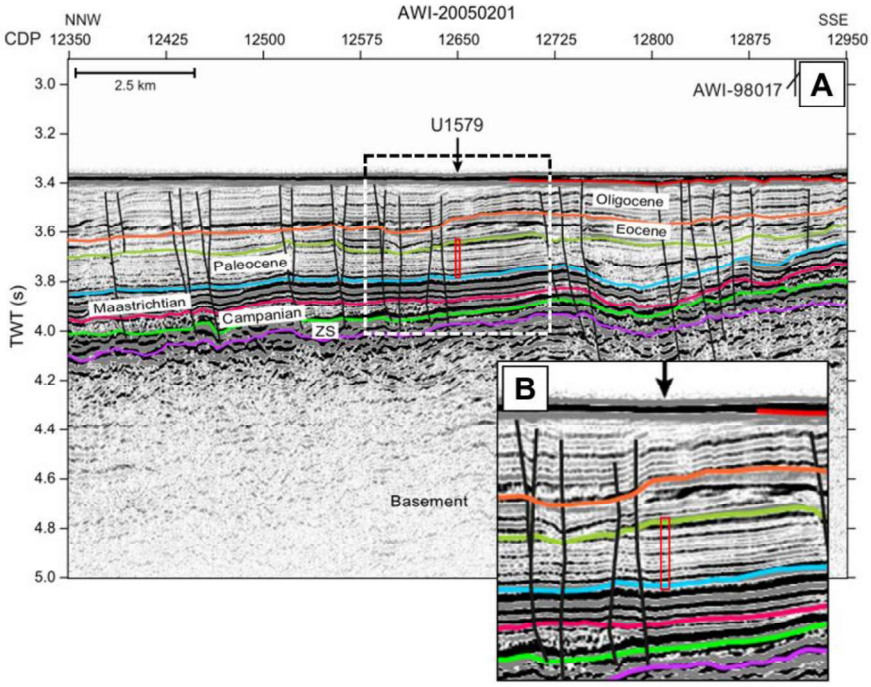


Figure 2 – **A**. location of Site U1579 over seismic Line AWI-20050201. Preliminary interpretation of seismic units according to the chronostratigraphic model is shown. CDP = common depth point, TWT = two-way traveltime, ZS = zeolitic silicified sediments (Uenzelmann-Neben *et al*., 2023); **B.** Zoom of the highlighted area within dashed white limits for better visualization of the studied interval marked approximately by red hollowed polygon.

4.1.3 K-Pg / PETM interval on Hole U1579D

The studied interval at Hole U1579D is entirely assigned to lithostratigraphic Unit II, specifically Subunit IIb, a ~407 m thick succession of white to light greenish-gray nannofossil chalk with variable clay content. Within Unit II, calcareous nannofossils are abundant and generally moderately to well preserved, providing high biostratigraphic resolution throughout the Paleocene (Uenzelmann-Neben *et al.,* 2023). Planktonic foraminifera are also common and well preserved. Benthic foraminiferal assemblages are consistently indicative of bathyal paleodepths, with well-oxygenated bottom-water conditions throughout the Paleocene section.

Between the K-Pg boundary and the basal Eocene, 13 nannofossil biohorizons and 6 paleomagnetic reversals provide robust age control. Apart from the PETM gap between Cores 16R and 17R (271.30-267.19 m CSF-A), the Paleocene succession is continuous, with an average sedimentation rate of ~1.7 cm/kyr. The K-Pg boundary is located at 433.2 m CSF-A (Core 33R), where the white nannofossil chalk is interrupted by a complex, ~2 m thick clay-rich sequence (Figure 3).

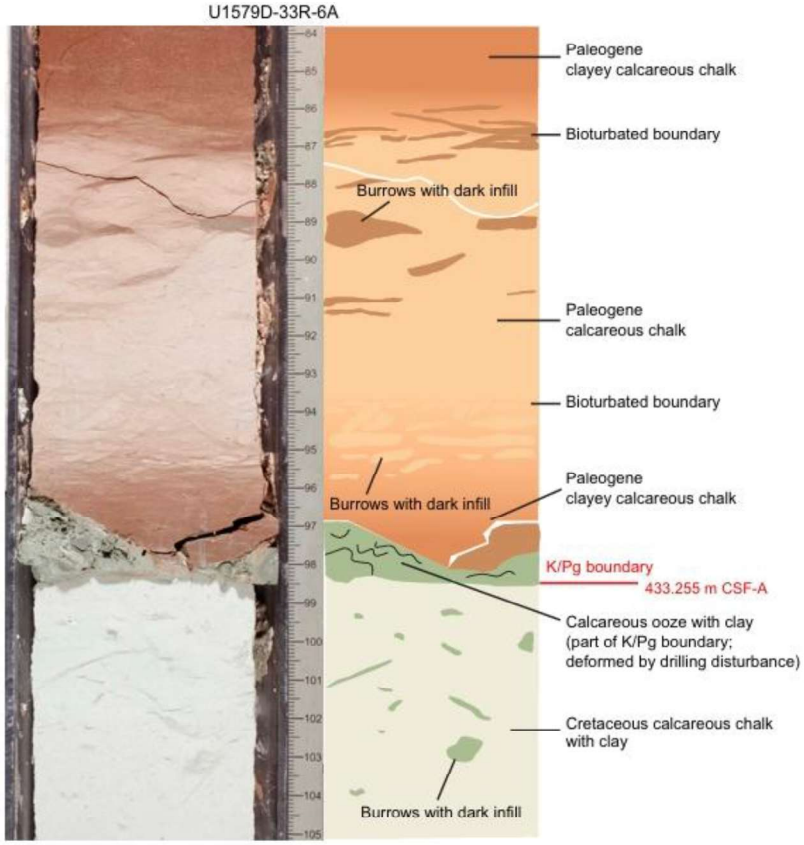


Figure 3 - Schematic of the K/Pg boundary, Hole U1579D: The boundary is characterised by a sharp color change at 33R-6A, 96 to 99 cm, from reddish-brown clayey calcareous chalk to grayish-green calcareous chalk with clay. The interval is affected by drilling-related deformation and includes a narrow (~1 cm) greenish-gray layer of calcareous ooze with clay (Uenzelmann-Neben *et al*., 2023).

The boundary is characterised by a sharp colour change at 33R-6A (96 to 99 cm), from reddish-brown clayey calcareous chalk to grayish-green calcareous chalk with clay, affected by drilling-related deformation and including a narrow (~1 cm) greenish-gray layer of calcareous ooze with clay (Uenzelmann-Neben *et al.,* 2023). The absence of distinct changes in sediment colour or physical properties between the top of Core 17R and the base of Core 16R indicates that the Paleocene-Eocene boundary itself is not preserved in the recovered section; however, the occurrence of *Rhomboaster bramlettei* at 267.1 m CSF-A suggests that part of the PETM recovery interval may still be represented.

4.2 IODP EXPEDITION 369 - MENTELLE BASIN, WESTERN AUSTRALIA

IODP Expedition 369 (Huber *et al.,* 2019), conducted between September and November 2017, targeted the western Australian margin to investigate the Cretaceous and Cenozoic tectonic and paleoceanographic evolution of the Great Australian Bight (GAB) and the Mentelle Basin (MB). The MB, adjacent to the Naturaliste Plateau, was a primary focus due to its potential for preserving high-latitude climate records (~60° S paleolatitude during the Cretaceous; Figure 4).

The expedition goals were to:

(1) Investigate the timing and causes for the rise and collapse of the Cretaceous supergreenhouse and how this climate shift affected the climate-ocean system and oceanic biota;

(2) Determine the relative roles of productivity, ocean temperature, and ocean circulation at high southern latitudes during Cretaceous OAEs;

(3) Identify the main source regions for deep-water and intermediate water masses in the southeast Indian Ocean and how these changed during Gondwana breakup;

(4) Characterize how oceanographic conditions changed at the Mentelle Basin during the Cenozoic opening of the Tasman Gateway and restriction of the Indonesian Gateway;

(5) Resolve questions about the volcanic and sedimentary origins of the basin and provide stratigraphic control on the age and nature of the pre-breakup succession.

Drilling at Site U1514 recovered an expanded Pleistocene-Eocene sequence and penetrated into upper Albian strata. Notably, the Cenomanian-Turonian section contained deformed sedimentary rocks interpreted as a décollement zone (Huber *et al.,* 2019). The recovered pelagic carbonate sequences provided a well-resolved age framework, enabling high-resolution stratigraphic reconstructions and more precise correlations between global climate shifts and regional tectonic history. These data contribute to understanding the rise and decline of the Cretaceous greenhouse climate, as well as changes in latitudinal thermal gradients and deep-ocean circulation through the Cenozoic (Huber *et al*., 2019).

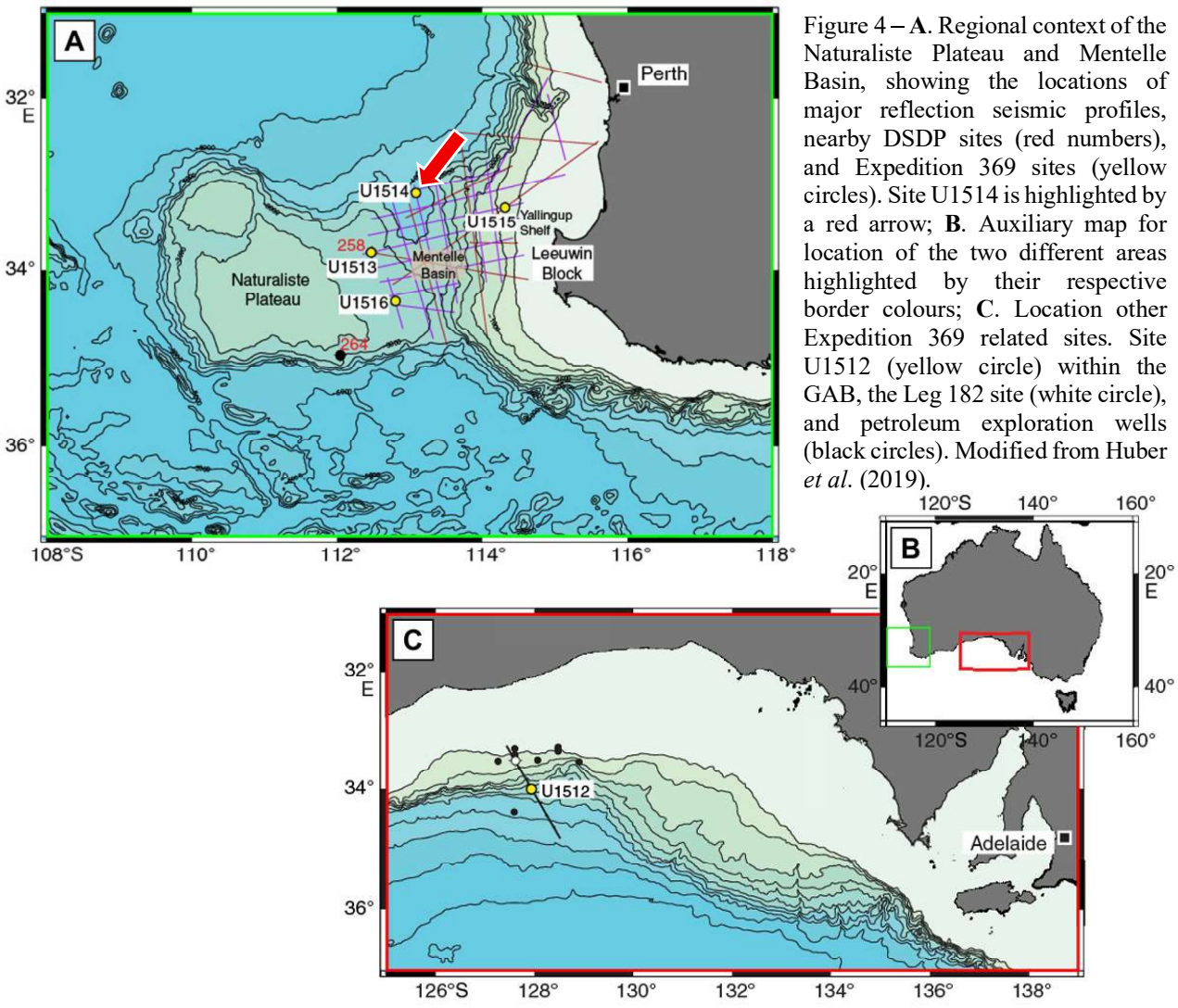


Figure 4 – **A**. Regional context of the Naturaliste Plateau and Mentelle Basin, showing the locations of major reflection seismic profiles, nearby DSDP sites (red numbers), and Expedition 369 sites (yellow circles). Site U1514 is highlighted by a red arrow; **B**. Auxiliary map for location of the two different areas highlighted by their respective border colours; **C**. Location other Expedition 369 related sites. Site U1512 (yellow circle) within the GAB, the Leg 182 site (white circle), and petroleum exploration wells (black circles). Modified from Huber *et al.* (2019).

4.2.1 Geological and tectonic setting

During the Early Cretaceous, at the onset of eastern Gondwana breakup, the Naturaliste Plateau was positioned at ~60° S, near the junction of the Australian, Antarctic, and Greater India plates. The Mentelle Basin formed along the western Australian margin during detachment from India, isolating the Naturaliste Plateau from mainland Australia (Bradshaw *et al.,* 2003). The plateau is interpreted as a volcanic margin, coeval with the onshore Bunbury Basalt, dated to 137 to 130 Ma (Direen *et al.,* 2017). Regional seismic surveys (Figure 5) revealed Neogene carbonate oozes unconformably overlying Paleogene deep-marine chalk, punctuated by thin chert layers, beneath which lies Cretaceous coccolith-rich chalk underlain by Albian-Aptian claystones and glauconitic sandstones.

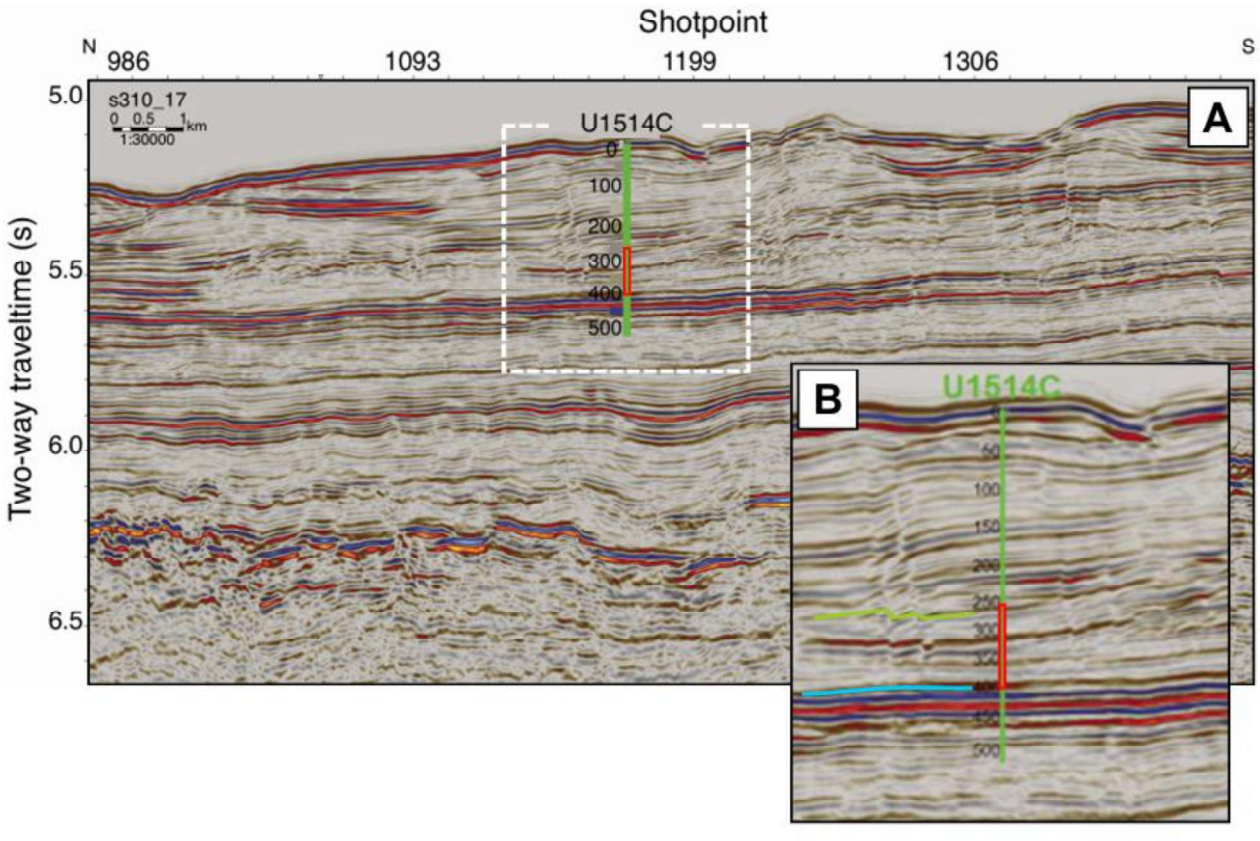


Figure 5 – **A**. Time-migrated Geoscience Australia reflection seismic with location of Site U1514 marked along seismic shotpoints (Huber *et al*., 2019); **B**. Zoom of the highlighted area within dashed white limits for better visualization of the studied interval marked approximately by red hollowed polygon. Green line along seismic reflector represents the upper limit, possibly related to the Paleocene/Eocene boundary while light blue line to the bottom of the studied sequence represents the Paleocene/Maastrichtian boundary. Modified from Huber *et al*. (2019).

4.2.2 Rift evolution and paleogeography

While the breakup of Greater India is considered volcanic in nature, the southern margin of Australia experienced slow, magma-poor rifting beginning between the Cenomanian and Turonian (Direen *et al.,* 2011). This process formed the GAB basin at the eastern end of the Australo-Antarctic Gulf (AAG), which hosted the largest continental margin deltaic sequences of the Late Cretaceous greenhouse period. In the early

Paleogene, transgressive sedimentation gave way to open-marine carbonate shelf conditions from the early Eocene onward. These plate reorganisations significantly influenced global deep-water circulation. The restriction of deep-water exchange in the nascent Indian Ocean persisted until two major Cenozoic events: the opening of the Tasman Gateway (middle Eocene-early Oligocene) and the restriction of the Indonesian Gateway (Miocene-Pliocene) (Huber *et al.,* 2019).

4.2.3 K-Pg / PETM interval on Hole U1514C

The studied interval at Hole U1514C corresponds primarily to lithological Unit II, a 308 m thick succession of nannofossil chalk with clay, with the uppermost ~10 m assigned to Unit III. The sedimentary record from the late Maastrichtian through the early Oligocene exhibits a nearly continuous sediment accumulation rate (SAR) of ~1.4 cm/kyr, consistent with values reported for other deep-water successions (Huber *et al.,* 2019). Several calcareous nannofossil and foraminiferal taxa were employed as datums to establish the chronological framework, complemented by paleomagnetic reversal stratigraphy.

Between 250 and 260 m CSF-A (Core 9R), sediments shift in colour from light greenish gray to pale yellow/light yellowish brown, coinciding with an NGR spike associated with U enrichment and U/Th ratios >1, potentially linked to the PETM. The highest occurrence of *Stensioeina beccariiformis*, dated to 55.81 Ma, whose extinction is a recognised marker of the Paleocene-Eocene boundary, is recorded in Sample 369-U1514C-11R (Huber *et al.,* 2019). The lowermost Paleocene is recorded in Core 23R, with assemblages of *Biantholithus sparsus*, *Cyclagelosphaera reinhardtii*, *Neocrepidolithus cruciatus*, and *Thoracosphaera spp*., together with reworked Upper Cretaceous taxa. At ~395.6 m WMSF, NGR values peak ~2 m below the K-Pg boundary, within Chron C30n, while U concentrations exceed 10 ppm (~20 times the mean for the hole), marking the characteristic geochemical signature of the K-Pg clay.

5 THE MILANKOVITCH CYCLES

5.1 THE CLIMATIC SPECTRUM

Earth's climate emerges from the interaction of multiple subsystems, oceans, cryosphere, biosphere, and atmosphere, that operate across vastly different timescales, generating variations of diverse amplitude and frequency (Berger *et al.,* 1992). This set of variations, spanning periods from minutes to billions of years, can be represented by a climatic power spectrum, whose features express both the internal variability of the system and the external influences acting upon it (Mitchell, 1976; Von der Heydt *et al.,* 2021). Sedimentary geological records constitute the primary repository of long-term climate changes, preserving signals of factors such as atmospheric carbon dioxide concentration, solar radiation intensity, and plate tectonic dynamics (Weedon, 2003; Meyers, 2019).

According to Ruddiman (2001), the fundamental climate forcings can be organised into three main temporal domains: (i) tectonic processes, operating on timescales of millions of years, which reshape the distribution of continents and ocean basins and modulate atmospheric and oceanic circulation over the long term; (ii) variations in Earth's orbital parameters, with periodicities between 10^4 and 10^6 years, which control the distribution of solar energy received by the planet; and (iii) fluctuations in solar luminosity, with impacts over short to medium timescales. These mechanisms interact non-linearly, producing the complex structure observed in the climatic spectrum.

Within the climate system itself, quasi-periodic phenomena of internal origin contribute energy at specific spectral frequencies. Among these, the El Nino-Southern Oscillation modulates sea surface temperatures across the equatorial Pacific with an average recurrence of 3 to 7 years (Philander, 1990), while the Quasi-Biennial Oscillation of the tropical stratosphere exhibits a mean period of approximately 28 months (Newman *et al.,* 2016). At decadal to multidecadal scales, the Pacific Decadal Oscillation adds variability in intervals of 15-25 and 50-70 years (Mantua and Hare, 2002). At the low-frequency end of the spectrum lie the long-scale astronomical forcings, the Milankovitch cycles, classified among the external deterministic sources acting on the climate system (Crucifix *et al.,* 2006).

An updated representation of this spectrum, proposed by Von der Heydt *et al.* (2021), illustrates how periodic (orbital) and episodic (volcanism, impacts, solar variability) forcings act on different climatic subsystems, whose internal responses amplify or attenuate the signals according to the dynamic properties of each component. In the context of cyclostratigraphy, it is particularly relevant to recognise that Milankovitch orbital cycles occupy a privileged position in this spectrum by combining high amplitude, well-defined periodicities, and stability across geological time, properties that underpin their widespread use as the primary framework for astrochronological calibration.

5.2 ORBITAL CYCLES AND CLIMATE FORCING

The astronomical theory of palaeoclimates, systematised in 1941 by the Serbian mathematician Milutin Milankovitch (1879-1958), postulates that long-term variations in Earth's orbital parameters constitute

the primary forcing of the climatic oscillations recognised in the geological record. According to this theory, changes in the geometry of Earth's orbit and in the orientation of its rotational axis produce variations in the amount and latitudinal distribution of received solar radiation, the so-called insolation variations, which in turn modulate the global climate system over characteristic timescales of between 10^4 and 10^6 years (Hilgen *et al.,* 2004; Strasser *et al.,* 2006; Hinnov, 2013). These processes are governed by three orbital parameters: (i) eccentricity (e); (ii) obliquity ($\in$); and (iii) longitude of perihelion relative to the moving equinox ($e \sin \psi$) (Hinnov and Hilgen, 2012; see Figure 6).

Eccentricity describes the degree of ellipticity of Earth's orbit around the Sun, that is, the variation between more nearly circular and more elongated trajectories, and is quantified by the relation presented in Equation . The characteristic periods of this parameter are approximately 405 kyr and ~100 kyr (with components at ~95, ~99, ~125 and ~131 kyr), in addition to a very long-period modulation of ~2.4 Myr (Hinnov and Hilgen, 2012; Hinnov, 2018). Eccentricity does not alter the total insolation received over the course of a year, but modifies its seasonal distribution, amplifying or attenuating the contrast between seasons.

$$e = \frac{(a^2 - b^2)^{1/2}}{a} \qquad \textit{Equation 1}$$

where a and b correspond to the semi-major and semi-minor axes of the Earth's orbital ellipse, respectively.

Obliquity ($\in$) refers to the tilt of Earth's rotational axis relative to the plane of its orbit, varying cyclically according to the Equation 2. Its current mean period is approximately 41 kyr, with additional components near 54, 40, and 29 kyr (Hinnov and Hilgen, 2012; Kodama and Hinnov, 2014). By controlling the tilt of Earth's rotational axis, obliquity governs the latitudinal contrast in solar insolation and the intensity of the seasons, exerting a particularly pronounced influence at high latitudes.

$$\in = \in^* + \sum A_i \cos(f_i t + \delta_i) \qquad \textit{Equation 2}$$

where $\in^*$ is the mean value; A_i are the amplitudes; f_i are the orbital eccentricity frequencies – combinations of the secular frequencies g_i where subscript "i" are the planets (e.g., Laskar 2020); δ_i is the fundamental phase.

Precession results from the combination of two motions: axial precession, the conical rotation of Earth's rotational axis, analogous to the wobble of a spinning top, and apsidal precession, the rotation of the orbital plane itself. The precession index ($e \sin \psi$) represents the combined effects of these two motions on the Earth-Sun distance throughout the year, with principal periods of ~23, ~22, ~19, and ~18 kyr (Berger and Loutre, 1994; Hinnov and Hilgen, 2012). Precession controls which hemisphere experiences summer at the orbital position of closest approach to the Sun (perihelion), thereby modulating hemispheric seasonality.

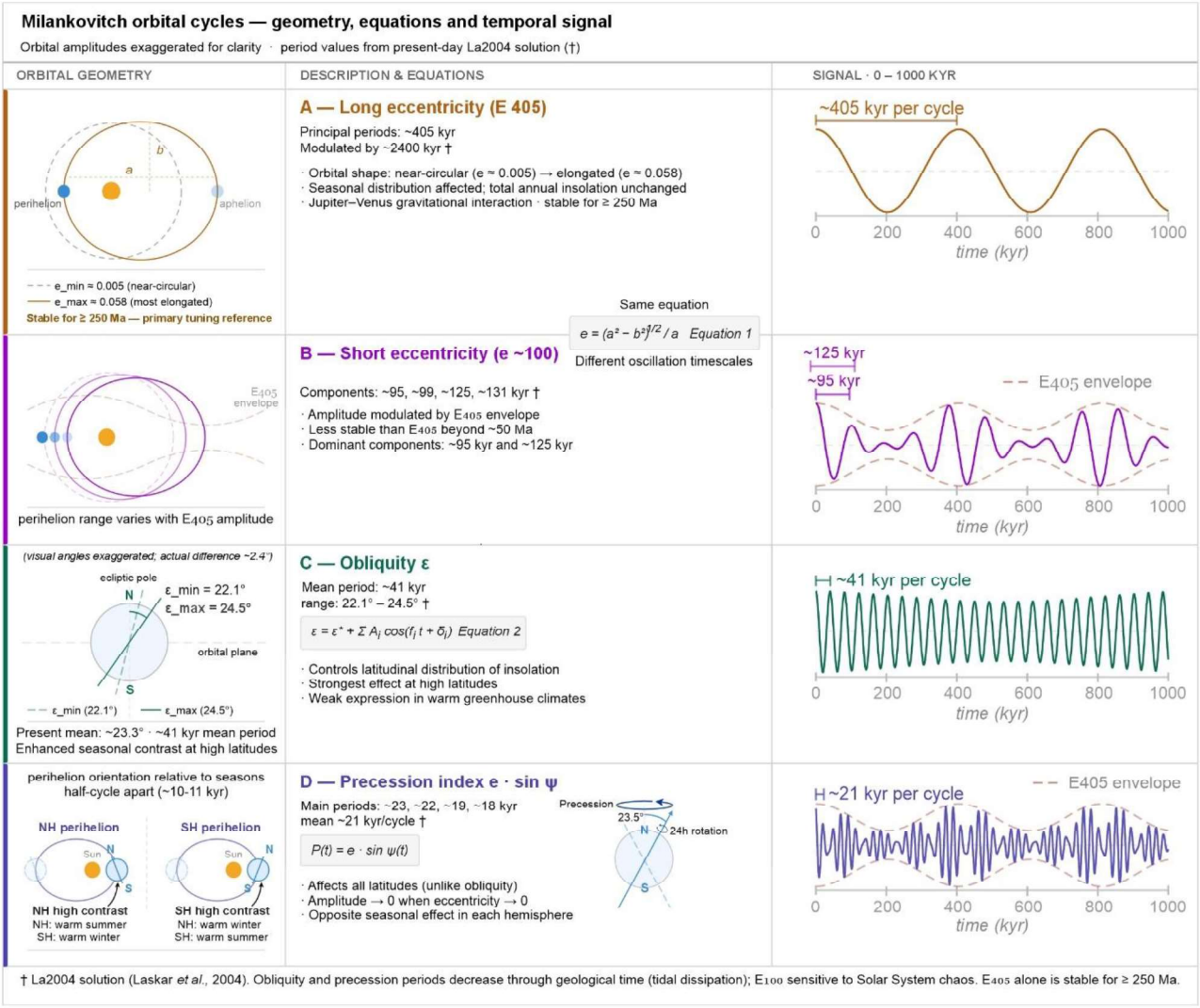


Figure 6 – Schematic representation of the three Milankovitch orbital parameters and their characteristic temporal signals over a 1 Myr window. **A**. 405 kyr Long eccentricity and **B**. ~100 kyr Short eccentricity: a single parameter expressed across two frequency bands, the long eccentricity (E_{405}, ~405 kyr), driven by the Jupiter-Venus gravitational interaction and stable for ≥ 250 Myr, and the short eccentricity (E_{100}, ~95–131 kyr), whose amplitude is modulated by the E_{405} envelope. **C**. Obliquity (ε): cyclic variation in the tilt of Earth's rotational axis relative to its orbital plane (~41 kyr; range 22.1°-24.5°), governing latitudinal insolation contrasts. **D**. Precession index (e sin ψ): combined effect of axial and apsidal precession (~21 kyr mean period), controlling which hemisphere experiences summer at perihelion and affecting all latitudes. Orbital geometries are exaggerated for clarity. Period values correspond to present-day orbital modelling (La2004 solution; Laskar *et al*., 2004).

A fundamental caveat for the practical application of these cycles is that the periodicities of orbital parameters have not remained constant throughout geological time. Factors such as tidal energy dissipation in the Earth-Moon system, responsible for the gradual recession of the Moon, variations in Earth's dynamic ellipticity, and the chaotic behaviour of the Solar System introduce secular perturbations into orbital frequencies (Berger *et al.,* 1989, 1992; Hinnov and Hilgen, 2012; Farhat *et al.,* 2022; Wu *et al.,* 2024). As a consequence of mainly tidal dissipation, the rate of precession has progressively decelerated in time toward the present, which is reflected in slightly different values for the obliquity-precession cycles relative to their present-day equivalents. However, since the percentage variation of obliquity and precession periodicities is

relatively small over intervals of ~100 Myr, these periods can be treated as practically constant in studies operating within temporal windows of this order (Weedon, 2003).

In contrast to the instability of the short eccentricity cycle (~100 kyr), whose frequencies are strongly influenced by the chaotic behaviour of the Solar System, the long eccentricity cycle of ~405 kyr exhibits remarkable stability for at least ~250 Myr into the geological past (Laskar *et al.,* 2004, 2011; Hinnov and Hilgen, 2012; Zeebe and Lantink, 2024). This stability arises primarily from the gravitational interaction between Jupiter and Venus, specifically from the displacement of their orbital perihelions, whose effects are maintained by the large Jovian mass. Owing to this exceptional property, the E405 cycle has become the preferred astronomical metronome in cyclostratigraphic studies, particularly for Mesozoic and older intervals where high-precision astronomical solutions are no longer directly applicable (Laskar *et al.,* 2004, 2011; Hinnov and Hilgen, 2012; Kent *et al.,* 2018). Indeed, the stability of E405 is the principal justification for its use as the primary tuning reference throughout the present study.

6 METHODS AND PROCEDURES

6.1 GAMMA RAY WELL LOGGING: NGR, U, TH AND K

Natural Gamma Radiation (NGR) logging is a widely used, non-destructive technique in sedimentological studies for detecting lithological variations (Goldberg, 1997). The technique measures gamma-ray emissions from naturally occurring radioactive isotopes in sediments, primarily potassium (^{40}K), uranium (^{238}U), and thorium (^{232}Th) and their decay products. In marine sediments, these elements are primarily associated with clay minerals, detrital heavy minerals, and, in the case of uranium, organic matter adsorption under reducing conditions (e.g., Myers and Wignall, 1987; Osmond and Ivanovich, 1992; Li *et al.,* 2019).

Potassium (^{40}K) is commonly hosted in illite, micas, and K-feldspar, generally serving as a proxy for detrital input from continental crust. Thorium (^{232}Th) is found mainly in heavy minerals such as zircon, monazite, and xenotime; it is relatively immobile during weathering and diagenesis and is thus considered a stable indicator of detrital input. Uranium (^{238}U) is distinct from K and Th in that it is redox-sensitive and can be enriched in sediments under reducing conditions through adsorption onto organic matter or precipitation as uraninite. Variations in U content may therefore reflect not only changes in sediment source but also palaeoceanographic factors such as oxygenation and productivity, making it a less reliable proxy for purely orbital detrital flux signals.

During logging operations in both expeditions, IODP used the Hostile Environment Natural Gamma Ray Sonde (HNGS) to record natural gamma radiation along the borehole. This instrument is equipped with two bismuth germanate scintillation detectors and applies a five-window energy spectroscopy system, enabling separate estimates of potassium concentration (wt%), and thorium and uranium contents (ppm). Data interpretation is performed via least-squares fitting, decomposing the measured spectrum into the specific contributions of each radioactive element. The tool also filters out radiations below 500 keV, minimising interference from drilling fluid additives such as bentonite and potassium chloride (KCl). The results include the estimated K, Th, and U contents as well as integrated parameters: the total gamma radiation (HSGR) and the uranium-free gamma radiation (HCGR), both expressed in standardised API units (gAPI). Raw data are corrected based on caliper readings to ensure greater reliability of the profiles.

6.2 DATA BASE AND CROSS-CORRELATION

The data used in this study were obtained from the Lamont-Doherty Earth Observatory (LDEO) Log Database, which stores the logging data generated during IODP expeditions (https://mlp.ldeo.columbia.edu/logdb/scientific_ocean_drilling/result/files). Specifically, datasets were retrieved from IODP Expedition 369, Hole U1514C (Mentelle Basin, southeast Indian Ocean) and IODP Expedition 392, Hole U1579D (Agulhas Plateau, southwest Indian Ocean). The available downhole logs include continuous measurements of magnetic susceptibility and natural gamma radiation (NGR), acquired with wireline tools during drilling operations.

To investigate the degree of correlation between geochemical proxies and their cyclostratigraphic expression across different time series, a script was developed in R language to automatically perform cross-correlation analysis (Cross-Correlation Function, CCF). Previous examples of the use of the CCF in cyclostratigraphic studies can be found in Preto *et al.* (2004) and Mitchell *et al.* (2008). The CCF quantifies the similarity between two series as a function of their relative displacement: one series is progressively shifted relative to the other, and at each lag position the corresponding values are multiplied and summed, yielding a correlation coefficient (r) that reflects the degree of co-variation at that displacement (Davis, 1986; Telford *et al.,* 1990). Where the two series share strong structural similarity, the products tend to be predominantly positive, resulting in high r values; conversely, where the relationship is weak or absent, positive and negative products partially cancel, driving r toward zero (Davis, 1986).

The R routine implemented here displaces one series relative to the other in lag units corresponding to the sampling interval (0.1524 m), using lag.max = 100 and therefore testing displacements of up to ±15.24 m. The resulting coefficient varies between −1 and +1, with positive values indicating co-directional variation, negative values indicating an inverse relationship, and a lag of zero indicating optimal synchrony between the two series without any relative shift. The CCF is mathematically analogous to the Pearson correlation coefficient, extended to account for the dependence structure between lagged observations (Kulhánek, 2012; Davis, 1986).

6.3 CYCLOSTRATIGRAPHY

The cyclostratigraphic analysis was performed using the software Acycle (Li *et al.*, 2019a), while following the methodology described by Li *et al.* (2019). After selecting the proxies with the CCF function, the raw data were sectioned to the interval related to the investigation and interpolated to the value equivalent to the sampling rate (0.1524 m). The data then underwent trend removal using the High-Pass Butterworth filter with a cutoff frequency of 0.1 cycles/m for both holes, aiming to remove large-scale changes in the depositional system and million-year-scale modulations while preserving orbital signals of interest. Under linear detrending, spectral energy of the million-year-scale signals apparently overshadows the E405 band in the EHA, making orbital identification unreliable without prior high-pass filtering.

After this pre-processing stage, spectral analyses of the fast Fourier transform (FFT) type were performed using the multi-taper method (MTM; Mann and Lees, 1996) and evolutionary harmonic analysis (EHA) to define spectral bands for the possible orbital periods identified. These spectral analyses were supplemented by the application of F-tests, used to test for the presence of spectral peaks related to regular cyclic components with constant phase located within a frequency band (Thomson, 1990). The E405-kyr bands were then filtered using a Gaussian filter. Statistical analyses of the Correlation Coefficient (COCO) and Evolutionary Correlation Coefficient (eCOCO) were performed in parallel to verify the possible sediment accumulation rates (SAR) associated with the orbital cycles in effect for the period studied. The TimeOpt

method (Meyers, 2015, 2019) was additionally applied to provide independent SAR optimisation using both spectral power concentration and eccentricity amplitude modulation as simultaneous fit criteria.

Once both the top and base of the studied interval are constrained by biostratigraphy (top at ~56 Ma and base at ~66 Ma), an average age value of 61 Ma was estimated for the deposition interval. Using the astronomical solution of Laskar (2004) and additional known periodicities, the values of the Milankovitch cycles were calculated according to this estimated period, as detailed in Table 1 of the manuscript.

6.4 ASTRONOMICAL TIME SCALE

The Astronomical Time Scale (ATS) has come to represent one of the most robust approaches time-calibrating geological records, relying on the predictable variations in Earth's orbital parameters. The construction of the ATS requires astronomical solutions that numerically model the long-term evolution of Earth's orbital parameters. This study employs the La2004 solution (Laskar *et al.,* 2004), which extends back 250 Myr and provides a reliable framework for the Cenozoic interval. It is worth noting that, for the purposes of this study, the use of La2004 rather than more recent and, arguably, more precise solutions does not affect the duration estimates for the Palaeocene Epoch. The ZB18a solution (Zeebe and Lourens, 2019) is additionally referenced for constraints on the PETM age. A key aspect of these models is the representation of amplitude modulation of orbital parameters, particularly the long eccentricity cycle (~405 kyr), which provides a stable metronome for astronomical tuning deep into the past.

In this work, the ATS was constructed by anchoring cycle counting to the K-Pg boundary, assuming Sprain *et al.* (2019) dating of 66.052 Ma, and calibrating the time series using top and bottom biostratigraphic datum positions. This approach avoids the distortions inherent in full "floating" tuning (where internal cycle-by-cycle fitting to an astronomical target can introduce circular reasoning) and instead uses biostratigraphic constraints to check and correct the cycle-counting-derived age model.

6.5 SAR TESTING

Sediment Accumulation Rate (SAR) testing is a fundamental step in cyclostratigraphic analysis, providing the quantitative basis for evaluating the preservation of orbital signals in sedimentary sequences. Accurate determination of SAR is essential for distinguishing between primary climatic forcing and potential distortions introduced by depositional or diagenetic processes. In this study, SAR was evaluated through three complementary methods — COCO, eCOCO, and TimeOpt — applied to the High-Pass 0.1-filtered HTHO series of both holes, enabling cross-validation of the estimated accumulation rates and assessment of their lateral stability along the studied intervals.

6.5.1 COCO / eCOCO

The COCO method tests different sedimentation rates to search for a value that maximises the correlation between the data and theoretical astronomical models, using Pearson's coefficient for quantifying

correlation strength and the Monte Carlo method for statistical significance testing. COCO returns the SAR values with the highest Pearson correlation against the astronomical target. eCOCO (Evolutionary COCO) allows for temporal variation in SAR, expressing a more geologically realistic behaviour of sedimentation rates throughout the data. This method does not assume SAR to be constant when windowing the data and applying COCO to each window, yielding a possibly more appropriate adjustment of SAR to the prevailing astronomical cycles (see Li *et al.,* 2018a). For each hole, the H_0 rejection level ($p < 0.05$) defines the range of statistically supported SARs, while the rho maximum within that range identifies the optimal SAR estimate. The eCOCO analysis is used to assess the lateral stability of the supported SAR range along the stratigraphic section, providing information on possible depth-dependent variations in accumulation rate.

6.5.2 TimeOpt / eTimeOpt

To better gauge the uncertainties involved between Milankovitch cycle recognition and geological observations, Meyers (2015) proposed TimeOpt, a statistical optimization method that evaluates time scale uncertainty and identifies optimal models for climate and depositional systems response to astronomical forcing. The current study employs the TimeOpt solution available in the software Acycle. TimeOpt evaluates the time scale uncertainty by using the concept of "triangulation" for recognition of multiple attributes of the astronomical hypotheses that can be used to increase astrochronological testing. A probabilistic regression model framework evaluates both concentration of spectral power at predicted astronomical frequencies and modulation amplitude of astronomical periods. This methodology is detailed in Meyers (2015).

For time series that present secular variations in SAR, similarly to eCOCO, the Evolutionary Statistical Optimization Method (eTimeOpt) is proposed as a windowed analysis to sequentially evaluate the behaviour of shifted accumulation rates throughout the stratigraphic record.

6.5.3 A multi-method approach to evaluate SAR

Employment of this approach, however, is not advised for series that present larger variations in SAR; for such scenarios the Astrochron function "timeOptTemplate" is advised. The r^2_opt metric returned by TimeOpt quantifies the goodness-of-fit of each tested SAR against the astronomical target, with the peak r^2_opt value identifying the optimal accumulation rate. Where the TimeOpt peak and the COCO rho maximum differ, comparison between the two estimates provides information on whether any depth interval carries disproportionate spectral weight in the global optimisation. The combined multi-method SAR estimate, integrating the COCO-supported range and the TimeOpt r^2_opt peak, is used as the primary accumulation rate estimate for each hole, in which the recognition of SAR compatible with the E405 cycles will serve as a tiebreaker between COCO and TimeOpt. The frequency targets used for COCO are those from La04 model for 61Ma. The frequency targets used for TimeOpt are those presented in Table 1 fitted to the short eccentricity modulation.

6.6 WAVELET TRANSFORM ANALYSIS

Wavelet transform analysis provides a time-frequency representation of the signal, allowing the identification of changes in spectral content as a function of stratigraphic position (Torrence and Compo, 1998; Weedon, 2003). Unlike the fixed time-frequency resolution of the standard Fourier transform, wavelets use a variable window size that adapts to the frequency being analysed, providing good time resolution for high-frequency components and good frequency resolution for low-frequency components. Whereas MTM provides a single, globally averaged power spectrum for the entire depth series, wavelet analysis resolves how spectral power at each frequency (or period) evolves along the stratigraphic depth axis, making it particularly sensitive to non-stationary signals and gradual changes in sediment accumulation rate.

The continuous wavelet transform (CWT; Grossmann & Morlet, 1984) was computed using the Morlet mother wavelet ($\omega_0 = 6$), which provides an optimal balance between depth and frequency localisation for quasi-periodic geological signals (Torrence and Compo, 1998; Weedon, 2003). The angular frequency $\omega_0 = 6$ satisfies the admissibility condition and ensures adequate frequency resolution at the orbital periodicities relevant to this study. The CWT was computed using the Acycle software (Li *et al.,* 2019), with input series interpolated to a uniform sampling interval of 0.1524 m prior to transformation. The 95% significance level against a red-noise background was estimated following Torrence and Compo (1998), using an AR(1) coefficient derived from each input series. Results are presented as period-domain and frequency-domain wavelet power spectra, with the cone of influence (COI), within which edge effects reduce interpretability, indicated in each panel.

In this study, extended wavelet analyses were performed on both the High-Pass 0.1-filtered and raw HTHO series for both wells, enabling the tracking of E405 cycle thickness variation through the studied interval and the identification of intervals of signal degradation or cycle amalgamation. The comparison between filtered and raw wavelet spectra also provides a direct visual assessment of the contribution of long-period myr-scale energy to the total spectral variance, corroborating the choice of the High-Pass 0.1 pre-filtering step.

Two main limitations of the wavelet approach merit consideration. First, the cone of influence (COI) reduces the interpretable depth range near the top and bottom of each series by a distance approximately equal to one half-wavelength of the period of interest; for E405-scale signals (~6–8 m period), this corresponds to an edge-affected zone of ~3–4 m at each end, which is negligible relative to the total series length. Second, the wavelet power at any given depth position represents a spectral average over a window of approximately one wavelength, so features shorter than one E405 cycle (~6–8 m) cannot be resolved as depth-specific events. The INPEFA method (Section 6.7), which operates in depth space without spectral averaging, is therefore better suited to identifying abrupt depositional events.

6.7 INTEGRATED PREDICTION ERROR FILTERING ANALYSIS (INPEFA)

The Integrated Prediction Error Filter Analysis (INPEFA) is a geophysical technique widely used as an auxiliary method for stratigraphic correlation between wells, highlighting depositional trends within a stratigraphic framework (Zulivandama, 2018; Nainggolan, 2019; Liu *et al.,* 2024). The INPEFA curve is derived from the integration of the Prediction Error Filter Analysis (PEFA) curve, which is obtained through an autoregressive (AR) model that compares observed values with values predicted from previous samples of the series. Significant deviations between predicted and observed values represent statistically unpredictable events, which may be interpreted as depositional discontinuities, often associated with stratigraphic hiatuses, sequence boundaries, or related stratigraphic surfaces.

Within the framework of sequence stratigraphy, the cumulative prediction error analysis (INPEFA) applied to logging data generates a curve that highlights depositional trends along the stratigraphic profile. Upward trends in the curve, commonly associated with high NGR values and positive prediction errors, indicate transgressive phases. Conversely, downward trends, typically related to lower NGR values, correspond to regressive phases (Nio *et al.,* 2005; De Jong, 2007; Liu *et al.,* 2024). Transitions between these trends are represented by inflection points in the INPEFA curve, which mark significant changes in depositional patterns. In this work, the INPEFA results selected for comparison correspond to curves generated using 35% LOWESS locally weighted scatterplot smoothing.

7 MANUSCRIPT: CYCLOSTRATIGRAPHY OF AGULHAS PLATEAU AND MENTELLE BASIN RECORDS (IODP EXPEDITIONS 392 AND 369): AN ORBITALLY-BASED CHRONOSTRATIGRAPHY FROM THE K–PG BOUNDARY TO THE PETM

The results of this dissertation are presented in the form of a scientific article submitted for publication. The study investigates the Paleocene cyclostratigraphy and astrochronology of two deep-marine IODP records from the Southern Hemisphere, the Agulhas Plateau (Expedition 392, Hole U1579D) and the Mentelle Basin (Expedition 369, Hole U1514C), through cyclostratigraphic analyses of downhole spectral gamma-ray thorium logs. The research focuses on identifying orbital cycles, estimating sediment accumulation rates and constructing astronomical time scales anchored to the K–Pg boundary. The resulting chronologies identify approximately 25-25.5 long-eccentricity cycles between the K–Pg boundary and the PETM onset, constraining the event to ~55.7-55.9 Ma. A positive thorium anomaly at ~58.15 Ma is interpreted as corresponding to a unnamed "*" carbon isotope excursion. INPEFA trends further suggest depositional changes broadly consistent with Paleocene sea-level variations. These results expand the Southern Hemisphere coverage of Paleocene astronomical time scales and refine the chronostratigraphic framework of the Paleocene Indian Ocean sector.

CYCLOSTRATIGRAPHY OF AGULHAS PLATEAU AND MENTELLE BASIN RECORDS (IODP EXPEDITIONS 392 AND 369): AN ORBITALLY-BASED CHRONOSTRATIGRAPHY FROM THE K–PG BOUNDARY TO THE PETM

Bernardo Mokan Maffessoni[1,*], Mariane Candido[1], João Maurício Figueiredo Ramos[2], Daniel Ribeiro Franco[1], Mateus Fontana Michelon[2], Raysa de Magalhães Rocha[1]

[1]*Coordenação de Geofísica, Observatório Nacional, Rio de Janeiro, Brazil.*

[2]*Petrobras, Rio de Janeiro, Brazil.*

* Corresponding author.

E-mail address: bmmaffessoni@on.br

ABSTRACT

The Paleocene Epoch (~66-56 Ma) represents a critical yet under-constrained interval in Earth's climate history, bracketed by the Cretaceous-Paleogene (K-Pg) mass extinction and the Paleocene-Eocene Thermal Maximum (PETM). Although the geological record of this interval is well-preserved in marine sedimentary

archives, the astronomical calibration of Paleocene successions remains incomplete - and the absolute age of the PETM onset in particular remains debated. Southern Hemisphere records are especially underrepresented in existing cyclostratigraphic frameworks, limiting the global integration of Paleocene timescales. Here, we present high-resolution cyclostratigraphic analyses of thorium wireline logs from two deep-marine Paleocene sequences recovered by IODP expeditions: Expedition 392 - Hole U1579D, Agulhas Plateau (South Indian Ocean) – and Expedition 369 - Hole U1514C, Mentelle Basin (Western Australia). Both astronomical timescales anchored to the K-Pg boundary identify approximately 25-25.5 long-eccentricity cycles to the PETM, constraining its onset to ~55.7-55.9 Ma. Sediment accumulation rates of ~1.1-2.1 cm/kyr at U1579D and ~1.0-1.8 cm/kyr at U1514C are supported by COCO/eCOCO statistical tests. A prominent positive thorium anomaly is constrained to ~58.15 Ma once is consistent with an unnamed carbon isotope excursion ("*" CIE) marking the termination of the Paleocene Oxygen Isotope Maximum. Integrated Prediction Error Filter Analysis curves evidenced trend reversals consistent with changes in the depositional regime, broadly consistent with the Paleocene eustatic sea-level variations. These results expand the geographic coverage of Paleocene astronomical timescales into the Southern Hemisphere and offer new chronostratigraphic constraints on key Paleocene climate events.

Keywords: Paleocene astrochronology; Cyclostratigraphic analysis; K-Pg-PETM interval; Th channel

1 INTRODUCTION

Throughout Earth's history, extreme events have repeatedly disrupted the stability of the Earth system, reshaping environmental conditions and influencing the evolution of life. These perturbations, operating across a range of temporal and spatial scales, have significantly altered ocean circulation patterns and global ecosystems. Mass extinctions represent the most extreme disruptions of the biosphere, opening ecological spaces for new organisms across the last ~540 Myr (Barnosky *et al*., 2011; Burgess, 2019), and the K-Pg boundary and PETM stand out as primary, globally recognised time markers offering unparalleled opportunities for high-resolution chronostratigraphic analysis.

The Paleocene Epoch (~66-56 Ma; Gradstein *et al*., 2020) remains one of the least astronomically constrained intervals of the Cenozoic, spanning from the K-Pg boundary to the PETM. The K-Pg boundary is associated with the abrupt extinction of approximately 75% of Earth's species, primarily linked to a large extraterrestrial impact and its cascading climatic and ecological consequences (Alvarez *et al*., 1980; Schulte *et al*., 2010). The PETM, in turn, is characterised by a rapid global temperature increase of ~5-8°C over a few thousand years, accompanied by ocean acidification, major disruptions to the carbon cycle, and large-scale biotic migrations (Zachos *et al*., 2005; 2008; McInerney and Wing, 2011).

A key unresolved debate (e.g., Westerhold *et al*., 2008; 2012; Hilgen *et al*., 2010; 2015; Dinarès-Turell *et al*., 2014; Zeebe and Lourens, 2019; 2022) concerns whether 24 (9720 kyr) or 25 (10125 kyr) complete E405 cycles separate the K-Pg boundary from the PETM – a question with direct implications for the absolute

age of the PETM and its causal relationship with the North Atlantic Igneous Province (NAIP) volcanic record (Westerhold *et al*., 2008; Hilgen *et al*., 2010; Dinarès-Turell *et al*., 2014). Beyond this cycle-count problem, the precise timing and duration of short-lived hyperthermal and carbon-cycle perturbation events within the Paleocene remain poorly resolved in many regions. This limitation is especially pronounced in the Southern Hemisphere, where existing cyclostratigraphic frameworks are underrepresented, hampering the global integration of Paleocene timescales.

To address these challenges, this study applies cyclostratigraphic analyses to HTHO wireline log data from two deep-marine Paleocene sequences recovered by IODP expeditions: Hole U1579D, drilled on the Agulhas Plateau (South Indian Ocean; Expedition 392), and Hole U1514C, drilled on the Mentelle Basin (western Australian margin; Expedition 369). Thorium is a lithophile, diagenetically immobile element concentrated in detrital heavy minerals that faithfully records orbital-scale detrital flux variations in pelagic carbonate sequences and has been shown to outperform total natural gamma ray and uranium as a cyclostratigraphic proxy in such settings (Adams and Weaver, 1958; Schnyder *et al*., 2006). The Agulhas Plateau provides an ideal setting for this analysis: its Paleocene succession is characterised by a nearly continuous, homogeneous nannofossil chalk with low detrital input and minimal evidence of reworking, offering a low-noise substrate for orbital signal preservation. The Mentelle Basin hole provides a complementary record from the eastern Indian Ocean margin, enabling assessment of inter-site consistency in orbital signal detection and sediment accumulation rates across two geographically distinct Southern Hemisphere localities.

By establishing orbitally calibrated timescales anchored to the K-Pg boundary across two under-studied Southern Hemisphere sites, this work directly addresses the long-standing 24-versus-25-cycle debate and provides new temporal constraints on the absolute age of the PETM. Furthermore, the co-temporal nature of anomalous HTHO peaks at both holes enables identification and discussion of the carbon isotope excursion "*" at ~58.15 Ma (Littler *et al*., 2014; Barnet *et al*., 2019; Hollis *et al*., 2022), linking it to the termination of the POIM and expanding our understanding of Paleocene carbon-cycle dynamics beyond the North Atlantic and Pacific domains. At a time when the astronomical timescale of the Paleocene is being actively revised, new orbital records from the Southern Hemisphere are not merely complementary, they are essential for testing current astrochronological models in a global scope.

2 GEOLOGICAL SETTING

2.1 IODP EXPEDITION 392 - HOLE U1579D, AGULHAS PLATEAU

IODP Expedition 392, conducted between February and April 2022, targeted the southwest Indian Ocean to investigate the long-term climate transition from the Cretaceous greenhouse to the late Paleogene icehouse (Uenzelmann-Neben *et al*., 2023). The Agulhas Plateau was positioned at paleolatitudes of 53°-61° S during the late Cretaceous (van Hinsbergen *et al*., 2015). The studied interval at Hole U1579D (~74% core recovery; Fig. 1A-D) is entirely assigned to Lithostratigraphic Subunit IIb (149.40-556.31 m CSF-A), a ~407

m thick sequence of white to light greenish-gray nannofossil chalk ($CaCO_3$ values generally 65-95 wt%) which provides a lithologically homogeneous and diagenetically stable substrate well-suited for cyclostratigraphic analysis (Bohaty *et al*., 2023). The dominant lithology is calcareous nannofossil chalk with faint decimeter- to meter-scale alternations in clay content; bioturbation is common throughout the U1579D stratigraphy.

The K-Pg boundary was inferred at 433.25 m CSF-A in Section 33R-6, 98.5 cm, marked by a sharp colour change from reddish-brown clayey calcareous chalk to grayish-green calcareous chalk with clay, and confirmed core catchers by calcareous nannofossil and foraminiferal datums (Bohaty *et al*., 2023). The Paleocene-Eocene boundary and base of the PETM are absent from the recovered sequence: the Paleocene-Eocene boundary falls within the unrecovered core gap between Cores 16R and 17R (~267-271 m CSF-A), as evidenced by the presence of PETM markers (*Rhomboaster bramlettei* and *Campylosphaera eodela*) in Sample 16R-CC at 267.14 m CSF-A and their absence in Sample 17R-1 at 271.5 m CSF-A. The Paleocene succession records a remarkably consistent average SAR of ~1.7 cm/kyr, constrained by 13 calcareous nannofossil biohorizons and 6 palaeomagnetic reversals (Chrons C26r through C29r), with inter-calibration between bio- and magnetostratigraphy (Bohaty *et al*., 2023). Unlike Hole U1514C, only minor reworking is reported within the Paleocene section at U1579D, consistent with the uninterrupted carbonate chalk facies, low detrital input, and the greater lithological homogeneity of the Agulhas Plateau succession.

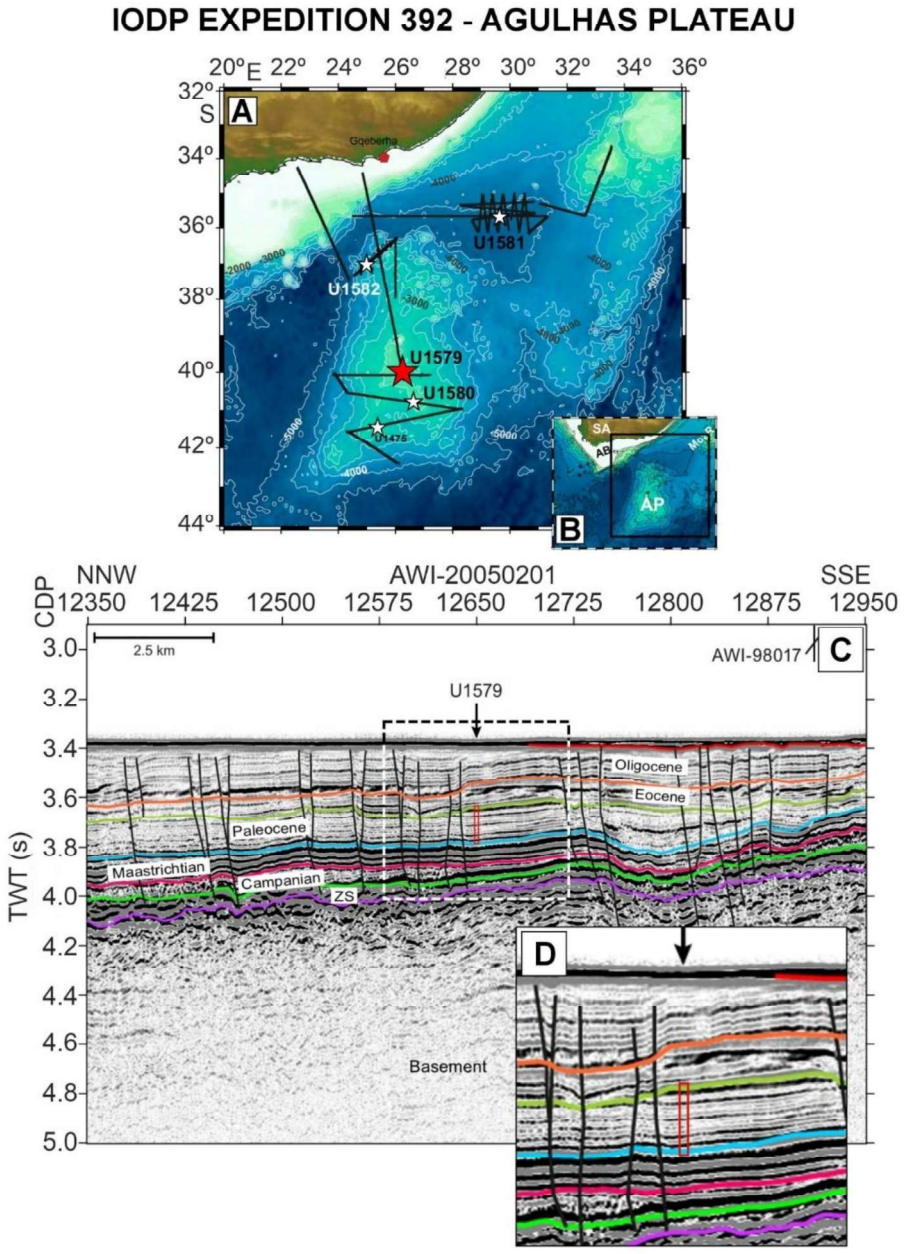


Figure 1 – Regional map and seismic profiles showing the location of Hole U1579D at the Agulhas Plateau (IODP Expedition 392). (A-B) Bathymetric map with expedition drill sites indicated; U1579 marked by red star. GPS coordinates: U1579D at 41°24.92'S, 25°30.46'E. (C-D) Seismic profile AWI-20050201 showing Paleocene stratigraphy with Site U1579 indicated. Map lines delineate study areas and do not necessarily depict accepted national boundaries (Modified from Uenzelmann-Neben *et al*., 2023).

2.2 IODP EXPEDITION 369 - HOLE U1514C, MENTELLE BASIN

IODP Expedition 369 (September - November 2017; Huber *et al*., 2019) targeted the western Australian margin to investigate the Cretaceous and Cenozoic tectonic and palaeoceanographic evolution of the Mentelle Basin (MB), adjacent to the Naturaliste Plateau. The MB formed along the western Australian margin during the detachment from the Indian subcontinent (Bradshaw, 2003), and the Naturaliste plateau (~60° S paleolatitude during the early Cretaceous) is interpreted as a volcanic margin coeval with the onshore Bunbury Basalt (137-130 Ma; Direen *et al*., 2017).

Site U1514 (Fig. 2A-D) recovered an expanded Pleistocene-Eocene sequence penetrating into upper Albian strata. At Hole U1514C, the studied interval corresponds predominantly to lithological Unit II, comprising clayey nannofossil chalk and nannofossil chalk. The K-Pg boundary is identified at ~393.5 m CSF-A, marked by a dark greenish-gray claystone package (Cores 22R-23R). The PETM interval is located near ~280 m CSF-A based on natural gamma-ray uranium enrichment, colour changes, and diagnostic core catchers nannofossil assemblages (Huber *et al*., 2019).

The sedimentary record exhibits a nearly continuous SAR of ~1.4 cm/kyr from the late Maastrichtian through the early Oligocene (Huber *et al*., 2019). Core recovery in Hole U1514C is approximately 65%, and significant reworking is documented in the lower Eocene section (Cores 9R-11R): sample 10R-CC contains reworked middle Paleocene nannofossil taxa (*Heliolithus kleinpellii*, *Fasciculithus tympaniformis*) within an early Eocene CP9a assemblage, indicating mixing of Paleocene material into the lowermost Eocene. A uranium enrichment spike recorded at 279 m CSF-A in the gamma-ray well-log was associated with the Paleocene-Eocene boundary by the expedition science team (Huber *et al*., 2019). Poor core recovery in several Paleocene cores (Cores 18R, 25R) further limits stratigraphic resolution. Magnetic polarity zones were tentatively correlated with Chrons C23n.1n through C34n, with biostratigraphy and micropaleontology serving as the primary age constraints.

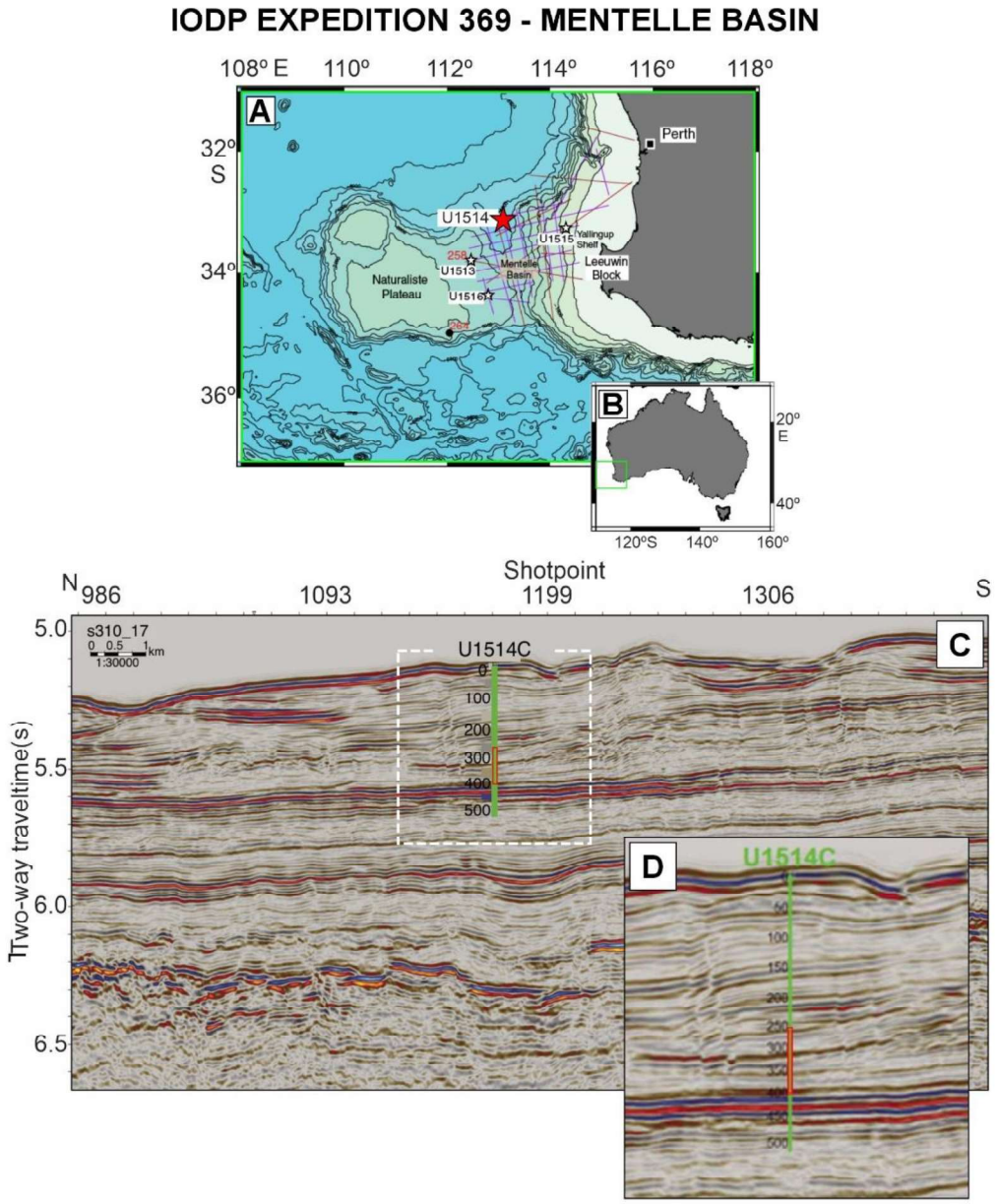


Figure 2 – Regional map and seismic profiles showing the location of Site U1514 at the Mentelle Basin (IODP Expedition 369). (A-B) Bathymetric map with expedition drill sites indicated; U1514 indicated by red star. GPS coordinates: U1514C at 33°46.96'S, 112°22.37'E. (C-D) Uninterpreted two-way traveltime seismic profile showing the Paleocene stratigraphy, the location of Hole U1514C, and the approximate position of the studied interval. Map lines delineate study areas and do not necessarily depict accepted national boundaries (Modified from Huber *et al.*, 2019).

3 METHODS

3.1 WIRELINE LOG DATA

Publicly available IODP data were obtained from the Lamont-Doherty Earth Observatory (LDEO) Log Database (available at https://mlp.ldeo.columbia.edu/logdb/scientific_ocean_drilling/result/files/) for Holes U1579D (Expedition 392) and U1514C (Expedition 369) (Fig. S1; Supplementary Material). Both expeditions employed the Hostile Environment Natural Gamma Ray Sonde (HNGS), that enables separate estimates of ^{40}K (HFK, wt%), ^{232}Th (HTHO, ppm), and ^{238}U (HURA, ppm), with the total spectral gamma

radiation (HSGR, gAPI) as the integrated parameter. The HNGS applies a five-window energy spectroscopy system and spectral deconvolution to separate elemental contributions (De Vleeschouwer *et al*., 2017; Huber *et al*., 2019; Bohaty *et al*., 2023). The wireline depth scale (WMSF) was used throughout. For Hole U1579D, the offset between CSF-A and WMSF is approximately -1.8 m. The sampling rate for the data used from both boreholes is 15.24 cm.

3.2 PROXY SELECTION

The analysed stratigraphic intervals were defined by two stratigraphic tie points, according to the established by the shipboard scientific teams of Expeditions IODP 392 and 369 for Holes U1579D and U1514C (Uenzelmann-Neben *et al.,* 2023; Huber *et al.,* 2019), respectively: (i) the K-Pg boundary; and (ii) the estimated position of the PETM – hence yielding the following stratigraphic intervals: ~255–440 m WMSF at U1579D and ~265–410 m WMSF at U1514C. The suitability of HTHO as the primary proxy was assessed through cross-correlation function (CCF) analysis of all pairwise combinations of the four NGR spectral components (HSGR, HFK, HTHO, HURA; see Fig. S1 and S2 in the Supplementary Material). CCF analysis demonstrates a clear zero-lag correlation of HTHO with both HSGR ($|r| = 0.78$ for U1579D, and $|r| = 0.92$ for U1514C) and HFK ($|r| = 0.54$ for U1579D, and $|r| = 0.92$ for U1514C), reflecting the geochemical immobility of thorium in terrigenous clay minerals under normal seawater and diagenetic conditions. HURA exhibits a systematic positive phase lag of 2.44 m for U1579D and 3.96 m for U1514C relative to HTHO, indicating possible post-depositional uranium remobilisation under variable redox conditions and disqualifying it as a cyclostratigraphic proxy (Fig. S2). HTHO was therefore selected as the primary proxy for all cyclostratigraphic analyses. The robustness of this selection was further supported by comparison of the filtered HTHO series with the HTHO/HFK ratio (Fig. 3A and 4A), which demonstrates broad coherence of orbital-scale cyclicity across independent geochemical channels at both holes, supporting the reliability of thorium as a cyclostratigraphic proxy independently of potassium co-variation. This comparison and full details of the CCF methodology and results are provided in the Text S1 (Supplementary Material).

3.3 CYCLOSTRATIGRAPHY

Time series analysis was performed using the open-source software Acycle version 2.8 (Li *et al*., 2019a). Raw HTHO data were trimmed to include the K-Pg–PETM interval, resampled at a uniform spacing of 0.152 m using linear interpolation prior to detrending by applying a high-pass butterworth filter with a cutoff of 0.1 cycles/m (for more information on the detrending tests, see Texts S3 and S4 at the Supplementary Material).

Spectral analyses were conducted using the multi-taper spectral estimator (MTM; Thomson, 1982; Mann and Lees, 1996) with two 2π tapers to identify significant frequencies above the 90% confidence levels relative to a robust first-order autoregressive red-noise background model. Evolutive harmonic analysis (EHA) performed using a sliding-window Fast Fourier method (eFFT) was used to track variations in the expression

of orbital frequencies throughout stratigraphic succession. Continuous wavelet transform was applied in order to provide an independent evaluation of the dominant periodicities identified by MTM and EHA. Expected orbital spectral peak ratios were calculated assuming a mean sedimentary age of ~61 Ma based on the La2004 astronomical solution (Laskar *et al*., 2004), yielding the following period ratios for the dominant Milankovitch cycles: 405:125:95:39:23:18.7 = 21.6:6.7:5.1:2.1:1.2:1 (Table 1). Definition of orbital frequency bands was conducted by considering the spectral peak ratios and the MTM/EHA analyses.

The optimal SAR and the null hypothesis of no orbital forcing (H_0) were evaluated using the correlation coefficient (COCO) and evolutionary correlation coefficient (eCOCO) methods (Li *et al*., 2018). Both analyses were run with 5000 Monte Carlo simulations, with SAR ranging from 0.5 to 5 cm/kyr. The TimeOpt method (Meyers, 2015) – which provides SAR estimates by fitting the stratigraphic power spectrum to predicted orbital periodicities – was applied to provide an independent estimate of the optimal SAR. For more detail, see Supplementary Material.

3.4 ASTRONOMICAL TIME SCALE

Astronomical time scales (ATS) were constructed by anchoring the Gaussian-filtered E405 signal to the K-Pg boundary at 66.052 ± 0.008/0.043 Ma (Sprain *et al*., 2019) and counting successive E405 cycles upward toward the PETM. The La2004 astronomical solution (Laskar *et al*., 2004) provides a stable and well-validated eccentricity model widely adopted as the reference framework for Paleocene astrochronology (Westerhold *et al*., 2008; 2020; Barnet *et al*., 2019). Anchoring to the K-Pg boundary, rather than employing a fully floating tuning approach, avoids the circular reasoning inherent in cycle-by-cycle fitting to an astronomical target, in which internal tuning distortions can accumulate undetected; instead, it provides an independent, radiometrically-constrained reference point that fixes the base of the E405 cycle count and allows deviations from the astronomical model to serve as genuine diagnostic information (Dinarès-Turell *et al*., 2014; Clyde *et al*., 2016; Sprain *et al*., 2019).

In our work, both ATS were constructed taking into account the top/bottom biostratigraphic datum positions - the base (B, first occurrence) and top (T, last occurrence) of calcareous nannofossil taxa extracted by core catchers from the expedition proceedings for each hole – following the Paleocene nannofossil zonation of Martini (1971) and the integrated bio-magnetochronology of Agnini *et al*. (2014), with foraminiferal datums following Wade *et al*. (2011). Datums exhibiting poor stratigraphic reliability or low biochronological diagnostic value, and those inconsistent with the cyclostratigraphic framework based on implausible cycle spacings, were excluded from the final tuning (Table 2).

3.5 INTEGRATED PREDICTION ERROR FILTER ANALYSIS (INPEFA)

INPEFA is a geophysical method which has been increasingly applied in well-log analysis for the identification of depositional trends and stratigraphic correlation within a sequence-stratigraphic framework (e.g., Nio *et al*., 2005; De Jong *et al*., 2007). In this study, INPEFA was applied to the raw HTHO series of

both holes prior to high-pass filtering. To reduce sensitivity to high-frequency noise while preserving third-order depositional trends, the HTHO series was pre-processed using locally weighted scatterplot smoothing (LOWESS; Cleveland, 1981) at a smoothing window of 35% prior to PEFA computation. The resulting INPEFA curves are presented alongside the primary cyclostratigraphic panels (Figs. 3B and 4B) to assist in the identification of depositional regime changes. Full details of the INPEFA procedure are provided in Text S2 (Supplementary Material).

4 RESULTS

4.1 SPECTRAL ANALYSIS AND ORBITAL FREQUENCY IDENTIFICATION

MTM spectral analysis of the high-pass 0.1-detrended HTHO logs identifies a dominant peak in ~5-7 m at both holes, corresponding to the 405-kyr long-eccentricity cycle (E405), with band limits of 4.55-8.40 m at U1579D and 4.24-7.19 m at U1514C, both exceeding the 99% confidence level (Figs. 3F and 4F; Table 1). Short eccentricity cycles are indicated by spectral power above the AR(1) noise background in both the MTM spectra and EHA, with band limits of 1.07-2.72 m at U1579D and 0.99-2.33 m at U1514C; however, their expression are not continuously resolved across the full depth interval. The obliquity signal is estimated for U1579D at ~0.7 m (Fig. 3F-G, deep purple slab), and is absent for U1514C (Fig. 4F-G). It was not possible to identify the precession imprint since the frequencies are probably below the Nyquist frequency: the depth-domain precession frequencies are expected between 1/48 - 1/21 cm^{-1} and 1/41 - 1/20 cm^{-1} (U1579D and U1514C, respectively) – hence falling at, or below, the effective Nyquist limit regarding the ~15.24 cm logging resolution (f_{nyq} ~ 1/30.48 cm^{-1}).

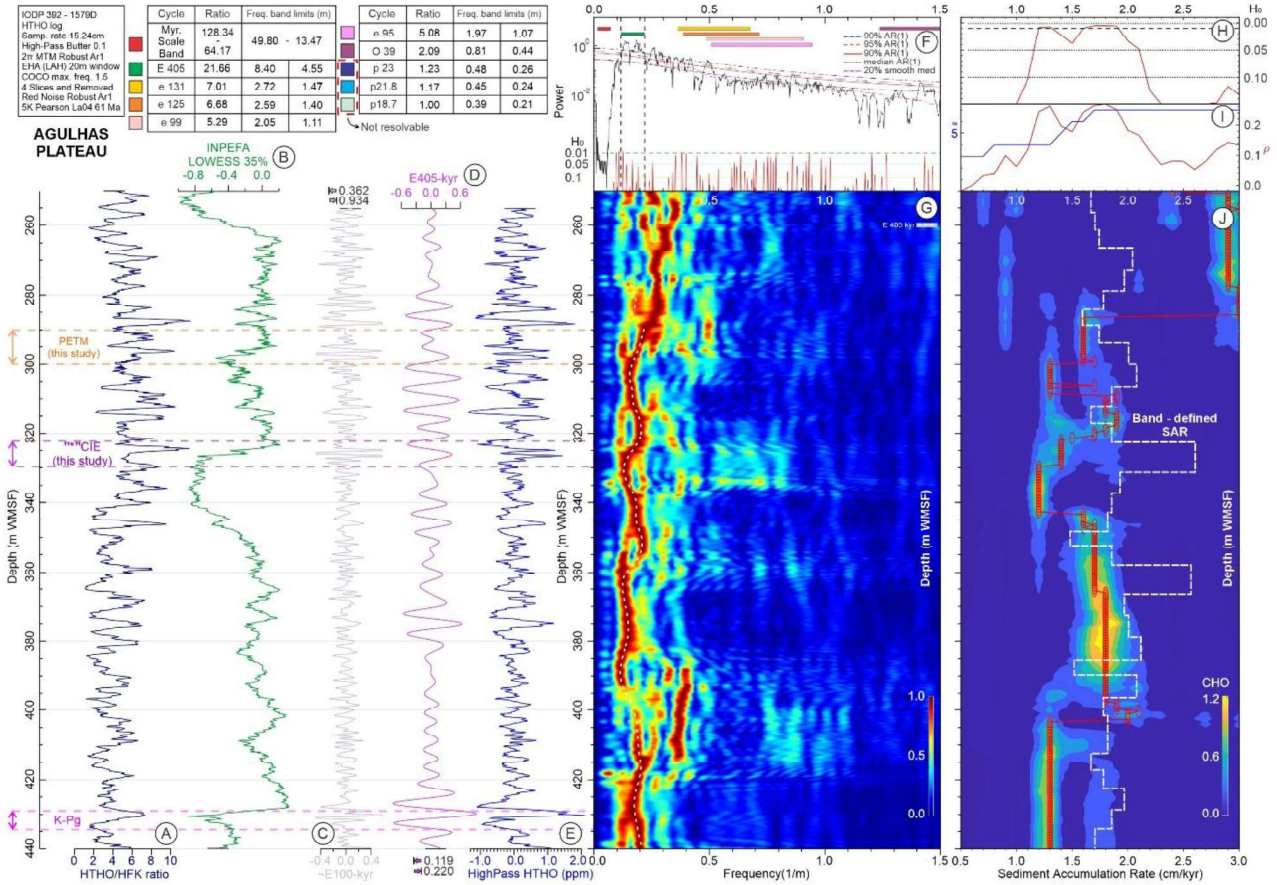


Figure 3 – Primary cyclostratigraphic analysis for Agulhas Plateau Hole U1579D (High-Pass 0.1). (A) HTHO/HFK ratio; (B) INPEFA with LOWESS 35%; (C) Gaussian-filtered ~E100-kyr signal; (D) Gaussian-filtered E405-kyr signal; (E) High-Pass detrended HTHO; (F) MTM spectral analysis with confidence levels and F-test results; (G) EHA with dashed white E405 reference (central wavelength ratio ~6.67 m); (H) COCO null hypothesis; (I) COCO ρ and number of contributing orbital parameters; (J) eCOCO with band-defined SAR obtained by constructing the age model based on the output of the E405 Gaussian filter.

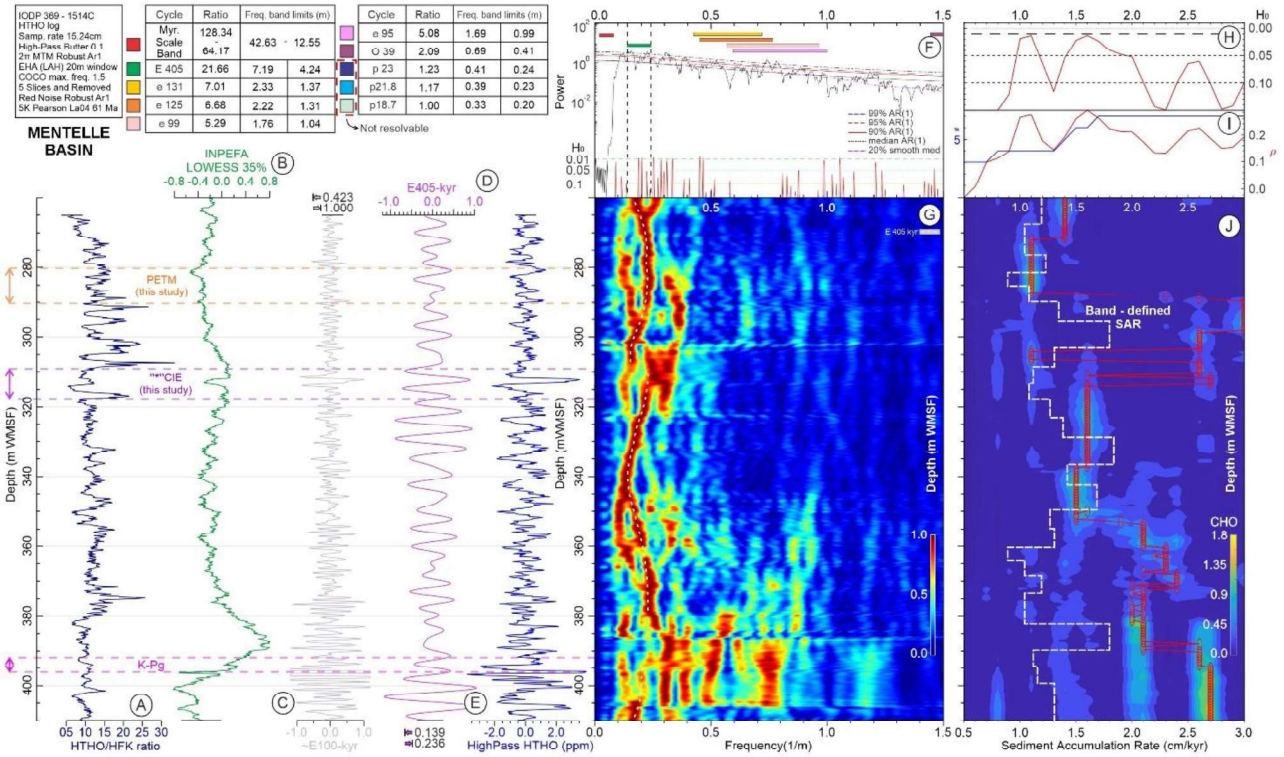


Figure 4 – Primary cyclostratigraphic analysis for Mentelle Basin Hole U1514C (High-Pass 0.1). Panels as in Fig. 3. Note the greater variability in the HTHO/HFK ratio (panel A) relative to Fig. 3A, consistent with the more lithologically heterogeneous Clayey Nannofossil Chalk facies at the Mentelle Basin.

EHA suggests persistence of the E405 signal across both records (Figs. 3G and 4G). At U1579D, a continuous frequency band centered at ~6-7 m tracks consistently from ~260 to ~430 m WMSF. An observed intermittent frequency at 0.362-0.934 cycles/m (Fig. 3C) and 0.423-1.000 cycles/m (Fig. 4C), interpreted as the expression of the short-eccentricity signal, is also present through parts of the section. At U1514C, the E405 band is persistent but exhibits slightly greater lateral variation, consistent with modest changes in sediment accumulation rate across the section. Extended wavelet analysis of the high-pass 0.1-filtered HTHO record independently confirms the dominance of E405 signal in the power spectra, with relatively uniform E405 wavelength of ~4-7 m throughout most of the section (Figs. S9 and S10; Supplementary Material).

Table 1. Orbital periodicities predicted by the La2004 astronomical solution (Laskar *et al.*, 2004) for a mean age of 61 Ma, with corresponding expected wavelengths at the primary sediment accumulation rate estimates for each hole. Observed band limits (from MTM and EHA analyses) are given in the rightmost columns. E = long eccentricity; e = short eccentricity; O = obliquity; P = precession; M = million-year-scale band. n.r. = not resolved above 95% confidence threshold.

Cycle	Period (kyr)	Spectral ratio *	Expected wavelength at 1.5 cm/kyr (m)	Expected wavelength at 1.3 cm/kyr (m)	Observed band U1579D (m)	Observed band U1514C (m)
E405	405	21.66	6.08	5.27	8.40-4.55	7.19-4.24
e131	131	7.01	2.00	1.73	2.72-1.47	2.33-1.37
e125	125	6.68	1.88	1.63	2.59-1.40	2.22-1.31
e99	99	5.29	1.49	1.29	2.05-1.11	1.76-1.04
e95	95	5.08	1.43	1.24	1.97-1.07	1.69-0.99

O39	39	2.09	0.59	0.51	~0.71 (tentative)	n.r.
P23	23	1.23	0.35	0.30	n.r.	n.r.
P21.8	21.8	1.17	0.33	0.28	n.r.	n.r.
P18.7	18.7	1.00	0.28	0.24	n.r.	n.r.
Myr-Scale Band	2400 - 1200	64.17 - ~128.34	36.00 - 18.00	31.20 - 15.60	50 - 13 m (raw)	43 - 13 m (raw)

* Spectral ratio calculated with respect to the 18.7 kyr-precession signal.

4.2 CYCLOSTRATIGRAPHIC CONSTRAINTS ON SEDIMENT ACCUMULATION RATES

The COCO results for U1579D stratigraphy indicates H_0 rejection at $p < 0.05$ for SARs ranging between approximately 1.1 and 1.9 cm/kyr (Fig. 3H–J; Supplementary Text S5, Fig. S7). eCOCO analysis yields a consistent pattern, with statistically significant correlation coefficients clustering within the same SAR range throughout most of the section. TimeOpt (Text S5; Supplementary Material) broadly corroborates these estimates, although r^2_opt reaches its global maximum at ~2.12 cm/kyr – a value falling outside the COCO supported range – a secondary peak at ~1.7 cm/kyr lies within the COCO interval and is therefore considered the more reliable estimate, given its consistency across methods. The combined multi-method SAR estimate for U1579D is ~1.1–2.1 cm/kyr, with an optimal fit SAR of ~1.5–1.9 cm/kyr.

At U1514C, null hypothesis is rejected at $p < 0.05$ for SARs between ~1.0 and 1.8 cm/kyr (Fig. 4H–J; Supplementary Text S5, Fig. S8). eCOCO results are consistent with this range across most of the stratigraphic succession. TimeOpt peaks at ~1.62 cm/kyr (Text S5; Supplementary Material), falling within the COCO-supported interval and reinforcing the multi-method estimate. The combined SAR estimate for U1514C is ~1.0–1.8 cm/kyr, with a SAR given by the optimal fit of ~1.62 cm/kyr.

Taken together, the SAR estimates at both holes are broadly consistent, ranging between ~1.0 and 2.1 cm/kyr, and are in good agreement with the shipboard SAR of ~1.4 cm/kyr reported for U1514C and ~1.7 cm/kyr for U1579D (Huber *et al.*, 2019; Bohaty *et al.*, 2023), providing independent cyclostratigraphic validation of the expedition-derived accumulation rates.

4.3 INPEFA

At Hole U1579D, the INPEFA curve undergoes a sharp inflection toward positive values at the K–Pg boundary (~430 m WMSF), followed by a gradual decreasing trend that reaches a minimum at ~330 m WMSF. An abrupt shift at ~325 m WMSF marks the transition to a plateau-like interval that persists upward to ~260 m WMSF. Within this interval, a secondary abrupt positive inflection occurs at ~300 m WMSF (Fig. 3B).

At Hole U1514C, the INPEFA curve exhibits a decreasing trend from the K–Pg boundary at ~395 m WMSF to ~340 m WMSF, after which the trend reverses into a gentle upward trajectory, culminating in an abrupt positive inflection at ~313 m WMSF (Fig. 4B). Above this inflection, the curve resumes a decreasing trend toward ~280 m WMSF, where a secondary positive inflection marks a renewed reversal toward the top of the studied interval.

4.4 ASTRONOMICAL TIME SCALE

4.4.1 Hole U1579D

Anchoring to the K-Pg boundary at ~431 m WMSF (T *Cretaceous nannoflora*, 66.04 Ma; Agnini *et al*., 2014; Uenzelmann-Neben *et al*., 2023), approximately 25.5 E405 cycles are identified between the K-Pg boundary and the PETM interval, with the full studied section yielding 31 cycles to ~265 m WMSF (~12.55 Myr; Fig. 5). Nine calcareous nannofossil biostratigraphic datums were incorporated into the ATS calibration (Table 2); eight datums from the Expedition 392 proceedings were excluded on the basis of low diagnostic value, taxonomic uncertainty, or internal inconsistency with the cyclostratigraphic framework.

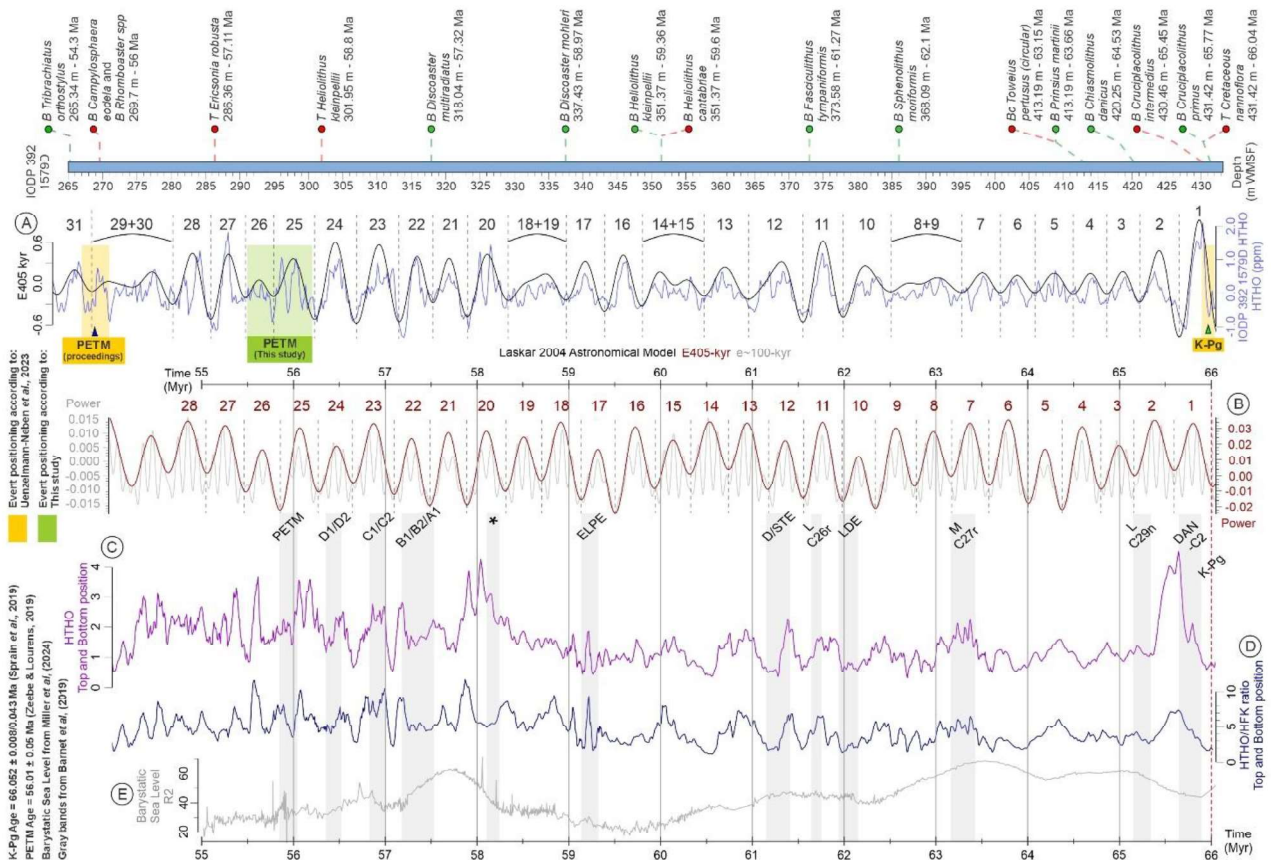


Figure 5 – Astronomical time scale for Hole U1579D based on the La2004 solution. (A) Detrended HTHO (blue) with Gaussian E405 filter (black) and E405 cycle numbering from the K-Pg boundary (the E405 kyr cycle boundary positions, in m along the core, are provided in Table S1); the PETM is provisionally placed at ~cycle 25.5 based on HTHO and HTHO/HFK peaks coinciding with the Barnet *et al.* (2019) PETM band; the prominent anomaly at ~325 m WMSF (asterisk "*" symbol) is constrained to ~58.15 Ma. (B) La2004 astronomical model (E405 red; e~100 grey). (C) HTHO tuned using top/bottom biostratigraphic datum positions; green markers indicate datums used; red markers indicate datums excluded due to internal cyclostratigraphic inconsistencies. (D) HTHO/HFK ratio tuned using top/bottom positions. (E) Barystatic sea-level curve of Miller *et al.* (2024). Grey vertical bands from Barnet *et al.* (2019). The "*" label denotes the unnamed carbon isotope excursion event of Littler *et al.* (2014) and Barnet *et al.* (2019) at ~58.15 Ma.

Elevated HTHO and HTHO/HFK values between ~290 and ~300 m WMSF, coinciding with the Barnet *et al*. (2019) PETM event band in the tuned ATS, provisionally locate the PETM within ~E405 cycles

25 and 26, corresponding to ~57.0-55.9 Ma, broadly consistent with the Zeebe and Lourens (2019) PETM age of 56.01 ± 0.05 Ma. A prominent positive HTHO anomaly at ~325 m WMSF is constrained to ~58.15 Ma, tightly bracketed by B *Discoaster mohleri* (~58.97 Ma) immediately above, which provides a firm upper biostratigraphic bound.

Table 2 Biostratigraphic datums used and excluded from ATS calibration at Holes U1579D and U1514C. B = base (first occurrence); T = top (last occurrence); Bc = consistent occurrence base.

Hole U1579D - Agulhas Plateau (Expedition 392)					
Taxon	**Event**	**Age (Ma)**	**Depth (m WMSF)**	**Status**	**Justification**
Cruciplacolithus primus	B	65.77	431.42	**Used**	-
Chiasmolithus danicus	B	64.53	420.25	**Used**	-
Prinsius martinii	B	63.66	413.19	**Used**	-
Sphenolithus moriformis	B	62.10	368.09	**Used**	-
Fasciculithus tympaniformis	B	61.27	373.58	**Used**	-
Heliolithus kleinpellii	B	59.36	351.37	**Used**	-
Discoaster mohleri	B	58.97	337.43	**Used**	-
Discoaster multiradiatus	B	57.32	318.04	**Used**	-
Tribrachiatus orthostylus	B	54.30	265.34	**Used**	-
T Cretaceous nannoflora	T	66.04	431.42	**Anchor**	Used as K-Pg positional anchor only; not a calibration datum *sensu stricto*. Reworked Cretaceous taxa above the boundary used as sediment-mixing indicators.
Cruciplacolithus intermedius	B	65.45	430.46	**Omitted**	Transitional morphologies of the *C. primus*-*C. intermedius* lineage complicate datum placement; inclusion did not improve correspondence with the La2004 target relative to the retained B *C. primus* datum.
Toweius pertusus	Bc	63.66	413.19	**Omitted**	Frequent taxonomic overlap with related species and inconsistent identification at this hole produced a mismatch with surrounding datums.
Heliolithus cantabriae	B	59.6	351.37	**Omitted**	Was not used for ATS calibration at Hole U1579D, as this datum was also absent from the Expedition 392 proceedings biostratigraphic framework.
Heliolithus kleinpellii	T	58.80	301.95	**Omitted**	Age in proceedings (~58.8 Ma) corresponds to the top of the range, not the FO; calibrated B *H. kleinpellii* at ODP Site 1262 is ~59.36-59.5 Ma. Applying the incorrect age would introduce a systematic bias.
Ericsonia robusta	T	57.11	286.36	**Omitted**	Size-threshold criterion (≥9 μm) introduces operator-dependent variability that limits reproducibility.
Rhomboaster spp.	B	56.00	269.70	**Omitted**	FO falls within the lowermost Eocene; taxon not recovered in the studied section (P/E boundary absent in the 16R-17R gap). Presence of *R. bramlettei* in sample 16R-CC (267.14 m CSF-A) confirms FO at or above the PETM level.
Campylosphaera eodela	B	56.00	269.70	**Omitted**	Limited biostratigraphic utility: small size and simple morphology yield inconsistent identification and unreliable correlation near the PETM.

Hole U1514C – Mentelle Basin (Expedition 369)					
Taxon	**Event**	**Age (Ma)**	**Depth (m WMSF)**	**Status**	**Justification**
Pseudoguembelina hariaensis	B	67.30	406.22	**Used**	-
Biantholithus sparsus	B	66.06	393.90	**Used**	-
Early Danian species	B	66.00	393.75	**Used**	-
Fasciculithus tympaniformis	B	61.51	363.47	**Used**	-
Globanomalina pseudomenardii	B	60.73	349.81	**Used**	-
Heliolithus cantabriae	B	59.60	340.21	**Used**	-
Discoaster mohleri	B	58.97	325.08	**Used**	-
Discoaster multiradiatus	B	57.21	304.75	**Used**	-
Fasciculithus spp.	T	55.64	280.38	**Used**	-
Tribrachiatus orthostylus	B	54.37	264.26	**Used**	-
Chiasmolithus danicus	B	64.81	392.17	**Omitted**	Placement produces an implausible compression of ~1 Myr into less than 2 m of section, inconsistent with the otherwise uniform sedimentation style at this depth.
Discoaster nobilis	B	57.5	314.25	**Omitted**	Depth position implies ~1.2 Myr for an interval biostratigraphy assigns only ~300 kyr; most parsimoniously explained by misidentification or reworking in a section with 65% core recovery.
Discoaster diastypus	B	54.95	280.38	**Omitted**	Warm-water, oligotrophic discoaster; occurrence strongly influenced by palaeolatitude, preservation, and ecological factors, compromising stratigraphic consistency at mid- to high-latitude sites.

4.4.2 Hole U1514C

Anchoring to the K-Pg boundary at ~393.9 m WMSF (B *Biantholithus sparsus*, 66.06 Ma – Huber *et al*., 2019), approximately 25 E405 cycles are identified between the K-Pg boundary and the PETM interval, with the full studied section yielding a total of 29 E405 cycles (~11.745 Myr; Fig. 6). Ten calcareous nannofossil and foraminiferal biostratigraphic datums were incorporated into the ATS calibration via top/bottom tuning (Table 2); three additional datums from the Expedition 369 proceedings were excluded based on low biochronological diagnostic value or internal inconsistency with the cyclostratigraphic framework (Table 2).

The tuned ATS places the PETM at ~E405 cycle 25 (~285 m WMSF), broadly consistent with Huber *et al.* (2019) assignment at ~278–283 m WMSF. A prominent positive HTHO anomaly at ~313 m WMSF is constrained to ~58.15 Ma in the U1514C ATS.

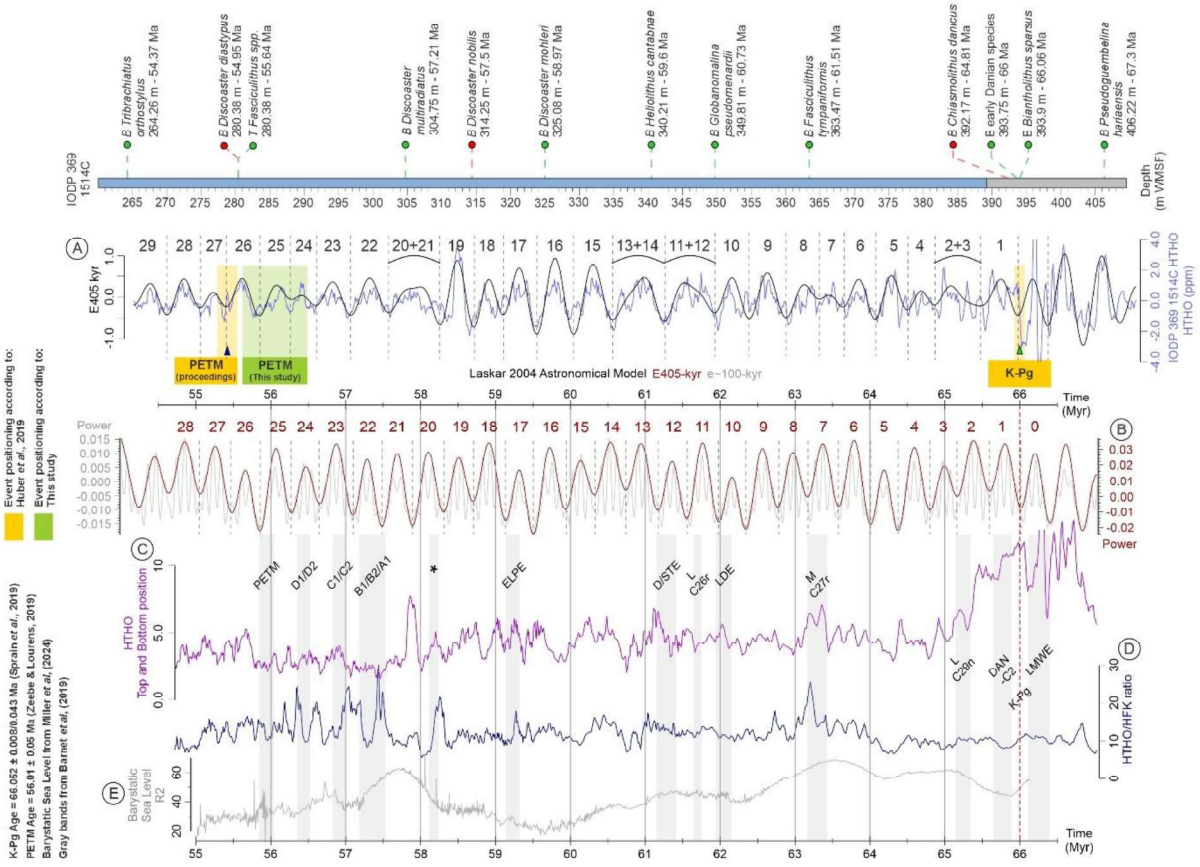


Figure 6 – Astronomical time scale for Hole U1514C based on the La2004 solution, with panels as in Fig. 5. The ATS places the prominent HTHO anomaly at ~313 m WMSF at ~58.15 Ma, co-temporal with the "*" CIE event at U1579D (Fig. 5). The PETM is tentatively placed at ~cycle 25 (~285 m WMSF), broadly consistent with the expedition proceedings assignment at ~278-283 m WMSF. Biostratigraphic datums applied in ATS calibration are shown as green markers; excluded datums as red markers. The "*" label marks the interpreted position of the unnamed ~58.15 Ma carbon isotope excursion event.

5 DISCUSSION

5.1 SAR CONVERGENCE, ORBITAL RESOLUTION, AND IMPLICATIONS FOR PETM AGE

The multi-method SAR evaluation indicates a convergence (COCO/eCOCO, TimeOpt) on ~1.1-2.1 cm/kyr for U1579D and ~1.0-1.8 cm/kyr for U1514C, which is consistent with typical open-ocean pelagic carbonate accumulation rates for the Paleocene-Eocene and agrees with expedition proceedings estimates (~1.7 cm/kyr for U1579D; ~1.4 cm/kyr for U1514C; Bohaty *et al*., 2023; Huber *et al*., 2019). As previously discussed, the dominance of the 405-kyr eccentricity cycle over shorter orbital cycles is primarily a consequence of sampling resolution. A straightforward explanation for the absence of precession imprint relative to the much better resolved 405-kyr eccentricity component lies in the Nyquist limit (1/30.48 cm^{-1}) imposed by the logging resolution, which implies that precession-scale variability falls at or below the theoretical resolution threshold, thereby preventing its robust spectral detection. Although not overtly evident, the obliquity detection at U1579D is consistent with the subdued 39-kyr expression in warm Paleocene

greenhouse conditions (Laskar *et al*., 2004; Littler *et al*., 2014; Barnet *et al*., 2019); its absence at U1514C may reflect the higher background noise level at that hole.

The E405 cycle count of ~25.5 at U1579D, and ~25 at U1514C is consistent with the 25-cycle interpretation now favoured by most recent studies (Hilgen *et al*., 2010; Dinarès-Turell *et al*., 2014), supporting a PETM age close to 56.01 ± 0.05 Ma (Zeebe and Lourens, 2019) rather than the ~55.93 Ma implied by a 24-cycle count (Westerhold *et al*., 2008). The findings regarding-cycle placement at both holes, compatible with the 25-cycle framework given the current age uncertainties, adds new Southern Hemisphere orbital constraints to this framework.

5.2 INPEFA AND DEPOSITIONAL TRENDS

The INPEFA curve at U1579D defines two contrasting phases: a gradually decreasing trend from the K-Pg to ~330 m WMSF, and an abrupt shift at ~325 m WMSF to a more heterogeneous plateau-like shape. This two-phase structure mirrors the late Paleocene progressive warming and carbon-cycle destabilisation documented globally from ~59 Ma onward (Zachos *et al*., 2001, 2008; Westerhold *et al*., 2020) and broadly coincides with the ELPE (~59.2 Ma) and the "*" CIE event (~58.15 Ma) interval in the Barnet *et al*. (2019) orbital framework. Comparison with the Miller *et al*. (2024) barystatic sea-level record shows broadly consistent first-order trends, suggesting that eustatic forcing may be indirectly reflected in the INPEFA signal through its influence on terrigenous clay delivery and carbonate accumulation at this deep-marine site.

At U1514C, the INPEFA curve shows broadly similar first-order trends, a decreasing phase from the K-Pg followed by a trend reversal, but with greater noise and a less intuitive inflection structure, consistent with the lithological heterogeneity and intermittent reworking at this hole. The abrupt positive inflection at ~313 m WMSF at U1514C is co-temporal with the prominent HTHO anomaly at ~325 m WMSF at U1579D, both constrained to ~58.15 Ma in the ATS. This co-temporal INPEFA inflection across two geographically separated sites is consistent with a globally coherent depositional signal associated with the "*" CIE event and the broader late Paleocene carbon-cycle transition.

It is important to highlight that the INPEFA method was originally developed for shallow-water siliciclastic settings (Nio *et al*., 2005; de Jong *et al*., 2007), where gamma-ray variations reflect grain-size changes controlled by relative sea level. Caution is therefore advised when applying it to deep-water pelagic carbonate sequences such as U1579D, where HTHO variability primarily reflects orbital-scale terrigenous clay flux and carbonate dilution rather than direct grain-size changes linked to sea-level oscillations. In this context, INPEFA trends are interpreted here as proxies for long-term shifts in the balance between clay input and carbonate production, rather than as direct sea-level indicators.

5.3 SPECTRAL RESOLUTION AND LITHOLOGICAL EFFECTS ON LONG-ECCENTRICITY BAND DEFINITION

A noticeable difference between the cyclostratigraphic analyses performed for Holes U1579D and U1514C emerges from the comparison of their MTM and EHA patterns. Whereas the U1579D results show greater lateral stability of the eCOCO-supported SAR range and lower distortion of the tuned ATS curves, the EHA spectrogram for U1514C suggests that two distinct frequency components partially overlap within the Paleocene interval studied here. This may reflect an apparent transient coalescence between low-frequency spectral power and the E405 component, partially obscuring the precise definition of the long-eccentricity frequency band. Such behavior provides a plausible explanation for stratigraphic intervals in which million-year-scale variability, finite depth–frequency resolution, and SAR changes may interact (Martinez *et al*., 2016).

Some differences in lithological aspects are relevant among both records – which may reflect in the distinctive depth-frequency patterns (see Figs 5 and 6). U1579D is entirely within homogeneous nannofossil chalk (Subunit IIb) - a ~407 m succession with only faint decimeter-scale clay variations and no significant reworking within the Paleocene section (Bohaty *et al*., 2023) - providing a low-noise substrate for orbital signal preservation. U1514C, by contrast, spans both clayey nannofossil ooze/chalk and nannofossil chalk, with the clay-rich facies possibly introducing non-orbital sedimentological variability.

5.4 THANETIAN ANOMALY AT ~58.15 MA: THE "*" CIE AND ITS PALAEOCLIMATIC CONTEXT

The prominent positive HTHO anomalies at ~325 m WMSF (U1579D) and ~313 m WMSF (U1514C) are independently constrained to ~58.15 Ma at both holes. Their simultaneous expression at the Agulhas Plateau and the Naturaliste Plateau argues for a globally coherent sedimentary event rather than a local depositional artefact. The age of ~58.15 Ma corresponds to the unnamed "*" carbon isotope excursion originally identified by Littler *et al*. (2014) in high-resolution benthic stable isotope records from ODP Sites 1209 (equatorial Pacific) and 1262 (Walvis Ridge, South Atlantic), and retained in the orbital framework of Barnet *et al*. (2019). This excursion falls within the Paleocene Carbon Isotope Maximum (PCIM, 59.3–57.4 Ma), approximately 1.0–1.1 Myr after the ELPE (~59.2 Ma), and marks the termination of the POIM (59.7–58.1 Ma; Hollis *et al*., 2022).

Hollis *et al.* (2022) note that the "*" CIE event coincides with a minimum in eccentricity forcing within a ~1 Myr decline that begins at the ELPE eccentricity maximum, an orbital context that contrasts with that of classical hyperthermals, which typically occur during eccentricity maxima (Barnet *et al.,* 2019). This orbital positioning, combined with the absence of robust evidence for deep-water warming in benthic $\delta^{18}O$ records at this time, led Hollis *et al*. (2022) to suggest that the "*" CIE is not a hyperthermal *sensu stricto*, but rather represents a significant carbon-cycle transition: the end of the decoupling interval between $\delta^{13}C$ and $\delta^{18}O$ that begins with the ELPE, and the transition from the cooler middle Paleocene to the warming late Paleocene. The sedimentary expression of the "*" CIE event as a positive HTHO anomaly at U1579D is consistent with a brief

episode of enhanced clay flux or carbonate dilution. The FO of *Discoaster mohleri* (~58.97 Ma) is recorded just above the anomaly at both holes, providing an independent biostratigraphic upper bound consistent with a ~58.15 Ma age at each location. Furthermore, comparing the ATS of both holes, the chronostratigraphic position of this event appears to differ by one E405 cycle between sites, which may reflect discrepancies between the shipboard biostratigraphic interpretations at Holes U1514C and U1579D. Confirmation of the specific event identity requires paired $\delta^{13}C$ and $\delta^{18}O$ data from these holes.

5.5 PETM REPOSITIONING

At U1579D, high amplitude spectral peaks in both HTHO and HTHO/HFK ratio curves between ~290 and ~300 m WMSF coincide with the Barnet *et al.* (2019) PETM event band in the tuned ATS, provisionally locating the PETM at ~E405 cycle 25.5 (~55.7-55.9 Ma), slightly deeper than the IODP Expedition 392 proceedings' assignment (~267-271 m CSF-A). This offset is most plausibly explained by poor core recovery in the 16R-17R gap where the proceedings note that the Paleocene/Eocene boundary is missing; cycle 25.5 falls within Core 19R, below this gap. The HTHO/HFK ratio divergence near ~280-290 m WMSF at U1579D provides an independent wireline-based sedimentological fingerprint of the PETM carbonate dissolution horizon, corroborating the cyclostratigraphic placement.

At U1514C, the PETM is tentatively placed at ~E405 cycle 25 (~285 m WMSF), broadly consistent with the IODP Expedition 369 proceedings' assignment at ~278-283 m WMSF, and the Th/K excursion at around this depth possibly provides a corresponding independent sedimentological fingerprint of the PETM at this hole.

5.6 GLOBAL CORRELATION AND FORWARD PERSPECTIVES

The anomalies at ~325 m WMSF (U1579D) and ~313 m WMSF (U1514C), co-temporal at ~58.15 Ma, fall in the same orbital position as the "*" CIE event identified in the South Atlantic (Littler *et al*., 2014; Barnet *et al*., 2019) and the southwest Pacific (Hollis *et al*., 2022), adding two new Southern Hemisphere constraints from the Indian Ocean sector to the orbital chronology of this event and confirming that its sedimentary expression extends from the South Atlantic to the southern and eastern Indian Ocean. The weak obliquity expression at U1579D, and its apparent absence at U1514C, is consistent with the warm greenhouse boundary conditions of the Paleocene, where obliquity power is negligible relative to eccentricity (Barnet *et al*., 2019; Littler *et al*., 2014).

The E405 cycle count of ~25.5 at U1579D and ~25 at U1514C align with the now-favoured 25-cycle interpretation of Hilgen *et al.* (2010), Dinarès-Turell *et al*. (2014) and Zeebe and Lourens (2019), and is consistent with the CENOGRID astronomical calibration of Westerhold *et al.* (2020). Future integration of stable isotope stratigraphy from both holes with the present orbital framework would provide the most rigorous test of PETM positioning and hyperthermal pacing, and "*" CIE identification, enabling direct confirmation through paired $\delta^{13}C$ and $\delta^{18}O$ data.

6 CONCLUSIONS

1. Indian Ocean IODP boreholes U1579D and U1514C preserve a dominant E405-kyr signal (wavelenght band 4.55-8.40 m at U1579D; 7.19-4.24 m at U1514C). COCO, eCOCO, and TimeOpt analyses converge on SAR estimates of ~1.1-2.1 cm/kyr for U1579D (mainly ~1.5-1.7 cm/kyr) and ~1.0-1.8 cm/kyr for U1514C. Short eccentricity cycles are tentatively suggested but lack continuous EHA expression. Obliquity is tentatively identified at U1579D; precession is unresolvable at the 15.2 cm sampling resolution.

2. ATS calibration using top/bottom biostratigraphic datum positions shows overall good correspondence with the La2004 target in the middle Paleocene. Approximately 25.5 E405 cycles at U1579D and 25 at U1514C are identified between the K-Pg and PETM, provisionally constraining the PETM to ~55.7–55.9 Ma.

3. The prominent HTHO anomaly at ~325 m (U1579D) and ~313 m (U1514C) is co-temporal at ~58.15 Ma. This age is consistent with the unnamed "*" CIE, which marks the termination of the POIM and the end of the $\delta^{13}C$- $\delta^{18}O$ decoupling interval that begins with the ELPE (~59.2 Ma). The CIE occurs close to an eccentricity minimum and is understood as not being a classical hyperthermal; its expression as positive HTHO anomaly is consistent with carbonate dilution or enhanced clay flux, paired with rapid increase in sediment density, during this global carbon-cycle transition. The co-temporal expression at two geographically separated Indian Ocean locations argues for a globally coherent sedimentary signal.

4. INPEFA modelling allowed us to identify trend reversals at both holes consistent with depositional regime changes at the K-Pg boundary and near the ELPE/"*" CIE event interval, broadly consistent with the Paleocene barystatic sea-level record of Miller *et al.* (2024). INPEFA curves are interpreted here as potential indicators of variations in terrigenous clay flux rather than direct sea-level proxies and may therefore provide a wireline-based perspective on Paleocene depositional dynamics in deep-water pelagic carbonate settings.

5. A comparison of the MTM and EHA patterns for Holes U1579D and U1514C reveals distinct depth–frequency behavior. U1579D shows greater lateral stability of the eCOCO-supported SAR range and lower distortion of the tuned ATS curves, whereas the EHA spectrogram for U1514C indicates partial overlap between low-frequency spectral power and the E405 component, potentially affecting the definition of the long-eccentricity band. These differences occur in contrasting lithological settings: U1579D consists of relatively homogeneous nannofossil chalk, while U1514C spans clayey nannofossil ooze/chalk and nannofossil chalk, with clay-rich facies potentially introducing non-orbital sedimentological variability.

Data availability

The wireline log data used in this study are publicly available from the LDEO Log Database (https://mlp.ldeo.columbia.edu/). Processed data and R scripts are presented in the supplementary material and available upon request.

Declaration of generative AI and AI-assisted technologies in the manuscript preparation process

During the preparation of this work, the authors used Claude (Anthropic; Sonnet v. 4.6) to assist with textual revision and organisation of scientific content. After using this tool, the authors reviewed and edited all content as needed and take full responsibility for the content of the published article.

Acknowledgements

The authors acknowledge the International Ocean Discovery Program (IODP) and the science parties of Expeditions 392 and 369 for recovering the sediment cores and acquiring the wireline log data used in this study. We also thank the financed support from CAPES (88887.893883/2023-00 to B.M.M.), CNPq (314462/2020-1 and 313253/2017-0 to D.R.F.) and FAPERJ (E-26/200.931/2022 and E-26/203.302/2017 to D.R.F., and 204.404/2021 to M.C.).

REFERENCES

Adams, J.A., Weaver, C.E., 1958. Thorium-to-uranium ratios as indicators of sedimentary processes: example of concept of geochemical facies. AAPG Bulletin, 42(2), 387–430.

Agnini, C., Fornaciari, E., Raffi, I., Rio, D., Röhl, U., Westerhold, T., 2007. High-resolution nannofossil biochronology of middle Paleocene to early Eocene at ODP Site 1262: Implications for calcareous nannoplankton evolution. Marine Micropaleontology, 64(3-4), 215–248.

Alvarez, L.W., Alvarez, W., Asaro, F., Michel, H.V., 1980. Extraterrestrial cause for the Cretaceous-Tertiary extinction. Science, 208(4448), 1095–1108.

Barnet, J.S., Littler, K., Westerhold, T., Kroon, D., Leng, M.J., Bailey, I., Zachos, J.C., 2019. A high-fidelity benthic stable isotope record of late Cretaceous–early Eocene climate change and carbon-cycling. Paleoceanography and Paleoclimatology, 34(4), 672–691.

Barnosky, A.D., Matzke, N., Tomiya, S., et al., 2011. Has the Earth's sixth mass extinction already arrived? Nature, 471(7336), 51–57.

Bohaty, S.M., Uenzelmann-Neben, G., Childress, L.B., et al., 2023. Site U1579. In: Uenzelmann-Neben, G., Bohaty, S.M., Childress, L.B., and the Expedition 392 Scientists, Agulhas Plateau Cretaceous Climate. Proc. Int. Ocean Discov. Program 392. https://doi.org/10.14379/iodp.proc.392.103.2023.

Burgess, S., 2019. Deciphering mass extinction triggers. Science, 363(6429), 815–816.

Cleveland, W.S., 1981. LOWESS: A Program for Smoothing Scatterplots by Robust Locally Weighted Regression. The American Statistician, 35(1), 54. https://doi.org/10.2307/2683591.

Clyde, W.C., Ramezani, J., Johnson, K.R., Bowring, S.A., Jones, M.M., 2016. Direct high-precision U–Pb geochronology of the end-Cretaceous extinction and calibration of Paleocene astronomical timescales. Earth and Planetary Science Letters, 452, 272–280.

De Vleeschouwer, D., Dunlea, A.G., Auer, G., et al., 2017. Quantifying K, U, and Th contents of marine sediments using shipboard natural gamma radiation spectra measured on DV JOIDES Resolution. Geochemistry, Geophysics, Geosystems, 18(3), 1053–1064.

Dinarès-Turell, J., Westerhold, T., Pujalte, V., Röhl, U., Kroon, D., 2014. Astronomical calibration of the Danian stage (Early Paleocene) revisited: Settling chronologies of sedimentary records across the Atlantic and Pacific Oceans. Earth and Planetary Science Letters, 405, 119–131.

Gradstein, F.M., Ogg, J.G., Schmitz, M.D., Ogg, G.M. (Eds.), 2020. The Geologic Time Scale 2020. Elsevier, Amsterdam.

Hilgen, F.J., Kuiper, K.F., Lourens, L.J., 2010. Evaluation of the astronomical time scale for the Paleocene and earliest Eocene. Earth and Planetary Science Letters, 300(1–2), 139–151.

Hinnov, L.A., 2013. Cyclostratigraphy and its revolutionizing applications in the earth and planetary sciences. Geological Society of America Bulletin, 125(11–12), 1703–1734.

Hinnov, L.A., 2018. Cyclostratigraphy and astrochronology in 2018. In: Stratigraphy & Timescales, Vol. 3, pp. 1–80. Academic Press.

Huber, B. T., Hobbs, R. W., Bogus, K. A., Batenburg, S. J., Brumsack, H. J., do Monte Guerra, R., ... & Xu, Z., 2019. Expedition 369 summary. Proceedings of the International Ocean Discovery Program, 369, 101.

Hollis, C.J., et al., 2022. The Paleocene–Eocene carbon isotope excursion in higher plant organic matter: differential fractionation of angiosperms and conifers in the New Zealand record. Geological Magazine, 159(7), 1024–1044.

Hull, P., 2015. Life in the aftermath of mass extinctions. Current Biology, 25(19), R941–R952.

Laskar, J., Robutel, P., Joutel, F., Gastineau, M., Correia, A.C., Levrard, B., 2004. A long-term numerical solution for the insolation quantities of the Earth. Astronomy & Astrophysics, 428, 261–285.

Li, M., Kump, L. R., Hinnov, L. A., & Mann, M. E., 2018. Tracking variable sedimentation rates and astronomical forcing in Phanerozoic paleoclimate proxy series with evolutionary correlation coefficients and hypothesis testing. Earth and Planetary Science Letters, 501, 165-179.

Li, M., Hinnov, L., Kump, L., 2019. Acycle: Time-series analysis software for paleoclimate research and education. Computers & Geosciences, 127, 12–22.

Littler, K., Röhl, U., Westerhold, T., Zachos, J.C., 2014. A high-resolution benthic stable-isotope record for the South Atlantic: Implications for orbital-scale changes in late Paleocene–early Eocene climate and carbon cycling. Earth and Planetary Science Letters, 401, 18–30.

Mann, M.E., Lees, J.M., 1996. Robust estimation of background noise and signal detection in climatic time series. Climatic Change, 33, 409–445.

Martinez, M., Kotov, S., De Vleeschouwer, D., Pas, D., Pälike, H., 2016. Testing the impact of stratigraphic uncertainty on spectral analyses of sedimentary series. Climate of the Past 12, 1765–1783. https://doi.org/10.5194/cp-12-1765-2016

McInerney, F.A., Wing, S.L., 2011. The Paleocene-Eocene Thermal Maximum: A perturbation of carbon cycle, climate, and biosphere with implications for the future. Annual Review of Earth and Planetary Sciences, 39, 489–516.

Meyers, S.R., 2012. Seeing red in cyclic stratigraphy: spectral noise estimation for astrochronology. Paleoceanography, 27, PA3228.

Meyers, S.R., 2015. The evaluation of eccentricity-related amplitude modulation and bundling in paleoclimate data: an inverse approach for astrochronologic testing and time scale optimization. Paleoceanography, 30, 1625–1640.

Miller, K.G., Schmelz, W.J., Browning, J.V., Rosenthal, Y., Hess, A.V., Kopp, R.E., Wright, J.D., 2024. Global mean and relative sea-level changes over the past 66 Myr: implications for early Eocene ice sheets. Earth Science, Systems and Society, 3, 10091.

Nio, S.D., Brouwer, J., Smith, D.G., de Jong, M., Böhm, A., 2005. Spectral trend attribute analysis: applications in the stratigraphic analysis of wireline logs. First Break, 23, 71–75.

Ruffell, A., Worden, R., 2000. Palaeoclimate analysis using spectral gamma-ray data from the Aptian (Cretaceous) of southern England and southern France. Palaeogeography, Palaeoclimatology, Palaeoecology, 155(3–4), 265–283.

Schnyder, J., et al., 2006. Conjunctive use of spectral gamma-ray logs and clay mineralogy in defining late Jurassic–early Cretaceous palaeoclimate change. Palaeogeography, Palaeoclimatology, Palaeoecology, 229, 303–320.

Schulte, P., et al., 2010. The Chicxulub asteroid impact and mass extinction at the Cretaceous-Paleogene boundary. Science, 327(5970), 1214–1218.

Sprain, C.J., Renne, P.R., Vanderkluysen, L., Pande, K., Self, S., Mittal, T., 2019. The eruptive tempo of Deccan volcanism in relation to the Cretaceous-Paleogene boundary. Science 363, 866–870. https://doi.org/10.1126/science.aav1446.

Uenzelmann-Neben, G., Bohaty, S.M., Childress, L.B., et al., 2023. Expedition 392 summary. In: Uenzelmann-Neben, G., Bohaty, S.M., Childress, L.B., and the Expedition 392 Scientists, Agulhas Plateau Cretaceous Climate. Proc. Int. Ocean Discov. Program, 392.

van Hinsbergen, D.J.J., et al., 2015. A paleolatitude calculator for paleoclimate studies. PLoS ONE, 10(6), e0126946.

Westerhold, T., Röhl, U., Raffi, I., et al., 2008. Astronomical calibration of the Paleocene time. Palaeogeography, Palaeoclimatology, Palaeoecology, 257, 377–403.

Westerhold, T., et al., 2020. An astronomically dated record of Earth's climate and its predictability over the last 66 million years. Science, 369(6509), 1383–1387.

Zachos, J., Pagani, M., Sloan, L., Thomas, E., Billups, K., 2001. Trends, rhythms, and aberrations in global climate 65 Ma to present. Science, 292(5517), 686–693.

Zachos, J.C., Röhl, U., Schellenberg, S.A., et al., 2005. Rapid acidification of the ocean during the Paleocene-Eocene Thermal Maximum. Science, 308(5728), 1611–1615.

Zeebe, R.E., Lourens, L.J., 2019. Solar system chaos and the Paleocene-Eocene boundary age constrained by geology and astronomy. Science, 365(6456), 926–929.

SUPLEMENTARY MATERIAL

Cyclostratigraphy of Agulhas Plateau and Mentelle Basin records (IODP Expeditions 392 and 369): an orbitally-based chronostratigraphy from the K–Pg boundary to the PETM

Bernardo Mokan Maffessoni*, Mariane Candido, João Maurício Figueiredo Ramos, Daniel Ribeiro Franco, Mateus Fontana Michelon, Raysa de Magalhães Rocha

* Corresponding author.

E-mail address: bmmaffessoni@gmail.com

This section includes:

Methods supplementary texts and figures

Text S1: Cross-Correlation Function (CCF) Routine: Description and Parameterisation

Figure S1 (Raw curves comparison)

Figure S2 (CCF, both holes)

Text S2: INPEFA Methodology, Parameter Sensitivity and Annotated Python Script

Text S3: Detrending Method Evaluation: Comparison and Selection Rationale

Figure S3 (Detrending comparison, Hole U1579D)

Figure S4 (Detrending comparison, Hole U1514C)

Text S4: Linear Detrend Cyclostratigraphic Analysis: Methodology and Interpretation

Figure S5 (Linear detrend, Hole U1579D)

Figure S6 (Linear detrend, Hole U1514C)

Text S5: Expanded SAR Estimation: COCO, eCOCO, and TimeOpt Results

Figure S7 (SAR estimation, Hole U1579D)

Figure S8 (SAR estimation, Hole U1514C)

Text S6: Wavelet Transform Analysis: Methodology and Interpretation

Figure S9 (Wavelet, Hole U1579D)

Figure S10 (Wavelet, Hole U1514C)

Text S7: E405-kyr cycle positions for Holes U1579D and U1514C

Table S1 (Cycle positions, Holes U1579D and U1514C)

Text S1: Cross-Correlation Function (CCF) Routine: Description and Parameterisation

S1.1 Overview

A custom cross-correlation function (CCF) routine was developed in RStudio (v.2025.05.1+513) using R (v.4.5.1; R Core Team, 2025) to quantify the degree of linear association and phase relationship between all pairwise combinations of four spectral gamma-ray (NGR) proxies measured at both Holes U1579D (IODP Expedition 392) and U1514C (IODP Expedition 369): total spectral gamma ray (HSGR), potassium (HFK), thorium (HTHO), and uranium (HURA) (see Fig. S1; U1579D upper half; U1514C lower half). The routine operates on depth-registered, regularly sampled wireline log series and returns, for each proxy pair, the maximum absolute correlation coefficient (|r|) and the corresponding lag displacement at which that maximum occurs. Results for each pair are exported as individual PNG figures (both in lag units and metres), which are subsequently assembled into a 2×3 composite panel, panels per hole (Fig. S2; U1579D upper half; U1514C lower half).

The CCF approach used here follows the standard definition of the cross-correlation function for two zero-mean, stationary discrete series x and y of length N:

$$r_{xy}(k) = \Sigma\,[x(n) \cdot y(n+k)] \,/\, \mathrm{sqrt}[\Sigma\, x(n)^2 \cdot \Sigma\, y(n)^2]$$

where k is the lag displacement in sample units. The routine reports both the lag value in sample units and the corresponding metric lag distance (metres), calculated as k × 0.1524 m (the wireline sampling interval used in this study).

S1.2 Input data and file structure

Input files are tab-delimited .txt files, one per proxy per hole, with two columns (depth in metres MWSF; proxy value). Files are named following the convention [expedition]_[hole]_[proxy]_[chrons].txt, which allows automatic detection of hole identity and proxy type via regular-expression parsing. No smoothing, detrending, or normalisation is applied prior to the CCF analysis; the raw wireline values are used directly. It is worth noting that the code was developed to work with one or more boreholes and can be adapted accordingly. The depth window analysed for this study corresponds to the K-Pg to PETM interval at Hole U1579D: 255-440 m WMSF, and at Hole U1514C: 265-410 m WMSF.

S1.3 Pair generation logic

The routine generates pairs in a structured order designed to prioritise geologically informative comparisons. Three groups of pairs are constructed: (1) HSGR vs. each of the remaining proxies; (2) HTHO vs. each of the remaining proxies; and (3) all combinations among the remaining proxies (HFK and HURA). Within each pair, HSGR and HTHO are placed first where applicable, ensuring consistent axis orientation across figures. Duplicate pairs are removed after sorting. This yields the six pairs for each Hole, shown in Fig. S2: HSGR-HFK (A), HSGR-HTHO (B), HSGR-HURA (C), HTHO-HFK (D), HTHO-HURA (E), HFK-

HURA (F). The CCF pair HTHO-HURA (panel E) specifically illustrates the positive lag of HURA relative to HTHO, which constitutes the primary basis for disqualifying HURA as a primary cyclostratigraphic proxy.

S1.4 CCF computation and output

For each pair, the CCF is computed using the R base function:

```
ccf(ts(x), ts(y), lag.max = 100, type = "correlation", plot = FALSE)
```

The lag.max = 100 setting restricts the search to ±100 sample units, corresponding to ±15.24 m at the 0.1524 m sampling interval. The lag k* at which |r_xy(k)| is maximised is identified and converted to metres (k* × 0.1524 m). Two figures are generated per pair: one with the x-axis in lag units and one in metres. Both are saved as 300 dpi PNG files. A console summary reports, for each pair, the maximum |r| and the corresponding lag in both units.

The significance of each maximum |r| value is assessed informally against the threshold for two-tailed significance at $p < 0.01$, approximated as $|r| \approx 0.06$-0.07 for the dataset lengths used here (~1150-1500 data points); all reported |r| values substantially exceed this threshold.

S1.5 Interpretation of lag values

A positive lag value ($k^* > 0$) indicates that proxy y trails proxy x stratigraphically, interpreted as proxy y responding to the same depositional process as proxy x but with a diagenetic or geochemical delay. A negative lag ($k^* < 0$) indicates that proxy y leads proxy x. A lag of zero indicates stratigraphic coincidence. At U1579D, CCF analysis display zero-lag, high-|r| correlations of HTHO with both HSGR (|r| = 0.784) and HFK (|r| = 0.540), reflecting the geochemical immobility of thorium in terrigenous clay minerals under normal seawater and diagenetic conditions. This result suggests a synchronous response to the same lithological driver (terrigenous clay flux). HURA exhibits a systematic positive lag of 2.438 m relative to HTHO (Fig. S2, panel E - upper half), suggesting post-depositional uranium remobilisation under variable redox conditions (Adams and Weaver, 1958; Schnyder *et al.*, 2006). At U1514C, HTHO shows even stronger zero-lag correlations with HSGR (|r| = 0.917) and HFK (|r| = 0.923), while HURA exhibits a larger positive phase lag of 3.962 m relative to HTHO (Fig. S2, panel E - lower half), consistent with more active uranium remobilisation in the clay-rich sedimentary environment of the Mentelle Basin. Because such lag relationships introduce phase-shifted variance into the total NGR signal that could be misinterpreted as orbital cycles, HURA is excluded as a primary cyclostratigraphic proxy in this study. Therefore, the cross-correlation analysis demonstrates that HTHO is the most suitable NGR spectral component for cyclostratigraphic analysis at both holes.

S1.6 Software, packages and reproducibility

All analyses were performed in R version 4.5.1. Packages: base R (ccf), ggplot2 v3.x (Wickham, 2016), dplyr v1.1.x (Wickham *et al.*, 2023), patchwork (Pedersen, 2024), cowplot (Wilke, 2024), png

(Urbanek, 2022), grid (R Core Team, 2025). Processed data and R scripts are available upon request from the corresponding author.

S1.8 Annotated R script (v2.3)

The full script is reproduced below for transparency and reproducibility. Path variables (setwd, pasta_png) are specific to the authors' local environment and must be adapted by the user.

```
# ------------------------------------------------
# CROSS-CORRELATION ANALYSIS (CCF)
# Author: Maffessoni, B. (ccf_automatizado.R)
# Version: 2.3
# ------------------------------------------------

# PART 1 — CCF COMPUTATION
library(ggplot2); library(dplyr)
setwd("path/to/CCF/folder")   # adapt to local environment
path <- getwd()

# Detect files, holes and proxies from filenames
arquivos_txt <- list.files(path, pattern = "\.txt$", full.names = FALSE)
pocos   <- sub("^[^_]+_([^_]+)_.*$", "\1", arquivos_txt)
proxies <- sub("^[^_]+_[^_]+_([A-Za-z]+).*\.txt$", "\1", arquivos_txt)
dados_arquivos <- data.frame(arquivo = arquivos_txt, poco = pocos, proxy =
proxies)

# Standard plot theme
tema_ccf <- theme_minimal() +
  theme(axis.title = element_text(size = 14),
        axis.text  = element_text(size = 12),
        plot.title = element_text(size = 16),
        panel.border = element_rect(color = "black", fill = NA, linewidth
= 0.8))

# Main CCF function
analisar_ccf <- function(dados_arquivos, path, pasta_saida =
"CCF_Results") {
  if (!dir.exists(pasta_saida)) dir.create(pasta_saida, recursive = TRUE)
  resultados <- list()
  for (poco_atual in unique(dados_arquivos$poco)) {
    dados_poco <- dados_arquivos %>% filter(poco == poco_atual)
    proxies    <- unique(dados_poco$proxy)
    if (length(proxies) < 2) next
```

```
    # Generate pairs: HSGR-first, HTHO-first, then remaining combinations
    pares_hsgr     <- lapply(setdiff(proxies, "HSGR"), function(x)
c("HSGR", x))
    pares_htho     <- lapply(setdiff(proxies, "HTHO"), function(x)
c("HTHO", x))
    restantes      <- setdiff(proxies, c("HSGR", "HTHO"))
    pares_restantes <- if (length(restantes) >= 2) combn(restantes, 2,
simplify = FALSE) else list()
    pares <- c(pares_hsgr, pares_htho, pares_restantes)
    pares <- lapply(pares, function(x) {
      ordem <- c("HSGR", "HTHO")
      c(intersect(ordem, x), sort(setdiff(x, ordem))) })
    pares <- pares[!duplicated(pares)]


    for (par in pares) {
      var1 <- par[1]; var2 <- par[2]
      df1  <- read.table(file.path(path,
dados_poco$arquivo[dados_poco$proxy == var1][1]),
                         header = TRUE, col.names = c("depth", "value"))
      df2  <- read.table(file.path(path,
dados_poco$arquivo[dados_poco$proxy == var2][1]),
                         header = TRUE, col.names = c("depth", "value"))


      ccf_res  <- ccf(ts(df1$value), ts(df2$value), lag.max = 100, plot =
FALSE)
      ccf_df   <- data.frame(lag = as.numeric(ccf_res$lag),
                             correlation = as.numeric(ccf_res$acf))
      max_cor  <- max(abs(ccf_df$correlation))
      lag_max  <- ccf_df$lag[which.max(abs(ccf_df$correlation))]
      fator_m  <- 15.24 / 100
      ccf_df$lag_m <- ccf_df$lag * fator_m
      lag_max_m    <- lag_max * fator_m


      # Figure in lag units
      p <- ggplot(ccf_df, aes(x = lag, y = correlation)) +
        geom_line(color = "steelblue", linewidth = 0.6) +
        geom_area(fill = "steelblue", alpha = 0.4, color = "steelblue",
linewidth = 0.6) +
        geom_vline(xintercept = lag_max, linetype = "dashed", color =
"red") +
        scale_x_continuous(breaks = seq(-100, 100, by = 10)) +
        labs(title = paste("CCF:", var1, "vs", var2),
             subtitle = paste("Well:", poco_atual, "| Max |r| =",
```

```
                              round(max_cor, 3), "@ Lag =", lag_max),
             x = "Lag", y = "Correlation coefficient") + tema_ccf
      ggsave(file.path(pasta_saida,
             paste0("CCF_", poco_atual, "_", var1, "_", var2, ".png")),
             plot = p, width = 8, height = 5, dpi = 300)

      # Figure in metres
      p_m <- ggplot(ccf_df, aes(x = lag_m, y = correlation)) +
        geom_line(color = "steelblue", linewidth = 0.6) +
        geom_area(fill = "steelblue", alpha = 0.4, color = "steelblue",
linewidth = 0.6) +
        geom_vline(xintercept = lag_max_m, linetype = "dashed", color =
"red") +
        scale_x_continuous(breaks = seq(-15, 15, by = 2.5)) +
        labs(title = paste("CCF (m):", var1, "vs", var2),
             subtitle = paste("Well:", poco_atual, "| Max |r| =",
                              round(max_cor, 3), "@ Lag =",
                              round(lag_max_m, 3), "m"),
             x = "Lag (m)", y = "Correlation coefficient") + tema_ccf
      ggsave(file.path(pasta_saida,
             paste0("CCF_m_", poco_atual, "_", var1, "_", var2, ".png")),
             plot = p_m, width = 8, height = 5, dpi = 300)

      resultados[[paste(poco_atual, var1, var2, sep = "_")]] <- list(
        dataframe = ccf_df, max_correlation = max_cor,
        lag_max = lag_max, lag_max_m = lag_max_m)
    }
  }
  return(resultados)
}

resultados_ccf <- analisar_ccf(dados_arquivos, path)

# PART 2 — 2x3 COMPOSITE PANEL WITH PANEL LABELS
library(patchwork); library(png); library(grid); library(cowplot)

pasta_png <- "path/to/CCF_Results/convertido/1579D"  # adapt per hole
todos <- list.files(pasta_png, pattern = "\.png$", full.names = TRUE)
nomes <- basename(todos)
poco  <- sub("^CCF_m_([^_]+)_.*$", "\1", nomes[grepl("^CCF_m_",
nomes)][1])

# Helper: locate file by pair suffix
```

```
pegar <- function(sufixo) {
  match <- todos[grepl(paste0("^CCF_m_", poco, "_", sufixo, "\.png$"),
nomes)]
  if (length(match) == 0) stop(paste("File not found:", sufixo))
  match[1]
}

arquivos_6 <- c(pegar("HSGR_HFK"), pegar("HSGR_HTHO"), pegar("HSGR_HURA"),
                pegar("HTHO_HFK"), pegar("HTHO_HURA"), pegar("HFK_HURA"))

# Overlay circled letter labels
png_para_ggplot <- function(caminho, rotulo = "") {
  img    <- readPNG(caminho)
  raster <- rasterGrob(img, interpolate = TRUE)
  p <- ggplot() +
    annotation_custom(raster, xmin=-Inf, xmax=Inf, ymin=-Inf, ymax=Inf) +
    theme_void()
  ggdraw(p) +
    draw_grob(circleGrob(x=0.055, y=0.94, r=0.035,
              gp=gpar(fill="white", col="black", lwd=1.5))) +
    draw_label(rotulo, x=0.055, y=0.94, hjust=0.5, vjust=0.5,
               size=14, fontface="plain", color="black")
}

plots        <- mapply(png_para_ggplot, caminho=arquivos_6,
                       rotulo=c("A","B","C","D","E","F"), SIMPLIFY=FALSE)
figura_final <- (plots[[1]] | plots[[2]] | plots[[3]]) /
                (plots[[4]] | plots[[5]] | plots[[6]])

ggsave(file.path(pasta_png, paste0("painel_2x3_LETTERS_", poco, ".png")),
 plot=figura_final, width=18, height=10, dpi=300)
```

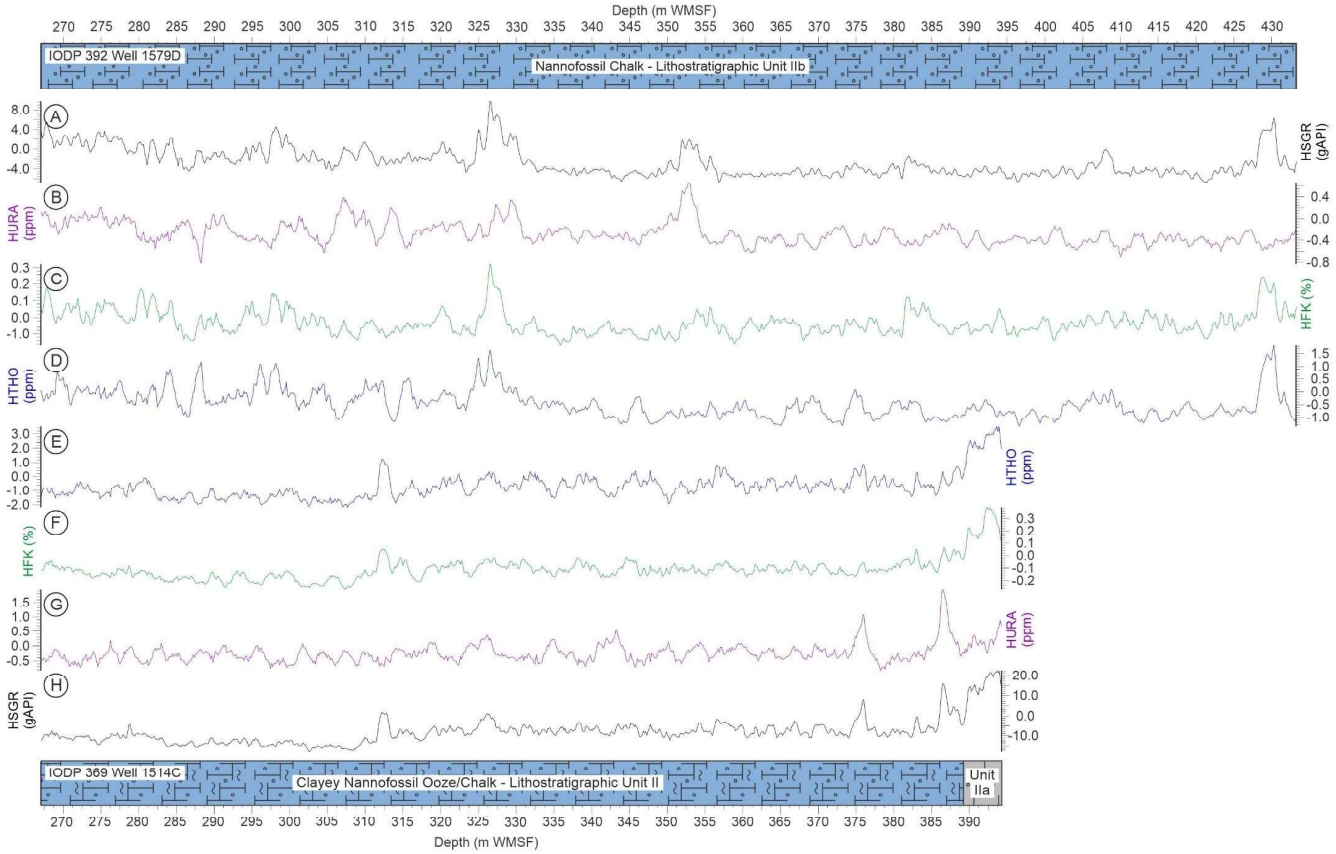


Figure S1: Plot of the total gamma-ray time series and its component channels. Hole U1579D = Panels: (A) HSGR, (B) HURA, (C) HFK, (D) HTHO. Hole U1514C = Panels: (E) HTHO, (F) HFK, (G) HURA, (H) HSGR. These were the time series to which the cross-correlation function was applied.

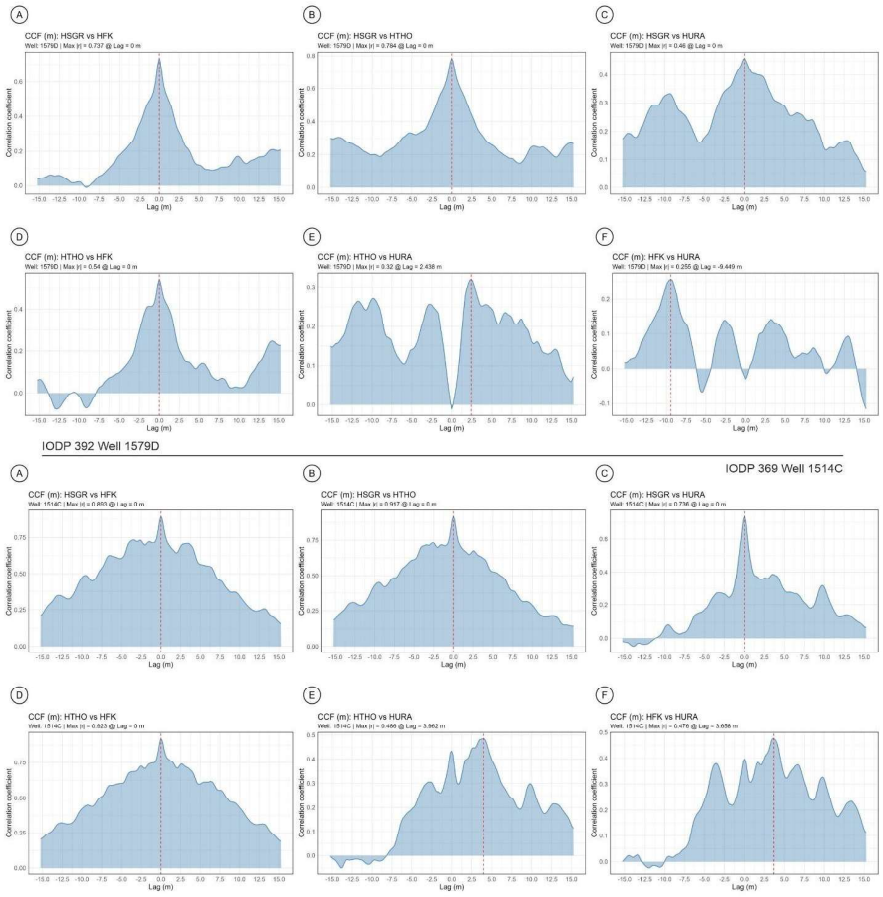


Figure S2: Cross-correlation function (CCF) analyses for all NGR proxy pairs at both IODP holes, showing correlation coefficient versus lag (m). Hole U1579D = upper panels: (A) HSGR-HFK, (B) HSGR-HTHO, (C) HSGR-HURA, (D) HTHO-HFK, (E) HTHO-HURA, (F) HFK-HURA. Hole U1514C = lower panels. Dashed red line indicates the lag at maximum |r|. Zero-lag, high-|r| correlations for HTHO (panels B and D) and HFK (panels A and D) with HSGR confirm synchronous response to the primary detrital clay-flux signal. For instance, the systematic positive lag of HURA relative to HTHO in panel E (2.438 m) and relative to HFK in panel F (−9.449 m) is interpreted as perhaps post-depositional uranium remobilisation under variable redox conditions.

REFERENCES

Adams, J.A., Weaver, C.E., 1958. Thorium-to-uranium ratios as indicators of sedimentary processes. AAPG Bull. 42, 387-430.

Box, G. E., Jenkins, G. M., Reinsel, G. C., & Ljung, G. M., 2015. Time series analysis: forecasting and control. John Wiley & Sons.

Chatfield, C., & Xing, H., 2019. The analysis of time series: an introduction with R. Chapman and hall/CRC.

Kwon, B. D., & Rudman, A. J., 1979. Correlation of geologic logs with spectral methods. Journal of the International Association for Mathematical Geology, 11(4), 373-390.

Pedersen, T.L., 2024. patchwork: The Composer of Plots. R package version 1.3.0 (CRAN 2024).

R Core Team, 2025. R: A Language and Environment for Statistical Computing. R Foundation for Statistical Computing, Vienna, Austria.

Ruffell, A., & Worden, R., 2000. Palaeoclimate analysis using spectral gamma-ray data from the Aptian (Cretaceous) of southern England and southern France. Palaeogeography, Palaeoclimatology, Palaeoecology, 155(3-4), 265-283.

Shumway, R. H., & Stoffer, D. S., 2017. Statistical methods in the frequency domain. In Time Series Analysis and Its Applications: With R Examples (pp. 385-471). Cham: Springer International Publishing.

Schnyder, J., et al., 2006. Conjunctive use of spectral gamma-ray logs and clay mineralogy in defining late Jurassic-early Cretaceous palaeoclimate change. Palaeogeogr. Palaeoclimatol. Palaeoecol. 229, 303-320.

Tribovillard, N., Algeo, T. J., Lyons, T., & Riboulleau, A., 2006. Trace metals as paleoredox and paleoproductivity proxies: An update. Chemical geology, 232(1-2), 12-32.

Urbanek, S., 2022. png: Read and write PNG images. R package version 0.1-8 (2022-11-01).

Wickham, H., 2016. ggplot2: Elegant Graphics for Data Analysis. Springer-Verlag, New York.

Wickham, H., François, R., Henry, L., Müller, K., Vaughan, D., 2023. dplyr: A Grammar of Data Manipulation. R package version 1.1.4 (2023-11-17).

Wilke, C.O., 2024. cowplot: Streamlined Plot Theme and Annotations for ggplot2. R package version 1.1.3 (2024-01-05).

Text S2: INPEFA Methodology, Parameter Sensitivity and Annotated Python Script

S2.1 Methodological background

The Integrated Prediction Error Filter Analysis (INPEFA) is a wireline log processing technique originally developed for stratigraphic correlation in the petroleum industry (Nio *et al*., 2005; de Jong *et al*., 2007) and subsequently applied to cyclostratigraphic analysis of deep-sea sediment sequences (Zulivandama

et al., 2018; Liu *et al*., 2024). The method detects depositional trend changes by quantifying the departure of an observed stratigraphic series from the behaviour predicted by an autoregressive (AR) model fitted to previous samples.

S2.2 Mathematical formulation

S2.2.1 Prediction Error Filter Analysis (PEFA)

The prediction error e_n at stratigraphic position n is defined as:

$$e_n = y_n - \Sigma(i=1 \text{ to } p)\ C_i \cdot y_{(n-i)}$$

where y_n is the observed proxy value at position n, C_i are the autoregressive coefficients estimated by the Burg method (forward-backward least-squares), and p is the prediction order (filter length). The term Σ C_i · y_(n−i) is the value predicted by the AR model from the preceding p samples. Positive prediction errors indicate that the observed value exceeds the model prediction, corresponding to upward increases in the proxy (here HTHO); negative errors indicate that the observed value falls below the prediction, corresponding to decreasing proxy values.

Prediction coefficients C_i are estimated using the Burg algorithm, which optimises forward and backward prediction simultaneously and is numerically stable for the short-to-moderate AR orders used here. The prediction order p is set to a length approximately equivalent to 10 m, following the recommendation of Nio *et al*. (2005) and de Jong *et al*. (2007); at the 0.1524 m sampling interval this corresponds to $p \approx 66$ coefficients. Sensitivity testing showed that varying p between 40 and 90 coefficients produced no qualitatively significant change in the INPEFA curves at U1579D, confirming the robustness of the result within this range.

S2.2.2 INPEFA integration

The INPEFA curve is computed as the running sum (numerical integration) of the PEFA prediction errors from the first sample to sample t:

$$INPEFA(t) = \Sigma(i=1 \text{ to } t)\ e_i$$

This integration acts as a low-pass filter on the PEFA series, suppressing high-frequency noise and revealing trends operating at stratigraphic scales longer than the prediction filter length. The INPEFA curve increases (positive slope) when the proxy values consistently exceed their AR predictions, interpreted as a transgressive phase in the context of sequence stratigraphy, and decreases (negative slope) when values consistently fall below predictions, interpreted as a regressive phase. Inflection points in the INPEFA curve mark transitions between depositional regimes and may correspond to sequence boundaries, maximum flooding surfaces, or major palaeoenvironmental events.

S2.3 Detrending approach applied in this study

A single INPEFA product is presented for both Holes U1579D and U1514C. The HTHO series was detrended using a locally weighted scatterplot smoothing (LOWESS) function with a 35% bandwidth prior to PEFA computation. Subtraction of the LOWESS curve attenuates the bulk of the long-wavelength signal and enhances fourth-order (E405-scale) cyclicity. This parameterisation was selected after testing multiple methods that imply spectral attenuation (5%, 35%, linear detrend, demean detrend and original). The 35% LOWESS provided the clearest correspondence between INPEFA oscillations and previously identified E405 cycle positions, while avoiding over-smoothing that would suppress genuine depositional cyclicity at both holes. It should be noted that this selection criterion implies that the INPEFA curves are not fully independent of the cyclostratigraphic analysis; they are therefore presented as complementary depositional trend indicators consistent with the orbital framework, rather than as independent cross-checks.

S2.4 Interpretation framework

The INPEFA method was originally formulated for shallow-water siliciclastic settings (Nio *et al*., 2005; de Jong *et al*., 2007). Its application to deep-water pelagic carbonates requires adaptation of the interpretive framework: in this setting, HTHO variability primarily records orbital-scale terrigenous clay flux, so INPEFA inflection points are interpreted as changes in the terrigenous-to-carbonate depositional balance rather than as classical shallow-water sequence boundaries or maximum flooding surfaces *sensu stricto*.

Within a sequence stratigraphic framework, upward INPEFA trends in the HTHO series correspond to intervals of increasing clay-mineral content (higher Th concentrations), broadly consistent with enhanced terrigenous clay flux to the deep-water site (analogous to a transgressive-highstand phase in conventional sequence stratigraphy). Downward INPEFA trends reflect decreased clay input, consistent with reduced clay input and increased carbonate dilution (analogous to a lowstand or regressive phase). This interpretation is consistent with the theoretical basis of the INPEFA method (Nio *et al*., 2005) and with the comparison between the INPEFA curve and the Paleocene barystatic sea-level record of Miller *et al*. (2024).

The two-phase depositional structure identified at U1579D, a gradually decreasing INPEFA trend from the K-Pg boundary to ~330 m WMSF, followed by an abrupt shift at ~325 m WMSF into a heterogeneous plateau, broadly tracks the transition from the cooler, more stable middle Paleocene to the progressively warming and carbon-cycle-destabilised late Paleocene interval documented in global benthic isotope records (Zachos *et al*., 2001; Barnet *et al*., 2019). The abrupt inflection at ~325 m WMSF coincides with the prominent positive HTHO anomaly constrained to ~58.15 Ma ("*" event; Littler *et al*., 2014; Hollis *et al*., 2022), and the secondary positive inflection at ~300 m WMSF is broadly consistent with the Barnet *et al*. (2019) PETM event band in the tuned ATS.

At U1514C, the INPEFA curve shows a general decreasing trend from the K-Pg boundary at ~395 m WMSF to approximately ~340 m WMSF, reflecting an interval of relatively reduced terrigenous flux consistent with the early Paleocene carbonate recovery phase. The trend then reverses to a gentle rise

culminating in an abrupt positive inflection at approximately ~313 m WMSF, co-temporal with the anomaly identified as the "*" event, followed by a decreasing trend toward ~280 m WMSF and a secondary inflection consistent with the PETM event band. These trends broadly parallel those at U1579D, supporting a globally coherent depositional response to the major Paleocene carbon-cycle transitions. However, the INPEFA signal at U1514C is noisier and less clearly structured than at U1579D, consistent with the greater lithological heterogeneity and intermittent reworking at the Mentelle Basin hole.

S2.5 Software, packages, and reproducibility

All INPEFA analyses were performed in Python 3 (v.3.13.x) using a Jupyter Notebook environment. The implementation is adapted from the open-source PyNPEFA package (https://github.com/daeIy/PyNPEFA), with minor modifications to input handling and detrending options. The following packages are required: numpy (van der Walt *et al*., 2011), pandas (McKinney, 2010), scipy (Virtanen *et al*., 2020), matplotlib (Hunter, 2007), statsmodels (Seabold and Perktold, 2010), spectrum (Cokelaer, 2017), and cvxopt (Andersen *et al*., 2013). The full annotated notebook is available upon request from the corresponding author.

S2.6 Annotated Python script

The complete script is reproduced below for transparency and reproducibility. Path variables (diretorio, arquivo) are specific to the authors' local environment and must be adapted by the user. Well and file identifiers are omitted from the reproduced script; the depth window used for Hole U1579D (IODP Expedition 392) corresponds to approximately 265-440 m WMSF, while the depth window used for Hole U1514C (IODP Expedition 369) corresponds to approximately 255-410 m WMSF.

```
########### LIBRARY IMPORTS ###########
%matplotlib inline


import matplotlib.pyplot as plt
import numpy as np
import pandas as pd
from scipy import signal as sig
from cvxopt import matrix
from spectrum.burg import _arburg2
import statsmodels.api as sm


########### INPUT PARAMETERS ###########
filtersize_meter = 10       # Filter size in metres (prediction window).
Default = 10
diretorio = "./"            # Path to working directory — adapt to local
environment
arquivo = "[hole]_HTHO_[depth_range]_rsp0.1524.txt"  # Input filename —
adapt to local environment
```

```
dg = pd.read_table(diretorio + arquivo, sep="\s+", header=None)
header_profundidade = "DEPTH"   # Depth column label
header_GR = "HTHO"              # Proxy column label
dg.columns = [header_profundidade, header_GR]

########### FUNCTION DEFINITIONS ###########

def INPEFA(df, ordem):
    # Reorganise data into matrix format required by _arburg2
    dg = pd.DataFrame([np.array(df["HTHO"])], columns=[df["MD"]])
    y = dg.iloc[0]
    y = matrix(y)

    # Burg AR model: estimate prediction coefficients
    bffy = _arburg2(y, ordem)[0].real

    # PEFA: convolve series with prediction coefficients
    pffy = sig.convolve(y, np.reshape(bffy, (len(bffy), 1)), mode="same")

    # INPEFA: cumulative sum of PEFA (integrated bottom-up)
    iipfy = np.cumsum(pffy[::-1])[::-1]

    # Normalise to [-1, 1]
    ipfy = iipfy / max(abs(iipfy))

    # Depth alignment: shift by half the filter order
    ipfy = np.roll(ipfy, int(ordem / 2))
    return ipfy

def filtersize_sample(df, filtersize_meter):
    # Convert filter size from metres to number of samples
    first_row_value = df["MD"].iloc[0]
    last_row_value  = df["MD"].iloc[-1]
    amostragem = (last_row_value - first_row_value) / (len(df) - 1)
    ordem = int(filtersize_meter / amostragem)
    return ordem

# Prepare working DataFrame and compute filter size in samples
df = dg[[header_profundidade, header_GR]]
df = df.set_axis(["MD", "HTHO"], axis=1)
filtersize = filtersize_sample(df, filtersize_meter)

x        = np.array(df["MD"])      # Depth array
```

```
original = np.array(df["HTHO"])    # Raw HTHO series

# INPEFA from raw (undetrended) series
inpefa_original = INPEFA(df, filtersize)

########### MEAN DETREND ###########
coefficients  = np.polyfit(x, original, 0)          # Fit constant (mean)
media_model   = np.poly1d(coefficients)
media_trend   = media_model(x)
media_detrended = original - media_trend

dk = pd.DataFrame(data=media_detrended, columns=["HTHO"])
dk["MD"] = df["MD"]
inpefa_dmedia = INPEFA(dk, filtersize)

########### LINEAR DETREND ###########
coefficients   = np.polyfit(x, original, 1)          # Fit linear trend
linear_model   = np.poly1d(coefficients)
linear_trend   = linear_model(x)
linear_detrended = original - linear_trend

dk = pd.DataFrame(data=linear_detrended, columns=["HTHO"])
dk["MD"] = df["MD"]
inpefa_dlinear = INPEFA(dk, filtersize)

########### LOWESS 35% DETREND (primary approach) ###########
lowess = sm.nonparametric.lowess
lowess_trend     = lowess(original, x, frac=0.35, it=0)  # frac=0.35: 35%
bandwidth
lowess_detrended = original - lowess_trend[:, 1]

dl = pd.DataFrame(data=lowess_detrended, columns=["HTHO"])
dl["MD"] = df["MD"]
inpefa_dlowess_35pc = INPEFA(dl, filtersize)

########### LOWESS 5% DETREND ###########
lowess = sm.nonparametric.lowess
lowess_trend     = lowess(original, x, frac=0.05, it=0)  # frac=0.05: 5%
bandwidth
lowess_detrended = original - lowess_trend[:, 1]

dl = pd.DataFrame(data=lowess_detrended, columns=["HTHO"])
dl["MD"] = df["MD"]
inpefa_dlowess_5pc = INPEFA(dl, filtersize)
```

```
########### COMPOSITE FIGURE — ALL INPEFA VARIANTS ###########
plt.figure(figsize=(10, 4.5), facecolor="w", edgecolor="k")

plt.subplot(161)
plt.plot(original, -x, label="original")
plt.grid(True); plt.minorticks_on(); plt.legend()
plt.title("HTHO original")

plt.subplot(162)
plt.plot(inpefa_original, -x)
plt.grid(True); plt.minorticks_on()
plt.title("IPF original")

plt.subplot(163)
plt.plot(inpefa_dmedia, -x)
plt.grid(True); plt.minorticks_on()
plt.title("IPF dmedia")

plt.subplot(164)
plt.plot(inpefa_dlinear, -x)
plt.grid(True); plt.minorticks_on()
plt.title("IPF dlinear")

plt.subplot(165)
plt.plot(inpefa_dlowess_35pc, -x)
plt.grid(True); plt.minorticks_on()
plt.title("IPF dlowess 35%")

plt.subplot(166)
plt.plot(inpefa_dlowess_5pc, -x)
plt.grid(True); plt.minorticks_on()
plt.title("IPF dlowess 5%")

plt.subplots_adjust(wspace=0.5, hspace=0.5)

# Save figure — adapt filename to local environment
plt.savefig(diretorio + "[hole]_HTHO_[depth_range]_inpefa.pdf",
format="pdf")

# Export all INPEFA curves and raw series as text files
np.savetxt(diretorio + "HTHOR_original.txt",
           np.column_stack((x, original)), fmt="%.6f")
```

```
np.savetxt(diretorio + "IPF_original.txt",
           np.column_stack((x, inpefa_original)), fmt="%.6f")

np.savetxt(diretorio + "IPF_dmedia.txt",
           np.column_stack((x, inpefa_dmedia)), fmt="%.6f")

np.savetxt(diretorio + "IPF_dlinear.txt",
           np.column_stack((x, inpefa_dlinear)), fmt="%.6f")

np.savetxt(diretorio + "IPF_dlowess_35pc.txt",
           np.column_stack((x, inpefa_dlowess_35pc)), fmt="%.6f")

np.savetxt(diretorio + "IPF_dlowess_5pc.txt",
           np.column_stack((x, inpefa_dlowess_5pc)), fmt="%.6f")

plt.show()
```

REFERENCES

Andersen, M.S., Dahl, J., Liu, Z., Vandenberghe, L., 2013. Interior-point methods for large-scale cone programming. In: Optimization for Machine Learning. MIT Press.

Barnet, J.S., Littler, K., Westerhold, T., Kroon, D., Leng, M.J., Bailey, I., Zachos, J.C., 2019. A high-fidelity benthic stable isotope record of late Cretaceous–early Eocene climate change and carbon-cycling. Paleoceanography and Paleoclimatology, 34(4), 672–691.

Cokelaer, T., 2017. Spectrum: Spectral Analysis in Python. Journal of Open Source Software, 2(18), 348.

de Jong, M., Nio, S.D., Smith, D., Böhm, A.R., 2007. Subsurface correlation in the Upper Carboniferous (Westphalian) of the Anglo-Dutch Basin using the climate stratigraphic approach. First Break 25, 49-59.

Hollis, C.J., et al., 2022. The Paleocene–Eocene carbon isotope excursion in higher plant organic matter: differential fractionation of angiosperms and conifers in the New Zealand record. Geological Magazine, 159(7), 1024–1044.

Hunter, J.D., 2007. Matplotlib: A 2D graphics environment. Computing in Science & Engineering, 9(3), 90–95.

Littler, K., Röhl, U., Westerhold, T., Zachos, J.C., 2014. A high-resolution benthic stable-isotope record for the South Atlantic: Implications for orbital-scale changes in late Paleocene–early Eocene climate and carbon cycling. Earth and Planetary Science Letters, 401, 18–30.

Liu, Y., Li, H., Peng, P., Wu, M., Yan, N., Qin, X., Zhang, Y., 2024. High-resolution sequence stratigraphy research based on continuous wavelet transform and INPEFA: A case study in the Kalashayi Formation, Tarim Basin, China. Unconv. Resour. 4, 100099.

McKinney, W., 2010. Data structures for statistical computing in Python. Proceedings of the 9th Python in Science Conference, 445, 51–56.

Miller, K.G., Schmelz, W.J., Browning, J.V., Rosenthal, Y., Hess, A.V., Kopp, R.E., Wright, J.D., 2024. Global mean and relative sea-level changes over the past 66 Myr: implications for early Eocene ice sheets. Earth Sci. Syst. Soc. 3, 10091.

Nio, S.D., Brouwer, J., Smith, D.G., de Jong, M., Böhm, A., 2005. Spectral trend attribute analysis: applications in the stratigraphic analysis of wireline logs. First Break 23, 71-75.

Seabold, S., Perktold, J., 2010. Statsmodels: Econometric and statistical modeling with Python. Proceedings of the 9th Python in Science Conference, 57–61.

van der Walt, S., Colbert, S.C., Varoquaux, G., 2011. The NumPy array: a structure for efficient numerical computation. Computing in Science & Engineering, 13(2), 22–30.

Virtanen, P., et al., 2020. SciPy 1.0: fundamental algorithms for scientific computing in Python. Nature Methods, 17, 261–272.

Zachos, J., Pagani, M., Sloan, L., Thomas, E., Billups, K., 2001. Trends, rhythms, and aberrations in global climate 65 Ma to present. Science, 292(5517), 686–693.

Zulivandama, S.R., Razi, F., Taslim, J.N., Winardhi, I.S., 2018. Sequence analysis on carbonate formation using INPEFA approach. In: Proc. 43rd Annu. Sci. Meet. HAGI, Semarang.

Text S3. Detrending Method Evaluation: Comparison and Selection Rationale

S3.1 Overview

Five detrending approaches were evaluated for the HTHO log at both holes prior to cyclostratigraphic analysis: (i) undetrended (raw) signal; (ii) linear detrend; (iii) LOESS 25%; (iv) High-Pass Butterworth at 0.05 cycles/m; and (v) High-Pass Butterworth at 0.1 cycles/m. Figure S3 presents all five detrended series (panels A-E) for U1579D, and Figure S4 presents the corresponding series for U1514C, both superimposed on the raw signal (shown in grey), to allow direct visual comparison of their morphological characteristics. Method selection was based on a multi-criteria assessment comprising: (a) morphological evaluation of the detrended series; (b) comparison of MTM power spectra; and (c) COCO-derived SAR solutions. The primary analysis (main text, Figs. 3 and 4) uses the High-Pass Butterworth filter at 0.1 cycles/m (panel E of Figs. S3 and S4) as the preferred detrending method at both wells. The Butterworth high-pass filter was implemented with a cutoff at 0.1 cycles/m. The lower edge of the E405 band (~8.40 m at U1579D, ~7.19 m at U1514C, corresponding to ~0.119 and ~0.139 cycles/m, respectively) falls close to this cutoff, implying a modest attenuation of the lowest-frequency E405 energy; however, as shown in the EHA (Figs. 3G and 4G of the main text), the E405 band is robustly identified throughout both sections, and, in the case of Hole U1579D, clearly distinguishable from the adjacent signal regarded as Myr-scale modulation (Fig. S5G). Therefore, is understood that this edge-band attenuation should not affect the E405-kyr cycle count or the SAR estimates.

S3.2 Rationale for High-Pass 0.1 selection

The raw HTHO series at U1579D exhibits dominant spectral energy at multi-decametre wavelengths corresponding to million-year-scale eccentricity amplitude modulation. This long-period energy is clearly visible as a broad, smooth oscillation in the undetrended signal (Fig. S3A) and persists as a dominant spectral feature in both the linear detrend (Fig. S3B) and LOESS 25% (Fig. S3C) outputs. Under linear detrending, the million-year-scale energy cannot be adequately removed, and its residual presence in the detrended series contaminates the orbital band, generating spurious COCO SAR solutions of 4-18 cm/kyr through spectral frequency overlap (see also Fig. S4 and the extended discussion in Text S4). Similarly, the LOESS 25% filter does not suppress energy at periods substantially longer than the bandwidth window length, leaving residual million-year variance that affects spectral interpretation.

The High-Pass Butterworth filter at 0.05 cycles/m (Fig. S3D) removes more of this long-period energy, but the relatively gentle spectral roll-off at this cutoff allows partial contamination from the Myr-scale cycles to persist into the orbital band. The High-Pass Butterworth at 0.1 cycles/m (Fig. S3E) provides a steeper cutoff that cleanly suppresses all energy below this frequency while preserving the E405 signal band (~0.12-0.24 cycles/m) and shorter orbital periodicities. Although High-Pass filtering is not the most conventional detrending method in cyclostratigraphy, its use is justified by the demonstrated spectral characteristics of this record, following the principle that pre-spectral removal of non-orbital variance improves orbital frequency detection (Meyers, 2012; Hinnov, 2013, 2018; Li *et al*., 2019).

At U1514C, the case for High-Pass 0.1 filtering is even stronger than at U1579D. Under linear detrending, the EHA at U1514C shows a continuous merger of the million-year energy with the E405 band (Supplementary Fig. S6G), making E405 identification impossible without prior high-pass filtering. The High-Pass 0.1-filtered EHA at U1514C (Fig. 4G of the main text) shows the E405 band more clearly defined and persistent throughout the section, supporting the argument that the filter successfully isolates the orbital band at this hole as well. The High-Pass 0.1 filter is therefore adopted as the primary detrending approach throughout this study.

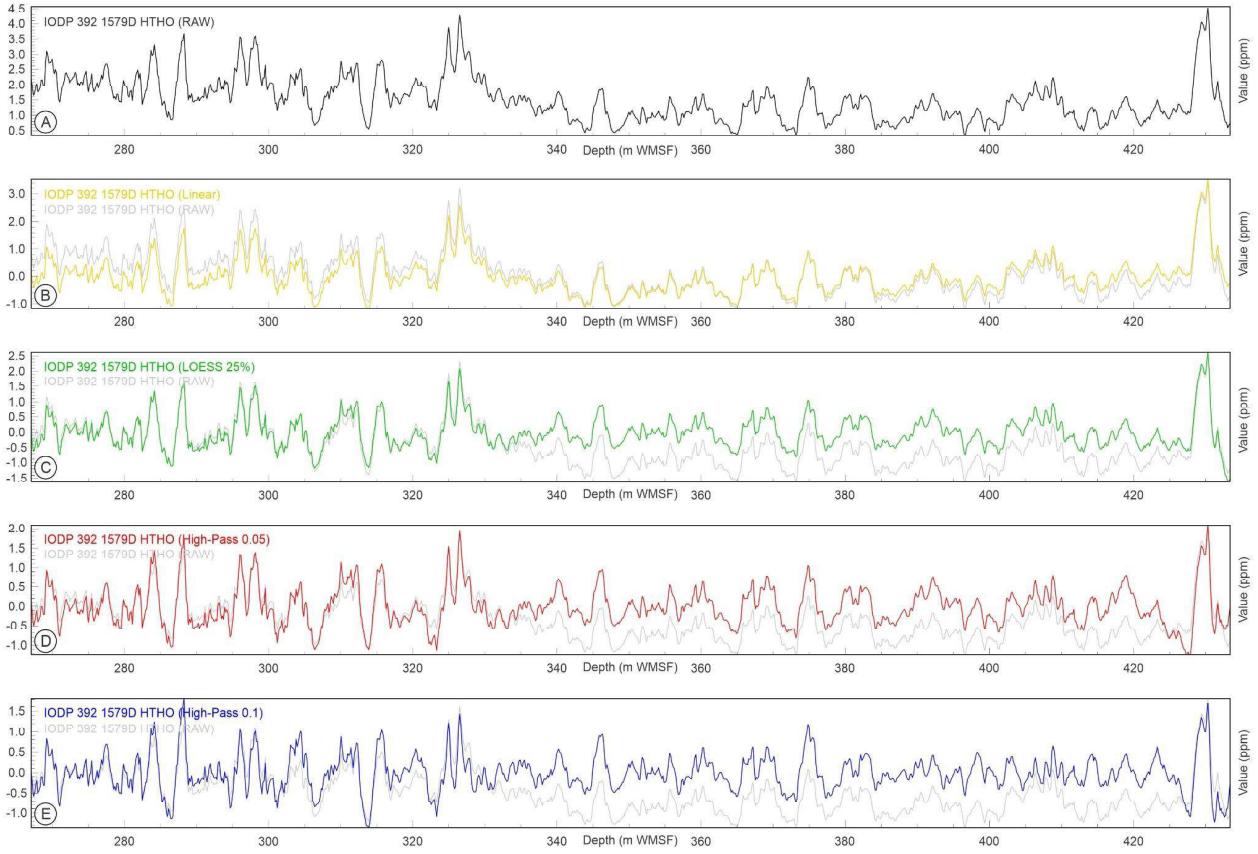


Figure S3: Comparison of detrending methods applied to the HTHO log at Hole U1579D (IODP Expedition 392). (A) Raw (undetrended) signal. (B) Linear detrend. (C) LOESS 25%. (D) High-Pass Butterworth at 0.05 cycles/m. (E) High-Pass Butterworth at 0.1 cycles/m. The raw signal is shown in grey for reference in panels B-E. The High-Pass 0.1 detrend (panel E) is adopted as the primary approach in this study, as it cleanly suppresses the dominant million-year-scale eccentricity modulation energy visible in panels A-C while preserving the E405 signal band and shorter orbital periodicities.

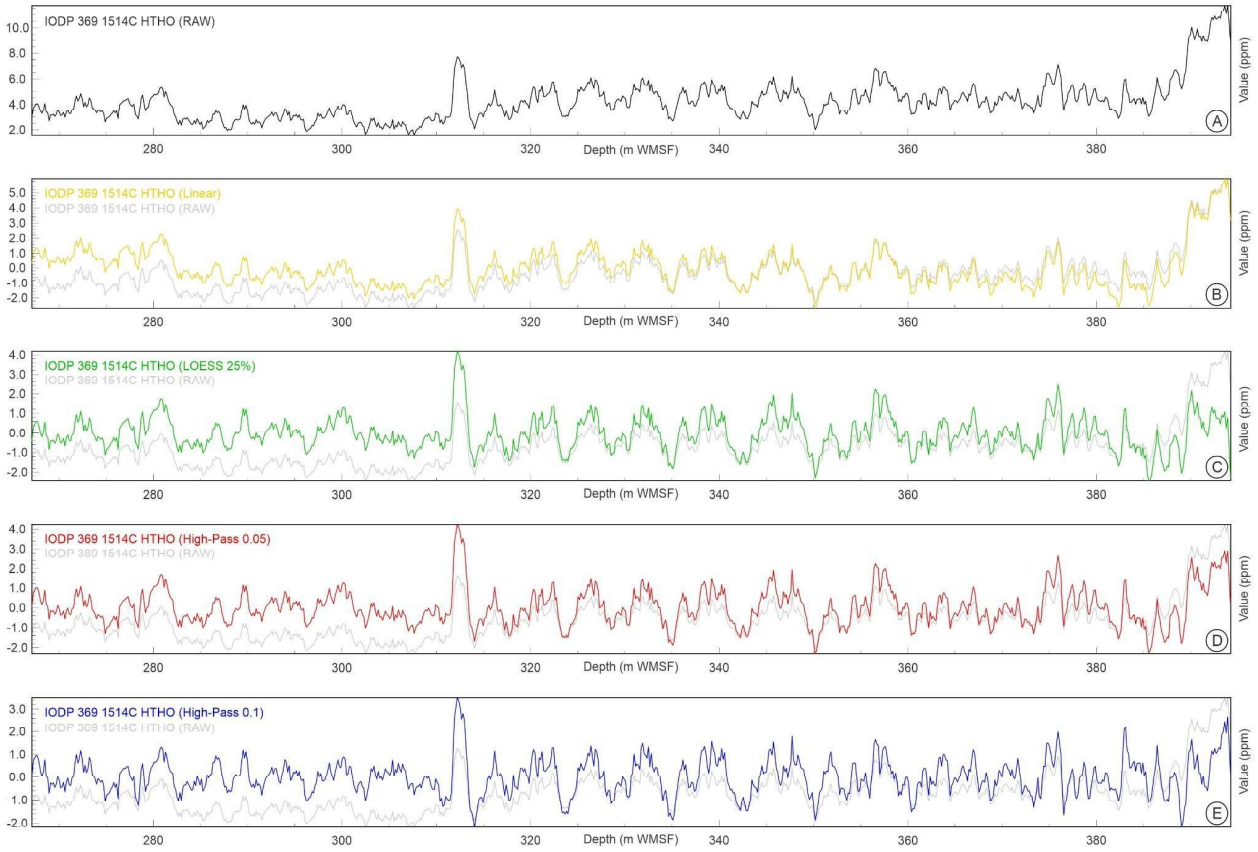


Figure S4: Comparison of detrending methods applied to the HTHO log at Hole U1514C (IODP Expedition 369). Panels as in Fig. S3. Note the higher raw HTHO values (~2-10 ppm) relative to U1579D (~0.5-4 ppm), reflecting the greater clay content of the Clayey Nannofossil Chalk facies at this well. The High-Pass 0.1 detrend (panel E) effectively isolates the orbital band and is the primary detrending approach applied at U1514C throughout this study. The prominent positive HTHO spike at ~313 m WMSF, visible in all detrended series, corresponds to the "*" event anomaly constrained to ~58.15 Ma.

REFERENCES

Hinnov, L.A., 2013. Cyclostratigraphy and its revolutionizing applications in the earth and planetary sciences. Geological Society of America Bulletin, 125(11–12), 1703–1734.

Hinnov, L.A., 2018. Cyclostratigraphy and astrochronology in 2018. In: Stratigraphy & Timescales, Vol. 3, pp. 1–80. Academic Press.

Li, M., Hinnov, L., Kump, L., 2019. Acycle: Time-series analysis software for paleoclimate research and education. Computers & Geosciences, 127, 12–22.

Meyers, S.R., 2012. Seeing red in cyclic stratigraphy: spectral noise estimation for astrochronology. Paleoceanography 27, PA3228.

Text S4. Linear Detrend Cyclostratigraphic Analyses: Methodology and Interpretation

S4.1 Overview

Figure S5 and S6 present the full cyclostratigraphic analysis of the HTHO series from Holes U1579D and U1514C, respectively, under linear detrending. This figures serves two purposes: (1) they document the spectral and SAR characteristics of the raw minus linear-trend signal for reference and comparison; and (2) they provide the primary methodological justification for the adoption of the High-Pass Butterworth filter as the preferred detrending approach. The linear detrend results are not used for orbital identification or ATS construction; they are retained as supplementary material to ensure methodological transparency.

S4.2 Linear detrending procedure

Linear detrending was performed by fitting a least-squares regression line to the full HTHO depth series over the studied interval (K-Pg to PETM interval, ~265-440 m WMSF-U1579D and ~255-410 m WMSF-U1514C) and subtracting the fitted trend from the observed values. This removes a first-order increase or decrease in HTHO with depth but leaves all shorter-wavelength variability intact, including any multi-decametre (million-year-scale) energy present in the signal. The detrended series was then analysed using the same MTM, EHA, and COCO/eCOCO procedures applied to the High-Pass 0.1-filtered series.

S4.3 Figure organisation

Figure S5 shows the results of the cyclostratigraphic analysis carried out on the HTHO data from U1579D using linear detrending; Figure S6 shows the corresponding analysis for U1514C. It follows the same panel layout as that used in the main analysis, with the exception of Panel C (Fig. 3 of the main text), with panels organised as follows: (A) HTHO/HFK ratio; (B) INPEFA with LOWESS 35% detrend applied to the RAW HTHO data; (C) Gaussian-filtered million-year modulation bands, isolating the long-period energy that dominates this detrend; (D) Gaussian-filtered E405-kyr signal; (E) linearly detrended HTHO; (F) MTM spectral analysis with confidence levels and F-test results; (G) EHA showing the spectral energy distribution

along the depth axis; (H) COCO null hypothesis; (I) COCO correlation coefficient and number of contributing orbital parameters; (J) Ecoco.

S4.4 Interpretation: U1579D

Under linear detrending at U1579D, the MTM power spectrum (Fig. S5F) is dominated by spectral peaks at multi-decametre wavelengths (~49-13 m), exceeding the 99% confidence level. These correspond to what was interpreted as Myr-scale eccentricity amplitude modulation cycles, whose filtered expression is shown in panel C. The Gaussian-filtered signal in panel C shows a smooth, long-wavelength oscillation with amplitude ~1-2 frequency units that tracks the bulk variation in HTHO along the section, demonstrating visually the energy that must be suppressed before orbital analysis.

In the EHA (Fig. S5G), the E405 band is visible but its energy merges at lower frequencies with the million-year signals, creating an ambiguous spectral landscape in which COCO identifies spurious SAR solutions of 4-18 cm/kyr (Fig. S5H-J). These artefacts arise because the COCO algorithm achieves high correlations with the La2004 orbital target by identifying the million-year energy as E405 and reinterpreting the true E405 signal as a shorter-period cycle. Although this frequency overlaping problem is less severe at U1579D than would be observed in more lithologically heterogeneous settings, the Myr-scale cycle envelope still introduces enough low-frequency variance to render reliable E405 identification and COCO-based SAR estimation impossible without prior High-Pass filtering. The High-Pass 0.1 filter mitigates this issue (see Text S3 and Fig. S3).

S4.5 Interpretation: U1514C

Under linear detrending at U1514C, the MTM power spectrum (Fig. S6F) is dominated by spectral peaks at multi-decametre wavelengths (~43-13 m), exceeding the 95% confidence level. These correspond to the million-year-scale eccentricity amplitude modulation cycles, whose filtered Gaussian expression is shown in panel C of Fig. S6. The key distinction from U1579D is that at U1514C, the EHA under linear detrending (Fig. S6G) shows what was interpreted as an apparently continuous merger of the million-year spectral energy into the E405 band, not merely a partial overlap as at U1579D, but a complete spectral continuum from ~0.02 to at least ~0.2 cycles/m that renders independent E405 identification impossible. This is the primary methodological justification for the High-Pass 0.1 pre-processing at U1514C: the frequency overlap problem is not a matter of degree but of observability. COCO analyses under linear detrending at U1514C accordingly return spurious SAR solutions of 4-18 cm/kyr across the tested range (Fig. S6H-J), analogous to U1579D but more severe. Following High-Pass 0.1 filtering, the E405 band is cleanly resolved and SAR solutions converge on geologically consistent values of ~1.0-1.8 cm/kyr (see Text S5 and Fig. S8).

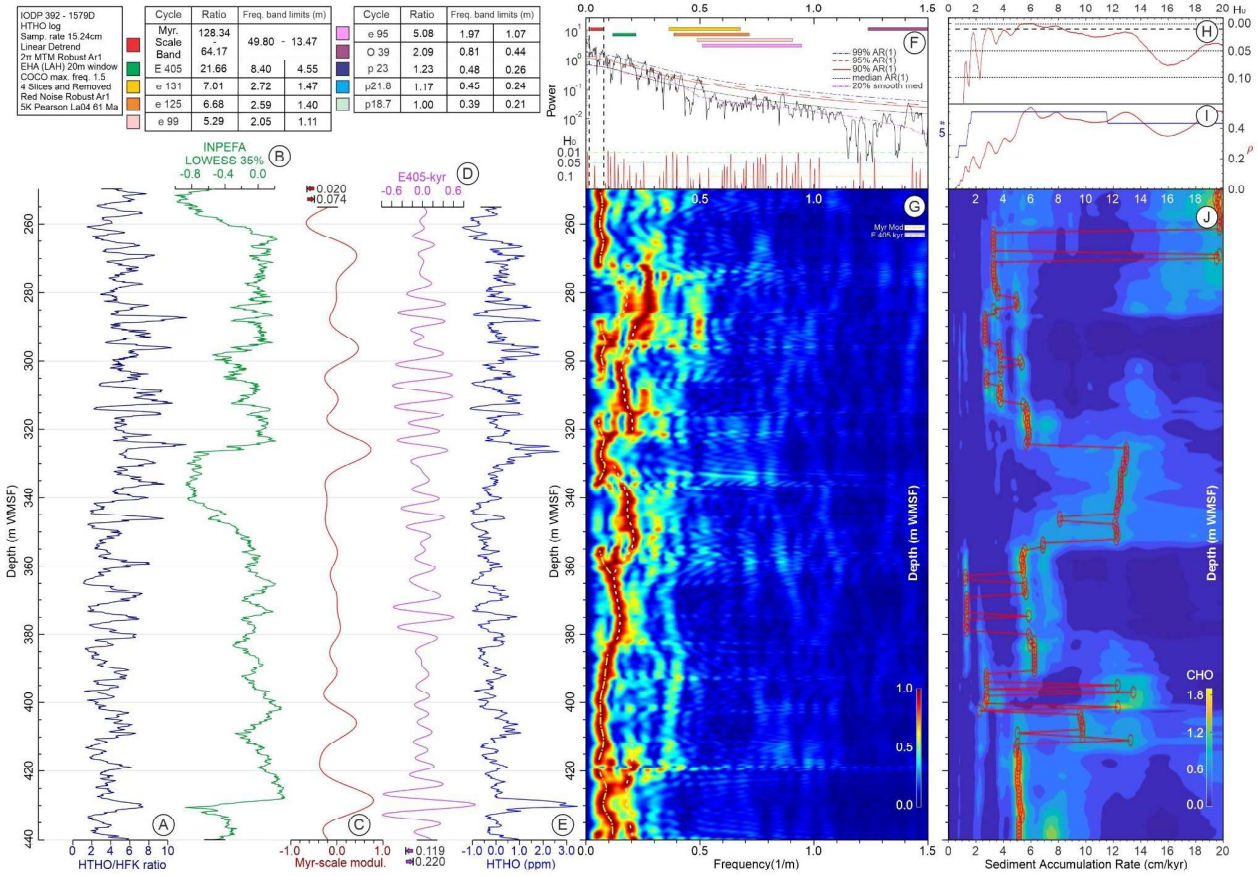


Figure S5: Cyclostratigraphic analysis for Hole U1579D under linear detrending, illustrating the dominance of million-year-scale energy and its partial merger with the E405 band in the EHA. (A) HTHO/HFK ratio; (B) INPEFA with LOWESS 35%; (C) Gaussian-filtered Myr-scale modulation bands, showing the long-period energy that dominates the spectrum under linear detrending; (D) Gaussian-filtered E405-kyr signal; (E) linearly detrended HTHO; (F) MTM spectral analysis with confidence levels and F-test results, note the dominance of low-frequency (multi-decametre) peaks; (G) EHA showing the partial merger of million-year and E405 energy at low frequencies; (H) COCO null hypothesis; (I) COCO ρ and number of contributing orbital parameters, showing spurious high-SAR solutions generated by spectral frequency overlap; (J) eCOCO. These artefacts constitute the primary methodological justification for the High-Pass 0.1 pre-processing approach adopted in this study (see Text S3 and Fig. S3).

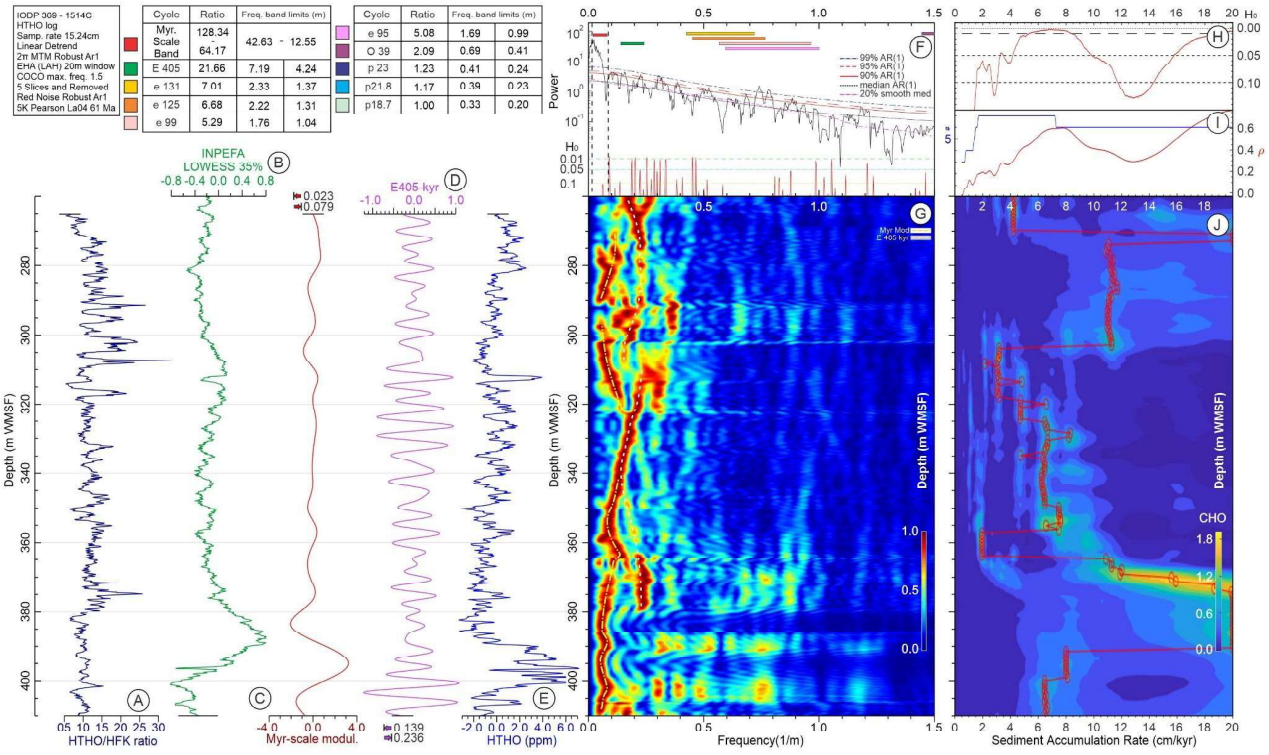


Figure S6: Cyclostratigraphic analysis for Hole U1514C under linear detrending, showing the complete merger of million-year-scale energy with the E405 band in the EHA (panel G). Panels as in Fig. S5. At U1514C, the merger of the myr-scale modulation energy (panel C) with the E405 band in the EHA is continuous and complete, in contrast to the partial overlap at U1579D (Fig. S5G), making reliable E405 identification impossible without prior high-pass filtering. COCO analyses return spurious SAR solutions of 4-18 cm/kyr (panels H-J), as at U1579D, but the spectral frequency overlap is more severe. These features constitute the primary justification for the High-Pass 0.1 pre-processing at U1514C.

REFERENCES

Laskar, J., Robutel, P., Joutel, F., Gastineau, M., Correia, A.C., Levrard, B., 2004. A long-term numerical solution for the insolation quantities of the Earth. Astronomy & Astrophysics, 428, 261–285.

Text S5: Expanded SAR Estimation: COCO, eCOCO, and TimeOpt Results

S5.1 Overview

Figures S7 and S8 present the expanded sediment accumulation rate (SAR) estimation results for Holes U1579D and U1514C, respectively, using up to seven orbital parameters and three independent methods: the Correlation Coefficient (COCO), the Evolutionary Correlation Coefficient (eCOCO), and TimeOpt. These figures complement the primary cyclostratigraphic analysis (Figs. 3 and 4 of the main text) by showing the full SAR range tested and the convergence of the three methods on a consistent, geologically plausible solution.

S5.2 Methods

S5.2.1 COCO and eCOCO

The COCO method (Li *et al*., 2019a) quantifies the correlation between the power spectrum of the depth-domain proxy series and the power spectrum of the La2004 orbital solution (Laskar *et al*., 2004) evaluated at a given SAR hypothesis. For each candidate SAR, the depth series is rescaled to time using that SAR, and the resulting time-domain power spectrum is compared to the La2004 target. The SAR value that maximises this correlation (rho) whilst rejecting the null hypothesis (H0) at $p < 0.05$ is reported as the COCO-supported estimate. The eCOCO extension applies the same procedure within a sliding depth window to resolve temporal changes in SAR along the section. Both analyses were performed with 5000 Monte Carlo simulations, robust AR1 red-noise modelling, a maximum frequency of 1.5 cycles/kyr, and 4 slices for the U1579D eCOCO and 5 slices for the U1514C. The La2004 solution was evaluated at 61 Ma, corresponding to the mean age of the studied interval.

S5.2.2 TimeOpt

TimeOpt (Meyers, 2015) searches for the SAR that simultaneously optimises two criteria: (1) the fit of the envelope of the bandpass-filtered signal to the La2004 E405 amplitude modulation envelope (r^2_envelope); and (2) the fit of the power spectrum to the full set of orbital periodicities (r^2_power). The combined optimality criterion $r^2_opt = r^2_envelope \times r^2_power$ is maximised at the best-fit SAR. TimeOpt was applied using the La2004 solution at 61 Ma, with the E405 bandpass filter defined by the band limits identified in the MTM analysis.

S5.3 Figure organisation

Figures S7 and S8 contain twelve panels: (A) TimeOpt r^2_opt curve versus SAR, showing the peak at the optimal SAR; (B) r^2_envelope versus r^2_power cross-plot; (C) reconstructed E405 envelope (from TimeOpt) compared to the La2004 E405 amplitude model; (D-F) COCO results: null hypothesis significance

level, rho, and number of contributing orbital parameters versus SAR, over the extended SAR range; (G-I) same three COCO panels over the primary SAR range (0.5-5.0 cm/kyr); (J) eCOCO rho along the depth axis; (K) eCOCO null hypothesis significance level; (L) number of contributing orbital parameters from eCOCO.

S5.4 Results: U1579D

At U1579D, TimeOpt identifies a primary r^2_opt peak at ~2.12 cm/kyr (Fig. S7A), with a secondary shoulder near ~1.7 cm/kyr that falls within the COCO-supported range. COCO rejects H0 at $p < 0.05$ for SARs between approximately 1.1 and 1.9 cm/kyr (Figs. S7D-I), with the rho maximum concentrated at ~1.3-1.6 cm/kyr and around 5 contributing orbital parameters at the optimal SAR. The eCOCO (Figs. S7J-L) shows that the COCO-supported SAR range is broadly stable along the section, with slight upward variation toward the top of the Paleocene consistent with the progressive thinning of E405 cycles documented in the wavelet analysis (Fig. S9). The combined multi-method estimate for U1579D is ~1.1-2.1 cm/kyr, with a primary concentration at ~1.5-1.9 cm/kyr. The TimeOpt peak at ~2.12 cm/kyr likely reflects a locally higher SAR in the upper Paleocene interval that carries more spectral weight in the global TimeOpt optimisation.

S5.5 Results: U1514C

At U1514C, TimeOpt identifies a primary r^2_opt peak at ~1.62 cm/kyr (Fig. S8A), with a secondary shoulder near ~1.3 cm/kyr that falls within the COCO-supported range. COCO rejects H_0 at $p < 0.05$ for SARs between approximately 1.0 and 1.8 cm/kyr (Figs. S8D-I), with the rho maximum concentrated at ~1.2-1.5 cm/kyr and up to 5 contributing orbital parameters at the optimal SAR. The eCOCO (Figs. S8J-L) shows notable lateral variability in the supported SAR range along the U1514C section, consistent with the more complex depositional history at this hole: the upper portion of the section (~265-360 m WMSF) shows a more stable COCO-supported range, while the lower portion (~360-405 m WMSF) exhibits broader H_0 rejection boundaries, reflecting the possibly higher lithological heterogeneity and reduced E405 signal continuity in this interval (see Supplementary Text S6 and Fig. S10). The combined multi-method estimate for U1514C is ~1.0-1.8 cm/kyr, consistent with the expedition proceedings estimate of ~1.4 cm/kyr (Huber *et al.*, 2019).

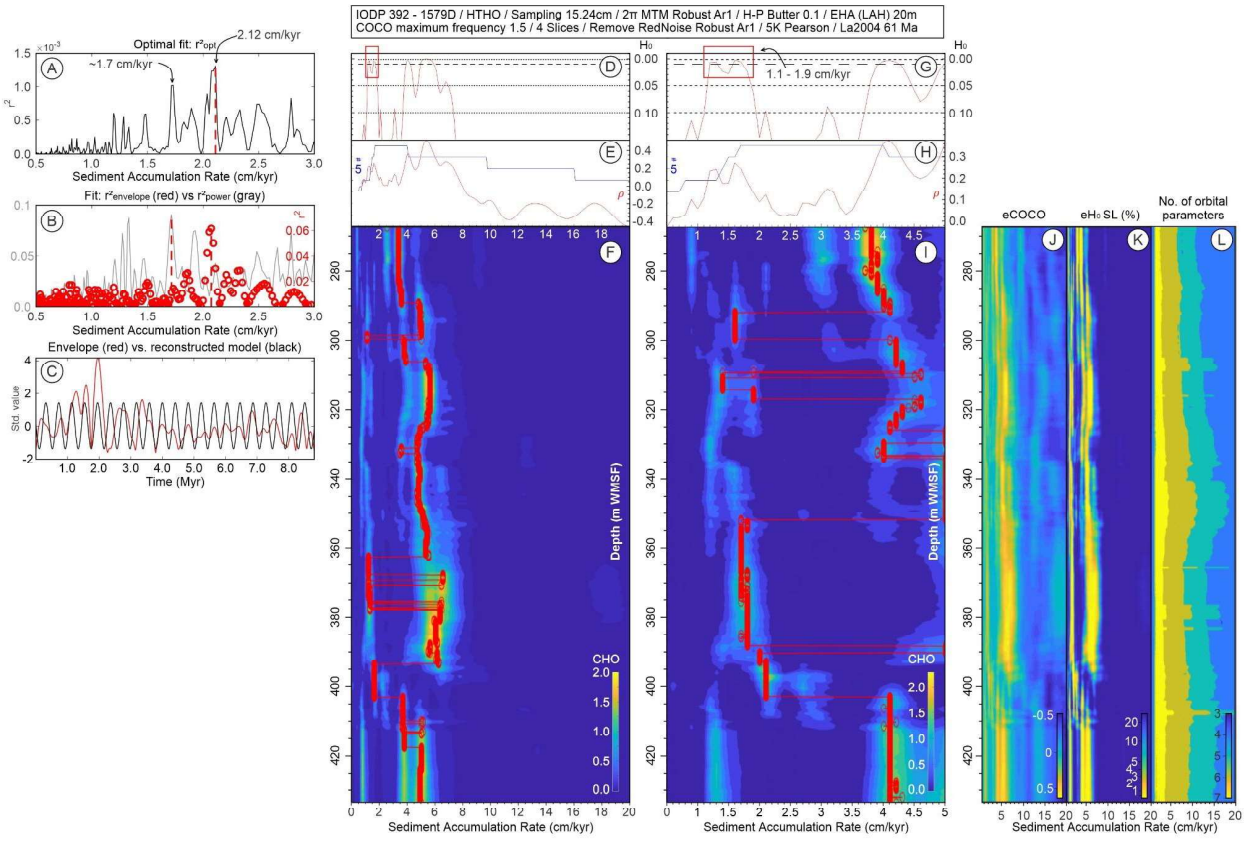


Figure S7: Expanded SAR testing for Hole U1579D (IODP Expedition 392, Hole U1579D; High-Pass Butterworth 0.1 detrend), showing COCO, eCOCO, and TimeOpt results over extended and primary SAR ranges. (A) TimeOpt optimal r² versus SAR, with primary peak at ~2.12 cm/kyr; (B) r²_envelope vs. r²_power cross-plot; (C) reconstructed E405 envelope (red) compared to La2004 model (black); (D-F) COCO null hypothesis, rho, and number of orbital parameters over extended SAR range (0-20 cm/kyr); (G-I) same COCO panels over primary SAR range (0.5-5.0 cm/kyr), with H_0 rejection range of ~1.1-1.9 cm/kyr highlighted; (J) eCOCO rho along depth axis; (K) eCOCO eH_0 significance level; (L) number of contributing orbital parameters from eCOCO. The convergence of the three methods on ~1.1-2.1 cm/kyr (primary concentration ~1.5-1.9 cm/kyr) confirms the geological consistency of the SAR estimate at this hole.

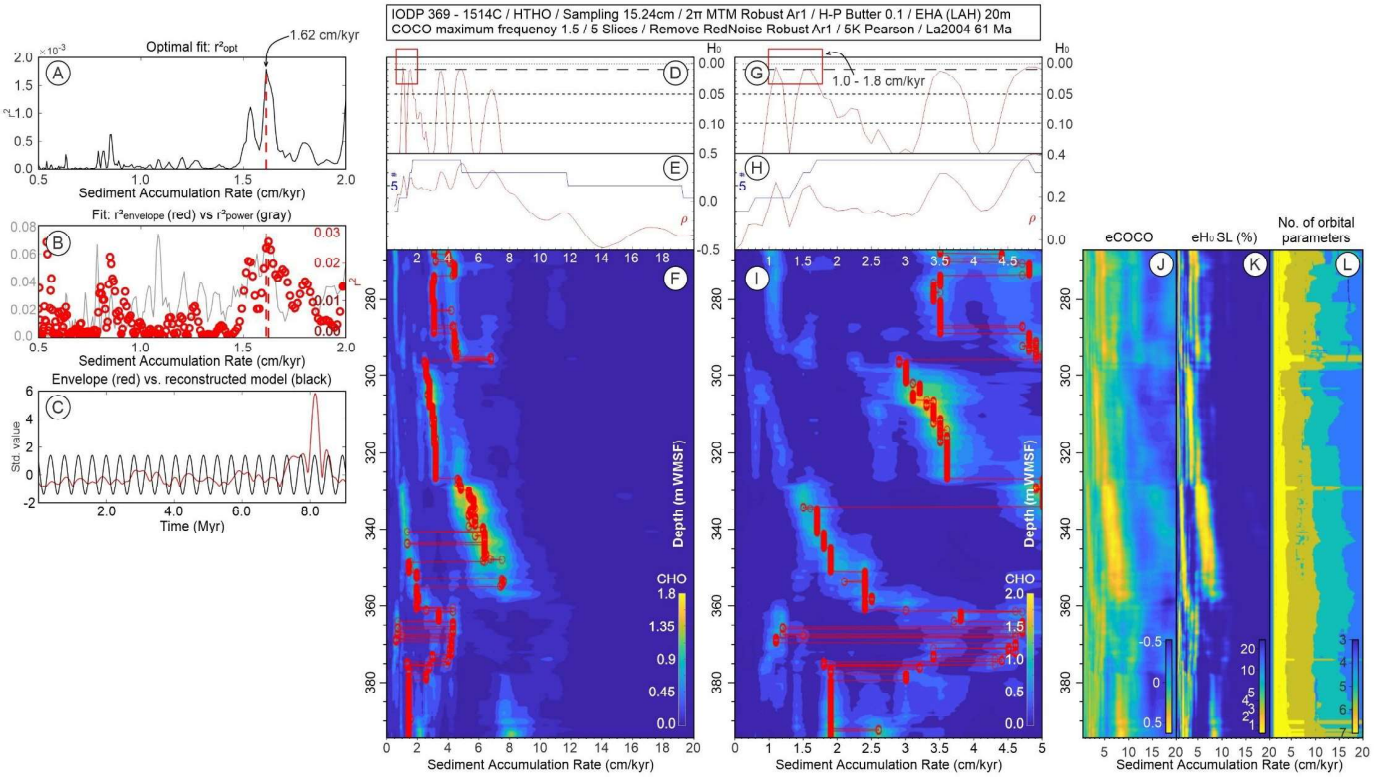


Figure S8: Expanded SAR testing for Hole U1514C (IODP Expedition 369, Hole U1514C; High-Pass Butterworth 0.1 detrend), showing COCO, eCOCO, and TimeOpt results over extended and primary SAR ranges. Panels as in Fig. S7. (A) TimeOpt optimal r^2 versus SAR, with primary peak at ~1.62 cm/kyr; (B-C) fit panels; (D-F) COCO null hypothesis, rho, and number of orbital parameters over extended SAR range (0-20 cm/kyr); (G-I) same COCO panels over primary SAR range (0.5-5.0 cm/kyr), with H_0 rejection range of ~1.0-1.8 cm/kyr highlighted; (J) eCOCO rho along depth axis; (K) eCOCO eH_0 significance level; (L) number of contributing orbital parameters from eCOCO. The eCOCO (panel J) shows greater lateral variability in the supported SAR range along the U1514C section compared to U1579D (Fig. S7J), consistent with the more complex depositional history and lithological heterogeneity at the Mentelle Basin well.

REFERENCES

Huber, B. T., Hobbs, R. W., Bogus, K. A., Batenburg, S. J., Brumsack, H. J., do Monte Guerra, R., ... & Xu, Z., 2019. Expedition 369 summary. Proceedings of the International Ocean Discovery Program, 369, 101.

Laskar, J., Robutel, P., Joutel, F., Gastineau, M., Correia, A.C., Levrard, B., 2004. A long-term numerical solution for the insolation quantities of the Earth. Astron. Astrophys. 428, 261-285.

Li, M., Hinnov, L., Kump, L., 2019. Acycle: Time-series analysis software for paleoclimate research and education. Comput. Geosci. 127, 12-22.

Meyers, S.R., 2015. The evaluation of eccentricity-related amplitude modulation and bundling in paleoclimate data: an inverse approach for astrochronologic testing and time scale optimization. Paleoceanography 30, 1625-1640.

Text S6: Wavelet Transform Analysis: Methodology and Interpretation

S6.1 Methodological background

Extended wavelet analysis was applied to the High-Pass 0.1-filtered and raw HTHO series from both Holes U1579D and U1514C to provide a time-frequency representation of spectral power that complements the global MTM spectral analysis. Whereas MTM provides a single, globally averaged power spectrum for the entire series, wavelet analysis resolves how spectral power at each frequency (or period) evolves along the stratigraphic depth axis, making it particularly sensitive to non-stationary signals and gradual changes in sedimentation rate.

S6.2 Wavelet transform implementation

The continuous wavelet transform (CWT) was computed using the Morlet mother wavelet, which provides an optimal balance between time (depth) and frequency localisation for quasi-periodic geological signals (Torrence and Compo, 1998; Weedon, 2003). The Morlet wavelet is defined as:

$$\psi(\eta) = \pi^{(-1/4)} \cdot \exp(i\omega_0\eta) \cdot \exp(-\eta^2/2)$$

where ω_0 is the non-dimensional frequency (set to 6, the standard value for the Morlet wavelet, which ensures at least one full oscillation within the wavelet envelope), and η is the non-dimensional time parameter. The angular frequency $\omega_0 = 6$ satisfies the admissibility condition and provides good frequency resolution at orbital periodicities relevant to this study.

The CWT was computed using the Acycle software (Li *et al*., 2019), which implements the wavelet algorithm of Torrence and Compo (1998) adapted for depth-domain stratigraphic series. The input series were interpolated to a uniform sampling interval of 0.1524 m prior to transformation. The wavelet power spectrum W(s, n) at scale s and depth position n is defined as:

$$W(s, n) = |CWT(s, n)|^2$$

where |·| denotes the modulus of the complex wavelet coefficient. The global wavelet power spectrum is obtained by averaging W(s, n) over all depth positions n. The 95% significance level against a red-noise background is estimated following the method of Torrence and Compo (1998), using an AR(1) coefficient estimated from the input series.

S6.3 Outputs and figure organisation

Figures S9 and S10 present wavelet analyses of the High-Pass 0.1-filtered HTHO series (panels A-B) and the raw HTHO series (panels C-D) for Holes U1579D and U1514C, respectively. Each panel pair contains: (A/C) Period-domain wavelet power spectrum (colour-coded power as a function of depth and period in metres, log scale); and (B/D) Frequency-domain wavelet power spectrum (same information but with the y-axis expressed as frequency in cycles/m). For each, the 95% significance contour is overlain as a solid curve, and the cone of influence (COI), within which edge effects reduce reliability, is shown as a shaded region.

S6.4 Interpretation of the wavelet results for U1579D

Fig S9A-B shows that the E405 signal (central period ~4-7 m; central frequency ~0.15-0.24 cycles/m) is expressed as a near-continuous band of elevated wavelet power from ~260 m to ~430 m WMSF, exceeding the 95% significance level throughout most of the section. The power in this band is broadly consistent with the multi-method SAR estimates of ~1.1-2.1 cm/kyr.

In the lowermost interval (~385-433 m WMSF), the raw and lightly detrended records show three broad high-amplitude packages spaced ~10-12 m apart. These are not individual E405 cycles; they represent amplitude envelopes of the million-year-scale eccentricity modulation. The biostratigraphic constraints at this depth (B *Cruciplacolithus primus* at 431.42 m / 65.77 Ma and B *Chiasmolithus danicus* at 420.25 m / 64.53 Ma) restrict the local SAR to ~0.9 cm/kyr, which predicts E405 cycle thicknesses of ~3.6 m, incompatible with a ~10-12 m E405 interpretation. After High-Pass 0.1 filtering, the million-year modulation envelope is suppressed and the shorter internal E405 cycles of ~3-5 m become the dominant wavelet expression in this interval. A secondary band of intermittent elevated power near ~1.4 cycles/m corresponds to the tentative obliquity signal identified in the MTM analysis (main text).

In the raw (unfiltered) HTHO series (Fig S9C-D), U1579D exhibits dominant wavelet power at very long periods (>8 m), corresponding to the myr-scale eccentricity modulation cycles identified in the MTM analysis. This long-period energy is expressed as a broad, high-amplitude band occupying the lowest-frequency portion of the wavelet spectrum, and is present throughout the full depth range. Its dominance in the raw record, relative to the E405 band, demonstrates visually the necessity of the High-Pass 0.1 pre-filtering step: without filtering, the million-year-scale energy would obscure the E405 signal in any spectral analysis. At U1579D, the long-period energy and the E405 band remain visually separable in the raw wavelet, consistent

with the observation that the frequency overlap problem, while present, is less severe here than in more lithologically heterogeneous settings.

S6.5 Interpretation of the wavelet results for U1514C

At U1514C, the filtered wavelet spectrum shows the E405 signal expressed as an elevated power band from ~265 to ~405 m WMSF, but with notably greater spatial variability than at U1579D (Fig. S10A-B). In the upper portion of the section (~265-360 m WMSF), more clearly defined cycles of ~4-6 m exceed the 95% significance level intermittently, consistent with the multi-method SAR estimates of ~1.0-1.8 cm/kyr. A gradual upward thinning of cycles toward ~4 m near the top of the section is consistent with a possible decrease in sediment accumulation rate from the lower to upper Paleocene at this hole, possibly reflecting progressive changes in carbonate preservation during Paleocene warming. In the lower portion (~360-405 m WMSF), cycle thicknesses are irregular and the E405 band shows reduced and discontinuous power. This pattern reflects the combined effects of higher lithological heterogeneity, lower signal-to-noise ratio, and residual contamination from long-period myr-scale energy in this interval, and is not interpreted as a meaningful change in the E405 cycle structure. Caution is therefore advised when interpreting the wavelet pattern in U1514C.

In the raw (unfiltered) HTHO series at U1514C, the wavelet spectrum is dominated by long-period energy at >8 m, corresponding to the myr-scale eccentricity modulation cycles (Fig. S10C-D). The raw HTHO values at U1514C are substantially higher than at U1579D (~2-10 ppm versus ~0.5-4 ppm), reflecting the greater clay content of the Clayey Nannofossil Chalk facies. The long-period energy in the raw wavelet spectrum is both higher in absolute power and more spectrally diffuse at U1514C than at U1579D, consistent with the greater non-orbital lithological variability at the Mentelle Basin hole. This diffuse long-period energy is the primary source of the continuous EHA spectral merger observed under linear detrending (Supplementary Fig. S6G) and further confirms the necessity of High-Pass 0.1 pre-filtering for reliable orbital analysis at U1514C.

S6.6 Limitations

The wavelet approach is subject to two main limitations in this context. First, the cone of influence (COI) reduces the interpretable depth range near the top and bottom of each series by a distance approximately equal to one half-wavelength of the period of interest (Torrence and Compo, 1998). For E405-scale signals (~6-8 m period), this corresponds to an edge-affected zone of ~3-4 m at each end of the series, which is negligible relative to the total series length (~165 m at U1579D). Second, the wavelet power at any given depth position represents an average over a depth window of approximately one wavelength, so features shorter than one E405 cycle (~6-8 m) cannot be resolved as depth-specific events. The INPEFA method, which operates in depth space without spectral averaging, is therefore better suited to identifying abrupt depositional events such as the anomaly at ~325 m WMSF.

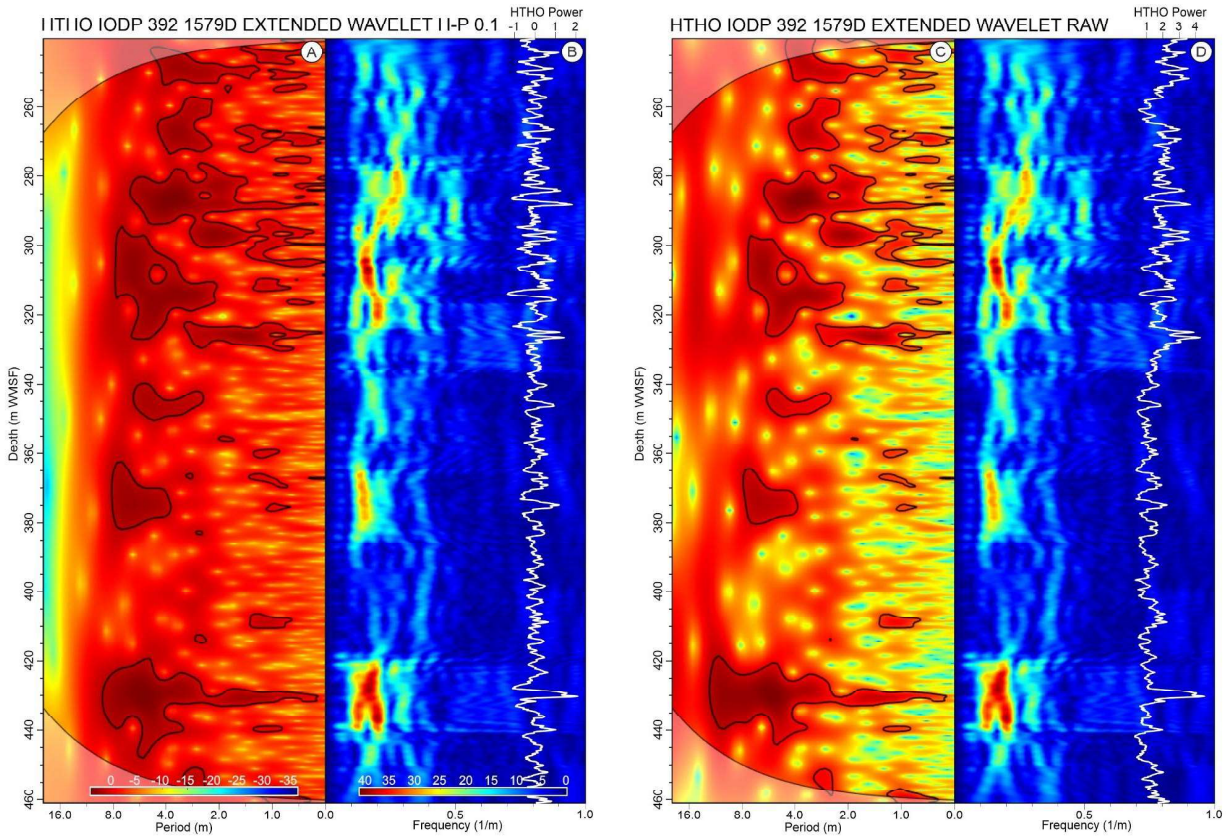


Figure S9: Extended wavelet analysis of HTHO at Hole U1579D (IODP Expedition 392). (A-B) High-Pass 0.1 filtered series: period-domain (A) and frequency-domain (B) representations. (C-D) Raw (unfiltered) HTHO series: period-domain (C) and frequency-domain (D) representations. In the period-domain scalograms (A, C), colour represents wavelet power on a logarithmic scale, with warm colours (red-brown) indicating high spectral power at a given period-depth combination and cool colours (blue) indicating low power. In the frequency-domain panels (B, D), colour likewise represents spectral power as a function of frequency and depth. The 95% significance contour is overlain as a solid black curve; the cone of influence is shown as a shaded region. In the filtered record (A-B), the E405 signal is expressed as a near-continuous band of elevated power from ~260 to ~430 m WMSF. In the raw record (C-D), dominant power at very long periods (>8 m) reflects the million-year-scale eccentricity modulation that necessitates High-Pass 0.1 pre-filtering for reliable orbital analysis. In the lowermost interval (~385-433 m WMSF), broad ~10-12 m packages in the raw record represent amplitude envelopes of million-year-scale modulation, not individual E405 cycles.

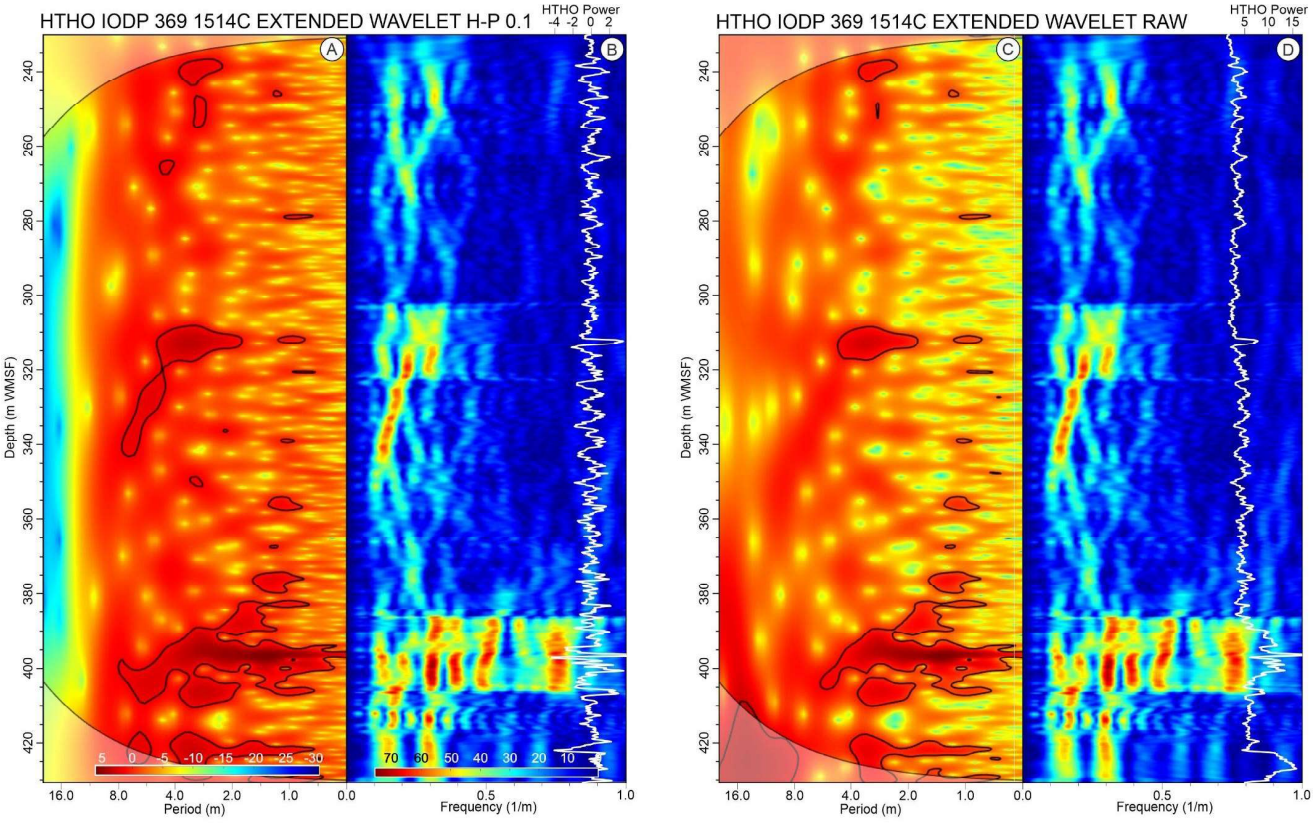


Figure S10: Extended wavelet analysis of HTHO at Hole U1514C (IODP Expedition 369). (A-B) High-Pass 0.1 filtered series: period-domain (A) and frequency-domain (B) representations. (C-D) Raw (unfiltered) HTHO series: period-domain (C) and frequency-domain (D) representations. Panels as in Fig. S9. In the filtered record (A-B), the E405 signal is intermittently expressed as an elevated power band from ~265 to ~405 m WMSF, with greater spatial variability than at U1579D (Fig. S9A-B), reflecting the more heterogeneous lithological substrate and lower signal-to-noise ratio at the Mentelle Basin hole. The upper portion (~265-360 m WMSF) shows more clearly defined cycles of ~4-6 m consistent with multi-method SAR estimates; the lower portion (~360-405 m WMSF) shows irregular cycle thicknesses and reduced E405 power. In the raw record (C-D), dominant power at very long periods (>8 m) is both higher in absolute power and more spectrally diffuse than at U1579D, reflecting the greater long-period non-orbital variance at U1514C and the necessity of High-Pass 0.1 pre-filtering for orbital analysis.

REFERENCES

Li, M., Hinnov, L., Kump, L., 2019. Acycle: Time-series analysis software for paleoclimate research and education. Comput. Geosci. 127, 12-22.

Torrence, C., Compo, G.P., 1998. A practical guide to wavelet analysis. Bull. Am. Meteorol. Soc. 79, 61-78.

Weedon, G.P., 2003. Time-Series Analysis and Cyclostratigraphy. Cambridge University Press.

Text S7: E405-kyr cycle positions for Holes U1579D and U1514C

The depth positions and thicknesses of individual E405 cycles identified in the HTHO records of Holes U1579D (Agulhas Plateau) and U1514C (Mentelle Basin) are summarised in Table S1. Cycle boundaries were placed at the minima of the bandpass-filtered HTHO series and define the lower and upper depth limits of each cycle in the wireline depth scale. Cycle thicknesses range from 4.11 to 11.89 m at U1579D (mean ~5.9 m) and from 3.50 to 7.62 m at U1514C (mean ~5.2 m), broadly consistent with the multi-method SAR estimates of ~1.1–2.1 cm/kyr and ~1.0–1.8 cm/kyr, respectively. Where successive cycles could not be individually resolved in the EHA, owing to reduced signal continuity or locally elevated noise, they are listed as a merged pair (e.g. cycles 8+9, 14+15). A total of 31 cycles are identified at U1579D and 29 at U1514C, spanning the full investigated interval.

Table S1. E405-kyr cycle positions and thicknesses for Holes U1579D (Agulhas Plateau) and U1514C (Mentelle Basin)

Hole U1579D - Agulhas Plateau (Expedition 392)			
Cycle Number	**Lower Limit (m WMSF)**	**Upper Limit (m WMSF)**	**Thickness (m)**
1	432.58	426.94	5.64
2	426.94	421.00	5.94
3	421.00	416.42	4.58
4	416.42	411.24	5.18
5	411.24	405.91	5.33
6	405.91	400.88	5.03
7	400.88	395.24	5.64
8+9	395.24	384.88	10.36
10	384.88	378.02	6.86
11	378.02	372.07	5.95
12	372.07	364.15	7.92
13	364.15	357.75	6.4
14+15	357.75	348.61	9.14
16	348.61	343.12	5.49
17	343.12	337.63	5.49
18+19	337.63	329.25	8.38

20	329.25	323.31	5.94
21	323.31	318.13	5.18
22	318.13	313.25	4.88
23	313.25	307.00	6.25
24	307.00	300.90	6.1
25	300.90	294.96	5.94
26	294.96	290.85	4.11
27	290.85	285.97	4.88
28	285.97	280.33	5.64
29+30	280.33	268.44	11.89
31	268.44	263.26	5.18

Hole U1514C – Mentelle Basin (Expedition 369)

Cycle Number	Lower Limit (m WMSF)	Upper Limit (m WMSF)	Thickness (m)
1	393.76	388.27	5.49
2+3	388.27	381.57	6.7
4	381.57	377.76	3.81
5	377.76	373.03	4.73
6	373.03	368.46	4.57
7	368.46	364.80	3.66
8	364.80	360.08	4.72
9	360.08	354.74	5.34
10	354.74	349.56	5.18
11+12	349.56	342.40	7.16
13+14	342.40	334.78	7.62
15	334.78	329.29	5.49
16	329.29	323.81	5.48
17	323.81	318.93	4.88
18	318.93	314.51	4.42
19	314.51	309.63	4.88
20+21	309.63	302.32	7.31
22	302.32	296.68	5.64
23	296.68	291.65	5.03
24	291.65	288.15	3.5
25	288.15	283.42	4.73
26	283.42	278.54	4.88
27	278.54	274.73	3.81
28	274.73	270.01	4.72
29	270.01	265.13	4.88

8 CONCLUDING REMARKS

In this work, we applied cyclostratigraphic methods to spectral gamma-ray thorium data from two Paleocene deep-marine sequences recovered during IODP Expeditions 392 and 369, at Holes U1579D (Agulhas Plateau, South Indian Ocean) and U1514C (Mentelle Basin, western Australia), respectively. The studied intervals span the entire Paleocene, from the K-Pg boundary (~66 Ma) to the PETM (~56 Ma), providing an approximately 10 million-year-long record of orbital cyclicity in the Indian Ocean sector.

The cross-correlation analysis (CCF) of the available spectral gamma-ray channels demonstrated that thorium (HTHO) constitutes the most reliable proxy for orbital signal detection in both pelagic carbonate sequences. The strong zero-lag correlation of HTHO with total NGR and potassium (HFK), combined with the phase lags and weak coherence exhibited by uranium (HURA) - of 2.44 m at U1579D and 3.96 m at U1514C, suggests that potential diagenetic remobilisation compromises the use of uranium as a cyclostratigraphic proxy in these settings. This conclusion has practical implications for the selection of proxies in future cyclostratigraphic investigations of similar depositional environments.

MTM spectral analysis and EHA of the detrended thorium series identify a dominant E405-kyr periodicity at both holes, with band limits of 4.55-8.40 m at U1579D and 4.24-7.19 m at U1514C. COCO, eCOCO, and TimeOpt analyses converge on sediment accumulation rate (SAR) estimates of ~1.1-2.1 cm/kyr for U1579D and ~1.0-1.8 cm/kyr for U1514C, consistent with the average SARs reported by the respective expedition proceedings (~1.7 cm/kyr for U1579D and ~1.4 cm/kyr for U1514C). Short eccentricity cycles are indicated, but their expression is not continuously resolved across the full depth interval; obliquity is tentatively identified at U1579D while absent at U1514C; precession is unresolvable once frequencies are probably below the Nyquist frequency.

Approximately 25.5 and 25 E405 cycles are identified between the K-Pg boundary and the PETM at the U1579D and U1514C records, respectively – therefore provisionally constraining the PETM to ~55.7–55.9 Ma. These counts are consistent with the 25-cycle Paleocene astrochronological framework now favoured by most recent studies (Hilgen *et al.,* 2010; Dinarès-Turell *et al.,* 2014; Clyde *et al.,* 2016), supporting a PETM age close to 56.01 ± 0.05 Ma (Zeebe and Lourens, 2019). Nevertheless, it is important to point out differences on the MTM and EHA patterns that could be observed for cyclostratigraphic results from both sites. Although both ATSs were quite compatible in terms of number of recorded E405 cycles, we noticed two distinct frequency components partially overlap within the U1514C stratigraphic interval, which possibly caused an apparent transient coalescence between low-frequency spectral power and the E405 component - therefore revealing a more complex influence comprising million-year-scale variability, finite depth–frequency resolution, and SAR changes.

A particularly important finding of this study is the identification of prominent positive HTHO anomalies at ~325 m WMSF (U1579D) and ~313 m WMSF (U1514C) as co-temporal at ~58.15 Ma. Their simultaneous expression at the Agulhas Plateau and the Mentelle Basin, two widely separated holes in the Indian Ocean, argues for a globally coherent sedimentary event rather than a local depositional artefact. This

age corresponds to the unnamed "*" CIE event originally identified by Littler *et al.* (2014) and retained in the orbital framework of Barnet *et al.* (2019), which marks the termination of the Paleocene Oxygen Isotope Maximum (POIM, 59.7-58.1 Ma) and the end of the $\delta^{13}C$-$\delta^{18}O$ decoupling interval that begins with the ELPE (~59.2 Ma). As characterised by Hollis *et al.* (2022), the "*" CIE occurs close to an eccentricity minimum and is understood as not being a classical hyperthermal; its positive HTHO expression at both holes is consistent with enhanced clay flux or carbonate dilution during this global carbon-cycle transition. Confirmation of the precise nature of this anomaly requires direct carbon and oxygen isotope data from these wells.

INPEFA modelling allowed for the identification of trend reversals at both holes that are consistent with depositional regime changes at the K-Pg boundary and near the ELPE/"*" event interval, and also broadly consistent with the Paleocene barystatic sea-level record of Miller *et al.* (2024). At U1579D, the INPEFA modeled curve shows a major trend shift at ~325 m WMSF, coinciding with the "*" event anomaly and possibly reflecting the documented transition from the relatively stable early-mid Paleocene to the progressively warming and carbon-cycle-destabilised late Paleocene.

These results contribute to the refinement of the Paleocene chronostratigraphic framework in the Indian Ocean sector, expand the geographic coverage of orbital calibration beyond the classical Atlantic and Pacific reference sections, and provide a new independent constraint on the timing and palaeoclimatic context of the "*" event at ~58.15 Ma. Future work incorporating direct isotopic ($\delta^{13}C$, $\delta^{18}O$, $\delta^{11}B$) measurements from these holes would be essential for fully characterising this event and further examination of our cyclostratigraphic age model.

REFERENCES

Adams, J.A., Weaver, C.E., 1958. Thorium-to-uranium ratios as indicators of sedimentary processes: example of concept of geochemical facies. AAPG Bulletin, 42(2), 387–430.

Agnini, C., Fornaciari, E., Raffi, I., Catanzariti, R., Pälike, H., Backman, J., Rio, D., 2014. Biozonation and biochronology of Paleogene calcareous nannofossils from low and middle latitudes. Newsletters on Stratigraphy, 47(2), 131–181.

Alvarez, L.W., Alvarez, W., Asaro, F., Michel, H.V., 1980. Extraterrestrial cause for the Cretaceous-Tertiary extinction. Science, 208(4448), 1095–1108.

Alvarez, L.W., Alvarez, W., Asaro, F., Michel, H.V., 1981. Response: Asteroid Extinction Hypothesis. Science, 211(4483), 654–656.

Arenillas, I., Molina, E., Ortiz, S., Schmitz, B., 2008. Foraminiferal and $\delta^{13}C$ isotopic event-stratigraphy across the Danian–Selandian transition at Zumaya (northern Spain). Terra Nova, 20(1), 38–44.

Babila, T.L., Penman, D.E., Standish, C.D., Doubrawa, M., Bralower, T.J., Robinson, M.M., et al., 2022. Surface ocean warming and acidification driven by rapid carbon release precedes Paleocene-Eocene Thermal Maximum. Science Advances, 8(11), eabg1025.

Barnet, J.S., Littler, K., Westerhold, T., Kroon, D., Leng, M.J., Bailey, I., et al., 2019. A high-fidelity benthic stable isotope record of late Cretaceous–early Eocene climate change and carbon-cycling. Paleoceanography and Paleoclimatology, 34(4), 672–691.

Barnosky, A. D., Matzke, N., Tomiya, S., Wogan, G. O., Swartz, B., Quental, T. B., ... & Ferrer, E. A., 2011. Has the Earth's sixth mass extinction already arrived?. Nature, 471(7336), 51-57.

Barthes, V., Pozzi, J.P., Vibert-Charbonnel, P., Thibal, J., Melieres, M.A., 1999. High-resolution chronostratigraphy from downhole susceptibility logging tuned by palaeoclimatic orbital frequencies. Earth and Planetary Science Letters, 165(1), 97–116.

Berger, A., 1988. Milankovitch theory and climate. Reviews of Geophysics, 26(4), 624–657.

Berger, A., Loutre, M. F., & Laskar, J., 1992. Stability of the astronomical frequencies over the Earth's history for paleoclimate studies. Science, 255(5044), 560-566.

Berger, A., Loutre, M.F., 1994. Astronomical forcing through geological time. Orbital forcing and cyclic sequences, p. 15–24.

Berggren, W.A., Pearson, P.N., 2005. A revised tropical to subtropical Paleogene planktonic foraminiferal zonation. The Journal of Foraminiferal Research, 35(4), 279–298.

Bernaola, G., Baceta, J.I., Orue-Etxebarria, X., Alegret, L., Martín-Rubio, M., Arostegui, J., Dinarès-Turell, J., 2007. Evidence of an abrupt environmental disruption during the mid-Paleocene biotic event (Zumaia section, western Pyrenees). Geological Society of America Bulletin, 119(7–8), 785–795.

Birch, H.S., Coxall, H.K., Pearson, P.N., Kroon, D., Schmidt, D.N., 2016. Partial collapse of the marine carbon pump after the Cretaceous-Paleogene boundary. Geology, 44(4), 287–290.

Birch, H., Schmidt, D.N., Coxall, H.K., Kroon, D., Ridgwell, A., 2021. Ecosystem function after the K/Pg extinction: decoupling of marine carbon pump and diversity. Proceedings of the Royal Society B, 288(1953).

Bohaty, S.M., Childress, L.B., Uenzelmann-Neben, G., et al., 2023. Agulhas Plateau Cretaceous Climate. Proceedings of the International Ocean Discovery Project, 392.

Borissova, I., Bradshaw, B., Nicholson, C., Payne, D., Struckmeyer, H., 2010. Mentelle Basin — tectonic evolution controlled by the combined extensional history of the Southwestern and Southern Australian margins. ASEG Extended Abstracts, 2010(1), 1–4.

Bornemann, A., Schulte, P., Sprong, J., Steurbaut, E., Youssef, M., Speijer, R.P., 2009. Latest Danian carbon isotope anomaly and associated environmental change in the southern Tethys (Nile Basin, Egypt). Journal of the Geological Society, 166(6), 1135–1142.

Bornemann, A., Jehle, S., Lägel, F., Deprez, A., Petrizzo, M.R., Speijer, R.P., 2021. Planktic foraminiferal response to an early Paleocene transient warming event and biostratigraphic implications. International Journal of Earth Sciences, 110(2), 583–594.

Bottjer, D. J., 2024. Analysis of ancient mass extinction recoveries in marine environments: Generating strategies for managing outcomes of the current mass extinction. National Science Review 11(1), nwad240.

Boulila, S., Dupont-Nivet, G., Galbrun, B., Bauer, H., Châteauneuf, J.J., 2021. Age and driving mechanisms of the Eocene–Oligocene transition from astronomical tuning of a lacustrine record (Rennes Basin, France). Climate of the Past, 17(6), 2343–2360.

Bowen, G.J., Maibauer, B.J., Kraus, M.J., Röhl, U., Westerhold, T., Steimke, A., et al., 2015. Two massive, rapid releases of carbon during the onset of the Palaeocene–Eocene thermal maximum. Nature Geoscience, 8(1), 44–47.

Bowen, G.J., Zachos, J.C., 2010. Rapid carbon sequestration at the termination of the Palaeocene–Eocene Thermal Maximum. Nature Geoscience, 3(12), 866–869.

Bradshaw, B.E., 2003. A revised structural framework for frontier basins on the southern and southwestern Australian continental margin. Geoscience Australia, Department of Industry, Tourism and Resources.

Burgess, S., 2019. Deciphering mass extinction triggers. Science, 363(6429), 815-816.

Cande, S.C., Kent, D.V., 1995. Revised calibration of the geomagnetic polarity timescale for the Late Cretaceous and Cenozoic. Journal of Geophysical Research: Solid Earth, 100(B4), 6093–6095.

Clyde, W.C., Ramezani, J., Johnson, K.R., Bowring, S.A., Jones, M.M., 2016. Direct high-precision U–Pb geochronology of the end-Cretaceous extinction and calibration of Paleocene astronomical timescales. Earth and Planetary Science Letters, 452, 272–280.

Coccioni, R., Frontalini, F., Bancalà, G., Fornaciari, E., Jovane, L., Sprovieri, M., 2010. The Dan-C2 hyperthermal event at Gubbio (Italy): Global implications, environmental effects, and causes. Earth and Planetary Science Letters, 297(1–2), 298–305.

Coccioni, R., Bancalà, G., Catanzariti, R., Fornaciari, E., Frontalini, F., Giusberti, L., et al., 2012. An integrated stratigraphic record of the Palaeocene–lower Eocene at Gubbio (Italy): new insights into the early Palaeogene hyperthermals and carbon isotope excursions. Terra Nova, 24(5), 380–386.

Coccioni, R., Frontalini, F., Catanzariti, R., Jovane, L., Rodelli, D., Rodrigues, I., et al., 2019. Paleoenvironmental signature of the Selandian-Thanetian Transition Event (STTE) and Early Late Paleocene Event (ELPE) in the Contessa Road section (western Neo-Tethys). Palaeogeography, Palaeoclimatology, Palaeoecology, 523, 62–77.

Crucifix, M., Loutre, M. F., & Berger, A., 2006. The climate response to the astronomical forcing. Space Science Reviews, 125(1), 213-226.

D'Hondt, S., Donaghay, P., Zachos, J.C., Luttenberg, D., Lindinger, M., 1998. Organic carbon fluxes and ecological recovery from the Cretaceous-Tertiary mass extinction. Science, 282(5387), 276–279.

Davis, J. C., & Sampson, R. J., 1986. Statistics and data analysis in geology (Vol. 646). New York: Wiley.

De Jong, M., Nio, S.D., Smith, D., Böhm, A.R., 2007. Subsurface correlation in the Upper Carboniferous (Westphalian) of the Anglo-Dutch Basin using the climate stratigraphic approach. First Break, 25, 49–59.

Dinarès-Turell, J., Baceta, J.I., Pujalte, V., Orue-Etxebarria, X., Bernaola, G., Lorito, S., 2003. Untangling the Palaeocene climatic rhythm: an astronomically calibrated Early Palaeocene magnetostratigraphy and biostratigraphy at Zumaia (Basque basin, northern Spain). Earth and Planetary Science Letters, 216(4), 483–500.

Dinarès-Turell, J., Baceta, J.I., Bernaola, G., Orue-Etxebarria, X., Pujalte, V., 2007. Closing the mid-Palaeocene gap: toward a complete astronomically tuned Palaeocene Epoch and Selandian and Thanetian GSSPs at Zumaia (Basque Basin, W Pyrenees). Earth and Planetary Science Letters, 262(3–4), 450–467.

Dinarès-Turell, J., Westerhold, T., Pujalte, V., Röhl, U., Kroon, D., 2014. Astronomical calibration of the Danian stage (Early Paleocene) revisited: Settling chronologies of sedimentary records across the Atlantic and Pacific Oceans. Earth and Planetary Science Letters, 405, 119–131.

Direen, N.G., Stagg, H.M., Symonds, P.A., Colwell, J.B., 2011. Dominant symmetry of a conjugate southern Australian and East Antarctic magma-poor rifted margin segment. Geochemistry, Geophysics, Geosystems, 12(2).

Direen, N.G., Cohen, B.E., Maas, R., Frey, F.A., Whittaker, J.M., Coffin, M.F., et al., 2017. Naturaliste Plateau: constraints on the timing and evolution of the Kerguelen Large Igneous Province and its role in Gondwana breakup. Australian Journal of Earth Sciences, 64(7), 851–869.

Dunhill, A. M., Zarzyczny, K., Shaw, J. O., Atkinson, J. W., Little, C. T., & Beckerman, A. P., 2024. Extinction cascades, community collapse, and recovery across a Mesozoic hyperthermal event. Nature Communications, 15(1), 8599.

Farhat, M., Auclair-Desrotour, P., Boué, G., & Laskar, J., 2022. The resonant tidal evolution of the Earth-Moon distance. Astronomy & Astrophysics, 665, L1.

Font, E., Adatte, T., Sial, A.N., de Lacerda, L.D., Keller, G., Punekar, J., 2016. Mercury anomaly, Deccan volcanism, and the end-Cretaceous mass extinction. Geology, 44(2), 171–174.

Friedrich, O., Norris, R.D., Erbacher, J., 2012. Evolution of middle to Late Cretaceous oceans — a 55 my record of Earth's temperature and carbon cycle. Geology, 40(2), 107–110.

Gibbs, S.J., Bown, P.R., Ward, B.A., Alvarez, S.A., Kim, H., Archontikis, O.A., et al., 2020. Algal plankton turn to hunting to survive and recover from end-Cretaceous impact darkness. Science Advances, 6(44), eabc9123.

Goldberg, D., 1997. The role of downhole measurements in marine geology and geophysics. Reviews of Geophysics, 35(3), 315–342.

Gorgas, T.J., Wilkens, R.H., 2002. Sedimentation rates off SW Africa since the late Miocene deciphered from spectral analyses of borehole and GRA bulk density profiles: ODP Sites 1081–1084. Marine Geology, 180(1–4), 29–47.

Gradstein, F.M., Ogg, J.G., Schmitz, M.D., Ogg, G.M. (Eds.), 2020. Geologic Time Scale 2020. Elsevier.

Grant, G.R., 2012. Pliocene-Pleistocene orbital cyclostratigraphy and glacial evolution of the East Antarctic Ice Sheet from continental rise IODP site U1361, Wilkes Land margin, East Antarctica. Doctoral dissertation, Victoria University of Wellington.

Grossmann, A., & Morlet, J., 1984. Decomposition of Hardy functions into square integrable wavelets of constant shape. SIAM journal on mathematical analysis, 15(4), 723-736.

Gutjahr, M., Ridgwell, A., Sexton, P.F., Anagnostou, E., Pearson, P.N., Pälike, H., et al., 2017. Very large release of mostly volcanic carbon during the Palaeocene-Eocene Thermal Maximum. Nature, 548, 573–577.

Harbich, M., Barnet, J.S., Rae, J.W., Kroon, D., 2024. Warming, acidification, and calcification feedback during the first hyperthermal of the Cenozoic — The Latest Danian Event. Geology, 52(1), 51–55.

Henehan, M.J., Ridgwell, A., Thomas, E., Zhang, S., Alegret, L., Schmidt, D.N., et al., 2019. Rapid ocean acidification and protracted Earth system recovery followed the end-Cretaceous Chicxulub impact. Proceedings of the National Academy of Sciences, 116(45), 22500–22504.

Hilgen, F., Schwarzacher, W., & Strasser, A., 2004. Concept and Definitions in Cyclostratigraphy (Second Report of the Cyclostratigraphy Working Group): International Subcommission on Stratigraphic Nomenclature of the IUGS Commission on Stratigraphy.

Hilgen, F.J., Kuiper, K.F., Lourens, L.J., 2010. Evaluation of the astronomical time scale for the Paleocene and earliest Eocene. Earth and Planetary Science Letters, 300(1–2), 139–151.

Hilgen, F.J., Hinnov, L.A., Aziz, H.A., Abels, H.A., Batenburg, S., Bosmans, J.H., et al., 2015. Stratigraphic continuity and fragmentary sedimentation: the success of cyclostratigraphy as part of integrated stratigraphy. Geological Society, London, Special Publications, 404(1), 157–197.

Hinnov, L. A., Hilgen, F. J., & Gradstein, F. M., 2012. Cyclostratigraphy and astrochronology. The geologic time scale, 1, 63-83.

Hinnov, L.A., 2013. Cyclostratigraphy and its revolutionizing applications in the earth and planetary sciences. Bulletin, 125(11–12), 1703–1734.

Hinnov, L.A., 2018. Cyclostratigraphy and astrochronology in 2018. In: Stratigraphy and Timescales. Academic Press, p. 1–80.

Hinnov, L. A., 2018. Astronomical metronome of geological consequence. Proceedings of the National Academy of Sciences, 115(24), 6104-6106.

Hollis, C.J., Crouch, E.M., Morgans, H.E.G., Handley, L., Baker, J.A., Creech, J., et al., 2022. Waipawa Formation deposition at Mead Stream, New Zealand, linked to Late Paleocene global events. New Zealand Journal of Geology and Geophysics, 65(3), 388–414.

Hsü, K.J., McKenzie, J.A., 1985. A "Strangelove" ocean in the earliest Tertiary. The carbon cycle and atmospheric CO_2: Natural variations Archean to present, 32, 487–492.

Huber, B. T., Hobbs, R. W., Bogus, K. A., Batenburg, S. J., Brumsack, H. J., do Monte Guerra, R., ... & Xu, Z., 2019. Expedition 369 summary. Proceedings of the International Ocean Discovery Program, 369, 101

Hull, P.M., Norris, R.D., 2011. Diverse patterns of ocean export productivity change across the Cretaceous-Paleogene boundary: New insights from biogenic barium. Paleoceanography, 26(3).

Hull, P., 2015. Life in the aftermath of mass extinctions. Current Biology, 25(19), R941-R952.

Hyland, E.G., Sheldon, N.D., Cotton, J.M., 2015. Terrestrial evidence for a two-stage mid-Paleocene biotic event. Palaeogeography, Palaeoclimatology, Palaeoecology, 417, 371–378.

Inglis, G.N., Bragg, F., Burls, N.J., Cramwinckel, M.J., Evans, D., Foster, G.L., et al., 2020. Global mean surface temperature and climate sensitivity of the early Eocene Climatic Optimum (EECO), Paleocene–Eocene Thermal Maximum (PETM), and latest Paleocene. Climate of the Past, 16(5), 1953–1968.

Jablonski, D., & Edie, S. M., 2025. Mass extinctions and their rebounds: a macroevolutionary framework. Paleobiology, 51(1), 83-96.

Jehle, S., Bornemann, A., Deprez, A., Speijer, R.P., 2015. The Impact of the Latest Danian Event on planktic foraminiferal faunas at ODP Site 1210 (Shatsky Rise, Pacific Ocean). PLoS One, 10(11), e0141644.

Jehle, S., Bornemann, A., Lägel, A.F., Deprez, A., Speijer, R.P., 2019. Paleoceanographic changes across the Latest Danian Event in the South Atlantic Ocean and planktic foraminiferal response. Palaeogeography, Palaeoclimatology, Palaeoecology, 525, 1–13.

Keller, G., 2014. Deccan volcanism, the Chicxulub impact, and the end-Cretaceous mass extinction: Coincidence? Cause and effect? Special Paper, Geological Society of America, 505, 57–89.

Keller, G., Punekar, J., Mateo, P., 2016. Upheavals during the late Maastrichtian: Volcanism, climate and faunal events preceding the end-Cretaceous mass extinction. Palaeogeography, Palaeoclimatology, Palaeoecology, 441, 137–151.

Kennett, J.P., Stott, L.D., 1991. Abrupt deep-sea warming, palaeoceanographic changes and benthic extinctions at the end of the Palaeocene. Nature, 353(6341), 225–229.

Kent, D. V., Olsen, P. E., Rasmussen, C., Lepre, C., Mundil, R., Irmis, R. B., ... & Parker, W. G., 2018. Empirical evidence for stability of the 405-kiloyear Jupiter–Venus eccentricity cycle over hundreds of millions of years. Proceedings of the National Academy of Sciences, 115(24), 6153-6158.

Koch, P.L., Zachos, J.C., Gingerich, P.D., 1992. Correlation between isotope records in marine and continental carbon reservoirs near the Palaeocene/Eocene boundary. Nature, 358(6384), 319–322.

Kodama, K.P., Hinnov, L.A., 2014. Rock Magnetic Cyclostratigraphy. John Wiley and Sons.

König, M., Jokat, W., 2010. Advanced insights into magmatism and volcanism of the Mozambique Ridge and Mozambique Basin in the view of new potential field data. Geophysical Journal International, 180(1), 158–180.

Kulhánek, O., 2012. Introduction to digital filtering in geophysics. Elsevier.

Laskar, J., Robutel, P., Joutel, F., Gastineau, M., Correia, A.C., Levrard, B., 2004. A long-term numerical solution for the insolation quantities of the Earth. Astronomy and Astrophysics, 428(1), 261–285.

Laskar, J., Fienga, A., Gastineau, M., Manche, H., 2011. La2010: a new orbital solution for the long-term motion of the Earth. Astronomy and Astrophysics, 532, A89.

Leandro, C. G., Savian, J. F., Kochhann, M. V. L., Franco, D. R., Coccioni, R., Frontalini, F., ... & Trindade, R. I. F. D., 2022. Astronomical tuning of the Aptian stage and its implications for age recalibrations and paleoclimatic events. Nature Communications, 13(1), 2941.

Li, M., Kump, L. R., Hinnov, L. A., & Mann, M. E., 2018. Tracking variable sedimentation rates and astronomical forcing in Phanerozoic paleoclimate proxy series with evolutionary correlation coefficients and hypothesis testing. Earth and Planetary Science Letters, 501, 165-179.

Li, M., et al., 2019. Paleoclimate proxies for cyclostratigraphy: Comparative analysis using a Lower Triassic marine section in South China. Earth-Science Reviews, 189, 125–146.

Li, M., Bralower, T.J., Kump, L.R., Self-Trail, J.M., Zachos, J.C., Rush, W.D., Robinson, M.M., 2022. Astrochronology of the Paleocene-Eocene Thermal Maximum on the Atlantic coastal plain. Nature Communications, 13(1), 5618.

Littler, K., Röhl, U., Westerhold, T., Zachos, J.C., 2014. A high-resolution benthic stable-isotope record for the South Atlantic: Implications for orbital-scale changes in late Paleocene–early Eocene climate and carbon cycling. Earth and Planetary Science Letters, 401, 18–30.

Liu, Y., Li, H., Peng, P., Wu, M., Yan, N., Qin, X., Zhang, Y., 2024. High-resolution sequence stratigraphy research based on continuous wavelet transform and INPEFA: A case study in the Kalashayi Formation, Tarim Basin, China. Unconventional Resources, 4, 100099.

Lourens, L.J., Sluijs, A., Kroon, D., Zachos, J.C., Thomas, E., Röhl, U., et al., 2005. Astronomical pacing of late Palaeocene to early Eocene global warming events. Nature, 435(7045), 1083–1087.

Ma, M., Wang, M., Huang, H., Liu, X., 2024. Terrestrial records of two hyperthermal events in the Cretaceous-Paleogene boundary suggest different control mechanisms. Communications Earth and Environment, 5(1), 248.

Maloney, D., Sargent, C., Direen, N.G., Hobbs, R.W., Gröcke, D.R., 2011. Re-evaluation of the Mentelle Basin, a polyphase rifted margin basin, offshore southwest Australia. Solid Earth, 2(2), 107–123.

Mann, M.E., Lees, J.M., 1996. Robust estimation of background noise and signal detection in climatic time series. Climatic Change, 33(3), 409–445.

Mantua, N. J., & Hare, S. R., 2002. The Pacific decadal oscillation. Journal of oceanography, 58(1), 35-44.

McInerney, F.A., Wing, S.L., 2011. The Paleocene-Eocene Thermal Maximum: A perturbation of carbon cycle, climate, and biosphere with implications for the future. Annual Review of Earth and Planetary Sciences, 39, 489–516.

Meyers, S.R., 2012. Seeing red in cyclic stratigraphy: Spectral noise estimation for astrochronology. Paleoceanography, 27(3).

Meyers, S.R., 2015. The evaluation of eccentricity-related amplitude modulation and bundling in paleoclimate data: An inverse approach for astrochronologic testing and time scale optimization. Paleoceanography, 30(12), 1625–1640.

Meyers, S.R., Malinverno, A., 2018. Proterozoic Milankovitch cycles and the history of the solar system. Proceedings of the National Academy of Sciences, 115(25), 6363–6368.

Meyers, S. R., 2019. Cyclostratigraphy and the problem of astrochronologic testing. Earth-Science Reviews, 190, 190-223.

Miller, K.G., Kominz, M.A., Browning, J.V., Wright, J.D., Mountain, G.S., Katz, M.E., et al., 2005. The Phanerozoic record of global sea-level change. Science, 310(5752), 1293–1298.

Miller, K.G., Browning, J.V., Schmelz, W.J., Kopp, R.E., Mountain, G.S., Wright, J.D., 2020. Cenozoic sea-level and cryospheric evolution from deep-sea geochemical and continental margin records. Science Advances, 6(20), eaaz1346.

Miller, K. G., Schmelz, W. J., Browning, J. V., Rosenthal, Y., Hess, A. V., Kopp, R. E., & Wright, J. D., 2024. Global mean and relative sea-level changes over the past 66 Myr: implications for early Eocene ice sheets. Earth Science, Systems and Society, 4(1), 10091.

Mitchell Jr, J. M., 1976. An overview of climatic variability and its causal mechanisms. Quaternary Research, 6(4), 481-493.

Mitchell, R. N., Bice, D. M., Montanari, A., Cleaveland, L. C., Christianson, K. T., Coccioni, R., & Hinnov, L. A., 2008. Oceanic anoxic cycles? Orbital prelude to the Bonarelli Level (OAE 2). Earth and Planetary Science Letters, 267(1-2), 1-16.

Myers, K.J., Wignall, P.B., 1987. Understanding Jurassic organic-rich mudrocks — new concepts using gamma-ray spectrometry and palaeoecology. Marine clastic sedimentology: Concepts and case studies, p. 172–189.

Nainggolan, H.B., Winardhi, S., 2019. Geophysical approach to improve well correlation and stratigraphy package in the frontier area: Example case of Upper Jurassic Fm. Semai Basin, Eastern Indonesia. IOP Conference Series: Earth and Environmental Science, 311, 012013.

Newman, P. A., Coy, L., Pawson, S., & Lait, L. R., 2016. The anomalous change in the QBO in 2015–2016. Geophysical Research Letters, 43(16), 8791-8797.

Nio, S.D., Brouwer, J., Smith, D.G., De Jong, M., Böhm, A., 2005. Spectral trend attribute analysis: Applications in the stratigraphic analysis of wireline logs. First Break, 23, 71–75.

Nunes, F., Norris, R.D., 2006. Abrupt reversal in ocean overturning during the Palaeocene/Eocene warm period. Nature, 439(7072), 60–63.

Osmond, J.K., Ivanovich, M., 1992. Uranium-series mobilization and surface hydrology. In: Uranium-series disequilibrium: applications to earth, marine, and environmental sciences, 2nd ed.

Pagani, M., Caldeira, K., Archer, D., Zachos, J.C., 2006. An ancient carbon mystery. Science, 314(5805), 1556–1557.

Parkinson, D.N., 1996. Gamma-ray spectrometry as a tool for stratigraphical interpretation: examples from the western European Lower Jurassic. Geological Society, London, Special Publications, 103(1), 231–255.

Paulissen, W.E., Luthi, S.M., 2011. High-frequency cyclicity in a Miocene sequence of the Vienna Basin established from high-resolution logs and robust chronostratigraphic tuning. Palaeogeography, Palaeoclimatology, Palaeoecology, 307(1–4), 313–323.

Philander, S. G., 1989. El Niño, La Niña, and the southern oscillation. International geophysics series, 46, X-289.

Preto, N., Hinnov, L. A., De Zanche, V., Mietto, P., & Hardie, L. A., 2004. The Milankovitch interpretation of the Latemar platform cycles (Dolomites, Italy): Implications for geochronology, biostratigraphy, and Middle Triassic carbonate accumulation.

Qayyum, F., Smith, D., 2014. Integrated sequence stratigraphy using trend logs and densely mapped seismic data. First Break, 32, 75–84.

Quillevéré, F., Norris, R.D., Kroon, D., Wilson, P.A., 2008. Transient ocean warming and shifts in carbon reservoirs during the early Danian. Earth and Planetary Science Letters, 265(3–4), 600–615.

Renne, P.R., Sprain, C.J., Richards, M.A., Self, S., Vanderkluysen, L., Pande, K., 2015. State shift in Deccan volcanism at the Cretaceous-Paleogene boundary, possibly induced by impact. Science, 350(6256), 76–78.

Röhl, U., Westerhold, T., Bralower, T. J., & Zachos, J. C., 2007. On the duration of the Paleocene-Eocene thermal maximum (PETM). Geochemistry, Geophysics, Geosystems, 8(12).

Ruddiman, W. F., 2001. Earth's climate: past and future. Macmillan.

Ruffell, A., Worden, R., 2000. Palaeoclimate analysis using spectral gamma-ray data from the Aptian (Cretaceous) of southern England and southern France. Palaeogeography, Palaeoclimatology, Palaeoecology, 155(3–4), 265–283.

Saunders, A.D., 2016. Two LIPs and two Earth-system crises: the impact of the North Atlantic Igneous Province and the Siberian Traps on the Earth-surface carbon cycle. Geological Magazine, 153(2), 201–222.

Schmitz, B., Pujalte, V., Molina, E., Monechi, S., Orue-Etxebarria, X., Speijer, R.P., et al., 2011. The global stratotype sections and points for the bases of the Selandian (Middle Paleocene) and Thanetian (Upper Paleocene) stages at Zumaia, Spain. Episodes Journal of International Geoscience, 34(4), 220–243.

Schnyder, J., et al., 2006. Conjunctive use of spectral gamma-ray logs and clay mineralogy in defining late Jurassic–early Cretaceous palaeoclimate change (Dorset, UK). Palaeogeography, Palaeoclimatology, Palaeoecology, 229(4), 303–320.

Schoene, B., Samperton, K.M., Eddy, M.P., Keller, G., Adatte, T., Bowring, S.A., et al., 2014. U-Pb geochronology of the Deccan Traps and relation to the end-Cretaceous mass extinction. Science, 347(6218), 182–184.

Schulte, P., Alegret, L., Arenillas, I., Arz, J.A., Barton, P.J., Bown, P.R., et al., 2010. The Chicxulub asteroid impact and mass extinction at the Cretaceous-Paleogene boundary. Science, 327(5970), 1214–1218.

Sluijs, A., Schouten, S., Pagani, M., Woltering, M., Brinkhuis, H., Damsté, J.S.S., et al., 2006. Subtropical Arctic Ocean temperatures during the Palaeocene/Eocene thermal maximum. Nature, 441(7093), 610–613.

Sluijs, A., Brinkhuis, H., Schouten, S., Bohaty, S.M., John, C.M., Zachos, J.C., et al., 2007. Environmental precursors to rapid light carbon injection at the Palaeocene/Eocene boundary. Nature, 450(7173), 1218.

Sluijs, A., Bijl, P.K., Schouten, S., Rohl, U., Reichart, G.J., Brinkhuis, H., 2011. Southern ocean warming, sea level and hydrological change during the Paleocene-Eocene thermal maximum. Climate of the Past, 7, 47–61.

Smit, J., 1999. The global stratigraphy of the Cretaceous-Tertiary boundary impact ejecta. Annual Review of Earth and Planetary Sciences, 27(1), 75–113.

Sprain, C.J., Renne, P.R., Clemens, W.A., Wilson, G.P., 2018. Calibration of chron C29r: New high-precision geochronologic and paleomagnetic constraints from the Hell Creek region, Montana. Bulletin, 130(9–10), 1615–1644.

Sprain, C.J., Renne, P.R., Vanderkluysen, L., Pande, K., Self, S., Mittal, T., 2019. The eruptive tempo of Deccan volcanism in relation to the Cretaceous-Paleogene boundary. Science 363, 866–870. https://doi.org/10.1126/science.aav1446.

Strasser, A., Hilgen, F. J., & Heckel, P. H., 2006. Cyclostratigraphy-concepts, definitions, and applications. Newsletters on Stratigraphy, 42, 75-114.

Svensen, H., Planke, S., Malthe-Sørenssen, A., Jamtveit, B., Myklebust, R., Rasmussen Eidem, T., Rey, S.S., 2004. Release of methane from a volcanic basin as a mechanism for initial Eocene global warming. Nature, 429(6991), 542–545.

Telford, W. M., Geldart, L. P., & Sheriff, R. E., 1990. Applied geophysics. Cambridge university press.

Thomas, E., 1998. Biogeography of the late Paleocene benthic foraminiferal extinction. In: Aubry, M.-P., Lucas, S., Berggren, W.A. (Eds.), Late Paleocene-Early Eocene Climatic and Biotic Events in the Marine and Terrestrial Records. Columbia University Press, New York, pp. 214–243.

Thomas, D.J., Bralower, T.J., Jones, C.E., 2003. Neodymium isotopic reconstruction of late Paleocene–early Eocene thermohaline circulation. Earth and Planetary Science Letters, 209(3–4), 309–322.

Thomas, E., 2007. Cenozoic mass extinctions in the deep sea: What perturbs the largest habitat on Earth? Geological Society of America Special Papers, 424, 1–23.

Thomson, D.J., 1990. Time series analysis of Holocene climate data. Philosophical Transactions of the Royal Society of London. Series A, 330(1615), 601–616.

Toon, O.B., Zahnle, K., Morrison, D., Turco, R.P., Covey, C., 1997. Environmental perturbations caused by the impacts of asteroids and comets. Reviews of Geophysics, 35(1), 41–78.

Torrence, C., Compo, G.P., 1998. A practical guide to wavelet analysis. Bull. Am. Meteorol. Soc. 79, 61-78.

Tripati, A., Elderfield, H., 2005. Deep-sea temperature and circulation changes at the Paleocene-Eocene thermal maximum. Science, 308(5730), 1894–1898.

Tucholke, B.E., Carpenter, G.B., 1977. Sediment distribution and Cenozoic sedimentation patterns on the Agulhas Plateau. Geological Society of America Bulletin, 88(9), 1337–1346.

Tucholke, B.E., Embley, R.W., 1984. Cenozoic regional erosion of the abyssal sea floor off South Africa. In: Schlee, J.S. (Ed.), Interregional Unconformities and Hydrocarbon Accumulation. American Association of Petroleum Geologists Memoir, 36, 145–164.

Uenzelmann-Neben, G., Bohaty, S.M., Childress, L.B., et al., 2023. Agulhas Plateau Cretaceous Climate. Proceedings of the International Ocean Discovery Project, 392.

Vellekoop, J., Sluijs, A., Smit, J., Schouten, S., Weijers, J.W., Sinninghe Damsté, J.S., Brinkhuis, H., 2014. Rapid short-term cooling following the Chicxulub impact at the Cretaceous–Paleogene boundary. Proceedings of the National Academy of Sciences, 111(21), 7537–7541.

Vellekoop, J., Esmeray-Senlet, S., Miller, K.G., Browning, J.V., Sluijs, A., van de Schootbrugge, B., et al., 2016. Evidence for Cretaceous-Paleogene boundary bolide "impact winter" conditions from New Jersey, USA. Geology, 44(8), 619–622.

van Hinsbergen, D.J., De Groot, L.V., van Schaik, S.J., Spakman, W., Bijl, P.K., Sluijs, A., et al., 2015. A paleolatitude calculator for paleoclimate studies. PloS One, 10(6), e0126946.

von der Heydt, A. S., Ashwin, P., Camp, C. D., Crucifix, M., Dijkstra, H. A., Ditlevsen, P., & Lenton, T. M., 2021. Quantification and interpretation of the climate variability record. Global and Planetary Change, 197, 103399.

Wade, B.S., Pearson, P.N., Berggren, W.A., Pälike, H., 2011. Review and revision of Cenozoic tropical planktonic foraminiferal biostratigraphy and calibration to the geomagnetic polarity and astronomical time scale. Earth-Science Reviews, 104(1–3), 111–142.

Waltham, D., 2015. Milankovitch period uncertainties and their impact on cyclostratigraphy. Journal of Sedimentary Research, 85(8), 990–998.

Weedon, G.P., 2003. Time-series analysis and cyclostratigraphy: examining stratigraphic records of environmental cycles. Cambridge University Press.

Westerhold, T., Röhl, U., Laskar, J., Raffi, I., Bowles, J., Lourens, L.J., Zachos, J.C., 2007. On the duration of magnetochrons C24r and C25n and the timing of early Eocene global warming events. Paleoceanography, 22(2).

Westerhold, T., Röhl, U., Raffi, I., Fornaciari, E., Monechi, S., Reale, V., et al., 2008. Astronomical calibration of the Paleocene time. Palaeogeography, Palaeoclimatology, Palaeoecology, 257(4), 377–403.

Westerhold, T., Röhl, U., Donner, B., McCarren, H.K., Zachos, J.C., 2011. A complete high-resolution Paleocene benthic stable isotope record for the central Pacific (ODP Site 1209). Paleoceanography, 26(2).

Westerhold, T., Röhl, U., Frederichs, T., Bohaty, S.M., Zachos, J.C., 2015. Astronomical calibration of the geological timescale: closing the middle Eocene gap. Climate of the Past, 11(9), 1181–1195.

Westerhold, T., Röhl, U., Frederichs, T., Agnini, C., Raffi, I., Zachos, J.C., Wilkens, R.H., 2017. Astronomical calibration of the Ypresian timescale: implications for seafloor spreading rates and the chaotic behavior of the solar system? Climate of the Past, 13(9), 1129–1152.

Westerhold, T., Röhl, U., Donner, B., Frederichs, T., Kordesch, W.E.C., Bohaty, S.M., et al., 2018. Late Lutetian Thermal Maximum — Crossing a thermal threshold in Earth's climate system? Geochemistry, Geophysics, Geosystems, 19(1), 73–82.

Westerhold, T., Marwan, N., Drury, A.J., Liebrand, D., Agnini, C., Anagnostou, E., et al., 2020. An astronomically dated record of Earth's climate and its predictability over the last 66 million years. Science, 369(6509), 1383–1387.

Wu, Y., Malinverno, A., Meyers, S. R., & Hinnov, L. A., 2024. A 650-Myr history of Earth's axial precession frequency and the evolution of the Earth-Moon system derived from cyclostratigraphy. Science Advances, 10(42), eado2412.

Yuan, R., Zhu, R., Qu, J., Wu, J., You, X., Sun, Y., et al., 2018. Utilizing integrated prediction error filter analysis (INPEFA) to divide base-level cycle of fan-deltas. Open Geosciences, 10, 79–86.

Zachos, J., Pagani, M., Sloan, L., Thomas, E., Billups, K., 2001. Trends, rhythms, and aberrations in global climate 65 Ma to present. Science, 292(5517), 686–693.

Zachos, J.C., Röhl, U., Schellenberg, S.A., Sluijs, A., Hodell, D.A., Kelly, D.C., et al., 2005. Rapid acidification of the ocean during the Paleocene-Eocene thermal maximum. Science, 308(5728), 1611–1615.

Zachos, J.C., Schouten, S., Bohaty, S., Quattlebaum, T., Sluijs, A., Brinkhuis, H., et al., 2006. Extreme warming of mid-latitude coastal ocean during the Paleocene-Eocene Thermal Maximum. Geology, 34(9), 737–740.

Zachos, J.C., Dickens, G.R., Zeebe, R.E., 2008. An early Cenozoic perspective on greenhouse warming and carbon-cycle dynamics. Nature, 451(7176), 279–283.

Zachos, J.C., McCarren, H., Murphy, B., Röhl, U., Westerhold, T., 2010. Tempo and scale of late Paleocene and early Eocene carbon isotope cycles: Implications for the origin of hyperthermals. Earth and Planetary Science Letters, 299(1–2), 242–249.

Zeebe, R.E., Ridgwell, A., Zachos, J.C., 2016. Anthropogenic carbon release rate unprecedented during the past 66 million years. Nature Geoscience, 9(4), 325–329.

Zeebe, R.E., Westerhold, T., Littler, K., Zachos, J.C., 2017. Orbital forcing of the Paleocene and Eocene carbon cycle. Paleoceanography, 32(5), 440–465.

Zeebe, R.E., Lourens, L.J., 2019. Solar System chaos and the Paleocene–Eocene boundary age constrained by geology and astronomy. Science, 365(6456), 926–929.

Zeebe, R. E., & Lantink, M. L., 2024. Milanković forcing in deep time. Paleoceanography and Paleoclimatology, 39(5), e2024PA004861.

Zulivandama, S.R., Razi, F., Taslim, J.N., Winardhi, I.S., 2018. Sequence analysis on carbonate formation using integrated prediction error filter analysis (INPEFA) approach. In: The 43rd Annual Scientific Meeting, Himpunan Ahli Geofisika Indonesia, Semarang, 24–27.